Universiteit
Leiden
The Netherlands

Surface-structure dependence of water-related adsorbates on platinum

Badan, C.

Citation

Badan, C. (2016, November 22). *Surface-structure dependence of water-related adsorbates on platinum*. Retrieved from https://hdl.handle.net/1887/44295

Version:	Not Applicable (or Unknown)
License:	Licence agreement concerning inclusion of doctoral thesis in the Institutional Repository of the University of Leiden
Downloaded from:	https://hdl.handle.net/1887/44295

Note: To cite this publication please use the final published version (if applicable).

Cover Page

Universiteit Leiden

The handle http://hdl.handle.net/1887/44295 holds various files of this Leiden University dissertation.

Author: Badan, C.
Title: Surface-structure dependence of water-related adsorbates on platinum
Issue Date: 2016-11-22

Surface-Structure Dependence of Water-Related Adsorbates on Platinum

Proefschrift

ter verkrijging van

de graad van Doctor aan de Universiteit Leiden,

op gezag van Rector Magnificus prof. mr. C.J.J.M. Stolker,

volgens besluit van het College voor Promoties

te verdedigen op dinsdag 22 november 2016

klokke 15:00

door

Cansin Badan

geboren te Çukurova, Adana in 1987

Promotiecommissie:

Promotor: Prof. Dr. M.T.M. Koper

Co-Promotor: Dr. L.B.F. Juurlink

Overige Leden:

Prof. Dr. J. Brouwer
Prof. Dr. G.J. Kroes
Prof. Dr. B. Nieuwenhuys
Prof. Dr. K. Morgenstern (Ruhr-University Bochum, Germany)
Dr. H. J. Fraser (The Open University, Milton Keynes, UK)
Dr. I.M.N. Groot

ISBN: 978-90-9029995-2

We gratefully acknowledge financial support from the Netherlands Organization for Scientific Research (NWO).

...dedicated to Adil and Gülay

Contents

1 Introduction **1**
1.1 Catalysis 1
1.2 Surface science approach and the need for ultra-high vacuum (UHV) 3
1.3 Surface-structure sensitivity 4
1.4 Scope 6
1.5 Bibliography 8

2 The Analysis of Temperature Programmed Desorption Experiments **11**
2.1 Temperature Programmed Desorption (TPD) 11
2.1.1 Redhead analysis 13
2.1.2 Leading edge analysis 14
2.1.3 Complete analysis 15
2.1.4 Inverse optimization 17
2.2 Conclusions 20
2.3 Bibliography 22

3 Experimental Set-up **23**
3.1 Set-up 23
3.2 Temperature programmed desorption 25
3.3 Low energy electron diffraction 27
3.4 Bibliography 29

4 How well Does Pt(211) Represent Pt[n(111)x(100)] Surfaces in Adsorption/Desorption? **31**
4.1 Abstract 31
4.2 Introduction 33
4.3 Experimental 34
4.4 Results and discussion 36

4.4.1 Water . . . 36
4.4.2 Deuterium . . . 41
4.4.3 Oxygen . . . 43
4.5 Conclusions . . . 50
4.6 Bibliography . . . 52

5 Surface Structure Dependence in Desorption and Crystallization of Thin Interfacial Water Films on Pt 57
5.1 Abstract . . . 57
5.2 Introduction . . . 58
5.3 Experimental Section . . . 59
5.4 Results and discussion . . . 60
5.5 Conclusions . . . 64
5.6 Bibliography . . . 65

6 The Interaction Between Water and Sub- and Pre-adsorbed Deuterium on Pt(211) 69
6.1 Abstract . . . 69
6.2 Introduction . . . 71
6.3 Experimental Section . . . 72
6.4 Results and discussion . . . 72
6.5 Conclusion . . . 80
6.6 Bibliography . . . 80

7 Step-Type Selective Oxidation of Pt Surfaces 83
7.1 Abstract . . . 83
7.2 Introduction . . . 85
7.3 Experimental Section . . . 86
7.4 Results and discussion . . . 89
7.5 Conclusion . . . 101
7.6 Bibliography . . . 101

8 Summary 105
8.1 Summary . . . 105
8.2 Samenvatting . . . 108

A Supporting information to Chapter 7 112

List of Publications 117

Curriculum Vitae 119

Chapter 1

Introduction

1.1 Catalysis

The term catalysis, proposed in 1835 by Jakob Berzelius (1779-1848), comes from the Greek words *kata*, meaning down, and *lyein*, meaning loosen. Berzelius wrote the following to clarify his definition, "*the property of exercising on other bodies an action which is very different from chemical affection. By means of this action, they produce decomposition in bodies, and form new compounds into the composition of which they do not enter*"[1]. Without literally defining what it actually is, humankind has been aware of the influences of catalysis since ancient times. In the beginning of mankind's civilization, our awareness was solely based on simple processes, e.g. producing alcohol by fermentation. With the industrialization of human society, today we can utilize and design various catalysts to make energy resources, to synthesize nearly 90 % of the products of chemical and pharmaceutical industry, and to reduce pollution from power plants and cars. Our society would not have reached its modern status without employing catalysis in our life[2–4].

There are three sub-disciplines in catalysis namely: biological, homogeneous, and heterogeneous catalysis. Enzymes are biological catalysts which can catalyze a single or multiple chemical reactions both inside and outside of living cells. In homogeneous catalysis, the catalysts occupy the same phase as the reaction mixture. A very well-known example is ozone depletion where chlorofluorocarbons (CFCs) and other halogenated molecules react with O_3 to form O_2. For this reaction, CFCs catalyze the decomposition of ozone and remain nearly unaltered[3].

In heterogeneous catalysis, the catalyst and the reactants are in different phases. As the catalytic reaction takes place on the surface of the catalyst, it is crucial that small particles with larger surface areas (nanoparticles) are used.

Compared to other catalysts, heterogeneous catalysts are more tolerant to extreme operating conditions. Hence, they are the primary catalysts used in the chemical and petrochemical industries. A typical heterogeneous catalysis reaction starts with the adsorption of the reacting species on the surface of the (generally impenetrable) catalyst. Next, the adsorbed species react on the surface. This involves several steps where intramolecular bonds may be weakened or even broken and new bonds may be formed. With introducing some energy, the products finally desorb from the surface into the gas phase. As soon as the product desorbs, it liberates a new available adsorption site on the surface to regenerate another catalytic cycle[3, 4].

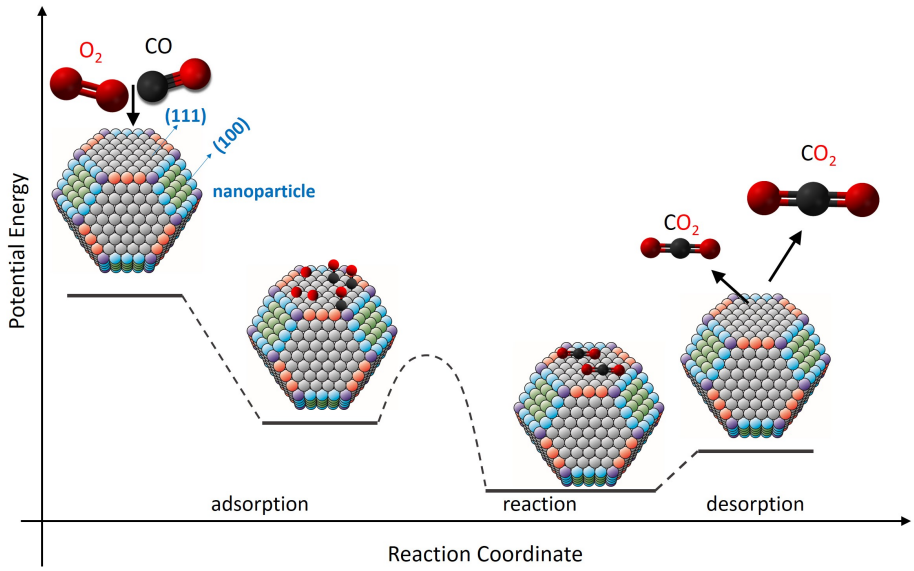

Figure 1.1: Schematic representation for the catalytic oxidation of CO by O_2 on a Pt nanoparticle.

Figure 1.1 illustrates the reaction cycle and potential energy diagram for the well known reaction most commonly applied to exhaust systems in cars. In this catalytic reaction CO is oxidized on the Pt catalyst, which sits between the engine and the tailpipe. Because adsorption is an exothermic process, the potential energy decreases during the associative adsorption of CO and dissociative adsorption of O_2. On a Pt surface, the dissociated O_{ad} and CO_{ad} combine to form $CO_{2,ad}$. Finally, the new product, CO_2, desorbs from the surface of Pt nanoparticle.

1.2 Surface science approach and the need for ultra-high vacuum (UHV)

In the last decades, petroleum and natural gas became the major natural resource ($> 60\%$) of the main energy production for 7 billions inhabitants on earth. Because of the consequential increase in energy demand, we are expected to be even more dependent on the raw chemical materials in the upcoming decades. Due to this inevitable dependency on natural resources, many developed countries are bringing new laws which promote renewable energy sources [5].

An ideal solution to our dependency to natural resources should be forged by a simple and rather abundant component such as water. If H_2O is split to its components, H_2 can be generated and used as clean and compact energy[6]. In electrochemistry, several precious heterogeneous catalysts, e.g. Pt, Pd, Rh, and Ni, are studied in detail to perform similar reactions that potentially play a key role to bring our dependency to fossil fuels to an end. Hence, a concrete understanding of interactions between catalysts and water is needed to develop or create a more active, selective, stable, mechanically robust and economically feasible catalyst [3, 4, 7]. To accomplish this, different scientific branches are merged to identify efficient and less efficient catalysts. For instance, theoretical studies can examine the structural and dynamic properties of reactions[8]. They can predict the possibility of so far entirely unknown catalysts, their active sites and explore the reaction mechanisms[9].

From theoretical point of view, however, it still remains challenging to predict the interactions of molecules containing many atoms. In addition, it is very difficult and expensive to include all the possible interactions, involving bond breaking or bond formation, that occur at the kinks, defects or steps[10]. In this aspect, electrochemistry offers more realistic, direct or indirect insight applicable to gas-phase studies. Despite the advantages, the various type of aggressive media can influence the long-term stability and durability of the electrode very negatively. Also, the electrochemical processes undergo mass-transport limitations causing difficulties to investigate the solid-liquid interfaces[11].

Particularly to understand the fundamental interaction between small molecules (such as H_2, O_2, and H_2O) and Pt, a UHV system can be used as a model approach. In a UHV system, there are significantly less particles per unit volume compared to atmospheric pressure. Hence, under UHV conditions the surface of the sample can be maintained clean for a couple of hours. Moreover, UHV can provide a reproducible domain where the amount and the type of adsorbates can be easily controlled.

Especially with the advances in vacuum technology in the late 1950s, many

surface probing techniques including temperature programmed desorption (TPD), low electron energy diffraction (LEED), etc, developed (chapter 2). Most of these techniques require an optimum impingement rate and mean free path, which can be accomplished only at pressure ranges below 10^{-9} bar. Since such a low pressure range stands out as a drawback of using UHV when it is compared to real processes, more techniques are currently being developed to elucidate the fundamental aspects of catalytic surfaces under more realistic conditions[12, 13].

1.3 Surface-structure sensitivity

The electronic structure, chemical and surface properties of the catalytic surface are crucial components to thoroughly elucidate the behaviour of catalysts in all aspects, (figure 1.2). Especially in heterogeneous catalysis, the behaviour of the adsorbates depend critically on the surface topography of the metals. Since real nanoparticles (figure 1.1) have a very large variation in surface orientation, determining the active sites is crucial in understanding the role of the catalysts in a catalytic reaction[14]. One way to identify the impact of local structure on chemical reactions occurring on a catalytic surface is to compare reactivity of well-structured, high and low-Miller-index single crystals under well-controlled UHV conditions.

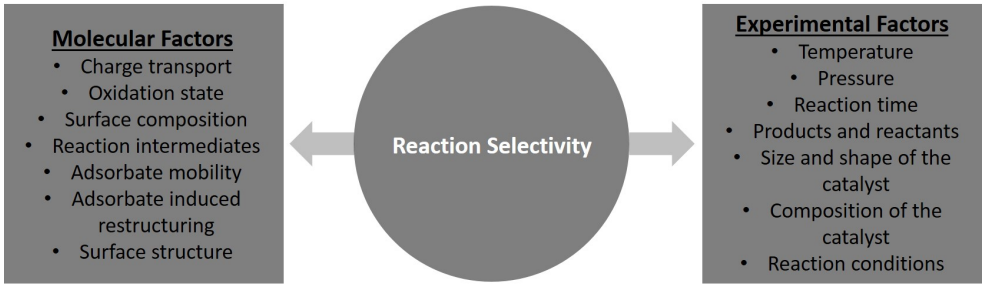

Figure 1.2: Schematic representation of main factors influencing a catalytic reaction[5, 6].

Figure 1.3 shows flat, curved and cylindrical crystals, which are used in surface science studies in our laboratory. The image in the left bottom panel demonstrates the surface orientations adapted from a face centered cubic (fcc) unit cell. [100] and [110] planes occur at angles from the [111] surface of 54.7° and 35.3°, respectively (image in the right bottom panel). Moving away from [111] plane, (100) (clockwise) or (110) (counterclockwise) stepped (111) terraces can be obtained. On flat single crystals, only one particular surface structure is present whereas

on curved or cylindrical crystals, multiple facets can be used in the same vacuum environment.

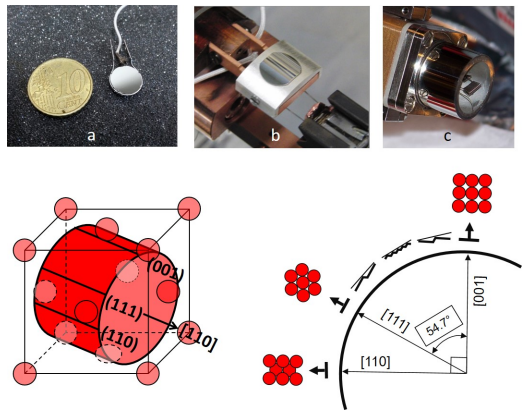

Figure 1.3: a)Flat, b) curved, and c) cylindrical crystals can be used to perform surface science experiments under well-controlled UHV conditions. The schematics in the bottom panel illustrates surface orientations on a curved or cylindrical crystal.

Pt(111) has been the focus of experimental and theoretical surface science studies for the last decades because of its simplicity, figure 1.4a. An ideal (111) plane has an infinite hexagonal structure without any kinks, steps or other defects. On the other hand, real nanoparticles have large number of defect sites, which are more active in bond breaking and making reactions[15], as compared to the (111) plane. This difference between real nanoparticles and well-defined catalysts is known as the materials gap. This drawback in surface science studies can be partially overcome when surfaces with higher step densities, such as Pt(211), Pt(221), Pt(553), Pt(533), are used, as shown in figure 1.4[16]. Therefore, from an experimental point of view, highly stepped surfaces are considered as appealing model systems for a nanoparticle catalyst.

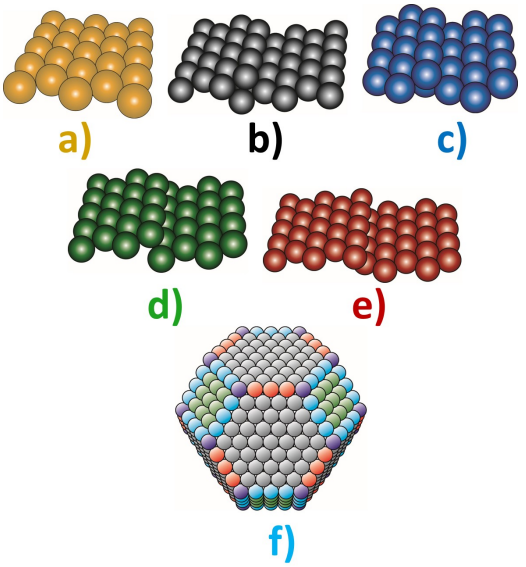

Figure 1.4: a)Pt(111), b) Pt(533), c) Pt(211), d) Pt(221), e) Pt(553) and f) a catalyst nanoparticle.

1.4 Scope

Water is one of the most extensively studied molecules due to its intriguing properties and relevance to many different fields in biology, astrophysics, chemistry, and physics. It is evidently present at many interfaces involving solid surfaces. In this thesis, we focus on the surface structure dependence of water and water-related interfaces on bare and D_2 pre-and-post-covered Pt surfaces. To carry out a more realistic approach, we perform our experiments on highly corrugated Pt surfaces which have similar surface step densities to real nanoparticles. In this research, we use single crystal surfaces and UHV techniques (TPD, LEED and scanning tunneling microscope (STM)) to explore the influences of surface structure on adsorption and desorption of water and related adsorbates.

H_2, O_2, and H_2O are known to be excellent molecules in surface science studies. They represent dissociative (O_2 and H_2)[17, 18] and non-dissociative (H_2O)[19] adsorption with different ranges of activation barriers. In chapter 4, we discuss the adsorption and desorption behaviour of these molecules on a very corrugated surface, Pt(211), (Pt[n(111)x(100)], n = 3). Pt(211) is used as a model surface in many theoretical studies because it has the smallest unit cell containing the (100) step edge. We compare our results on Pt(211) with stepped surfaces with $n > 4$.

The results provide deeper insights in how extreme corrugation on a Pt surface influences the adsorption and desorption characteristics of O_2, H_2 and H_2O. We show that it is crucial to be cautious in extrapolating results from theoretical studies when using Pt(211) as a model substrate to represent Pt[n(111) x (100)] surfaces.

The interaction of water with late transition metals has been reviewed multiple times in great detail[19–21]. It is known that H_2O dosed on Pt(111) below 180 K leads to molecular adsorption without dissociation even when exposed to X-rays[22]. When water is adsorbed on colder surfaces (< 120 K), it forms metastable amorphous solid water (ASW) which crystallizes into crystalline ice (CI) when heated[23, 24]. Recent studies show that the kinetics of this transition significantly depends on the substrate structure. These studies mainly focus on the influence of different metal substrates at very high (50 - 100 ML) coverages[25–27]. In chapter 5, using very thin interfacial water films, we show the significant differences in crystallization kinetics of very similar substrates, Pt(211) and Pt(221). Our results indicate that the thickness of the CI layers depends on the substrate surface. In chapter 6, we compare the crystallization kinetics and isotopic partitioning of D_2 pre-and-post-covered Pt(211), H_2O/D_2/Pt(211) and D_2/H_2O/Pt(211), respectively. We find that isotopic partitioning does not depend on the sequence of dosing. However, the order of dosing influences the crystallization kinetics significantly. D_2 is found to provide a 'smoothing effect' on the corrugated surface when it is dosed first. Also, Pt(211) shows hydrophobic behaviour when D_2 is pre-dosed onto surface. However, the hydrophobicity of the surface does not change when the H_2O covered surface is exposed to hydrogen.

In chapter 7, we study molecular and recombinative O_2 desorption from (110) and (100) stepped Pt(111) surfaces using TPD and STM. We find that (110) stepped Pt(111) terraces trigger dissociative adsorption upon impact at a temperature as low as 100 K. A combination of atomically and molecularly adsorbed oxygen doubles total oxygen coverages for (110) stepped Pt(111) terraces as compared to Pt(111) and Pt(211). (100) stepped Pt also boosts O_2 dissociation by comparison to Pt(111). This, however, results from a trivial geometry effect brought by the steps due to the increased surface area, meaning that the (100) steps provide no extra reactivity.

1.5 Bibliography

References

(1) Wisniak, J. *Educación química* **2010**, *21*, 60–69.

(2) Smith, J. K., *History of catalysis*; Wiley Online Library: 2003.

(3) Chorkendorff, I.; Niemantsverdriet, J. W., *Concepts of modern catalysis and kinetics*; John Wiley & Sons: 2006.

(4) Niemantsverdriet, J. W., *Spectroscopy in catalysis*; John Wiley & Sons: 2007.

(5) Fechete, I.; Wang, Y.; Védrine, J. C. *Catalysis Today* **2012**, *189*, 2–27.

(6) Bisquert, J. *The Journal of Physical Chemistry Letters* **2011**, *2*, 270–271.

(7) Thomas, J. M.; Thomas, W. J., *Principles and practice of heterogeneous catalysis*; John Wiley & Sons: 2014.

(8) Kroes, G.-J. *Physical Chemistry Chemical Physics* **2012**, *14*, 14966–14981.

(9) Nørskov, J. K.; Bligaard, T.; Rossmeisl, J.; Christensen, C. H. *Nature chemistry* **2009**, *1*, 37–46.

(10) Clary, D. C. *Science* **2008**, *321*, 789–791.

(11) Bard, A. J.; Stratmann, M.; Unwin, P., *Encyclopedia of Electrochemistry volume 3: Instrumentation and Electroanalytical Chemistry*; Wiley-VCh: 2003.

(12) Hendriksen, B.; Frenken, J. *Physical Review Letters* **2002**, *89*, 046101.

(13) Van Spronsen, M.; Van Baarle, G.; Herbschleb, C.; Frenken, J.; Groot, I. *Catalysis Today* **2015**, *244*, 85–95.

(14) Nilsson, A.; Pettersson, L. G.; Norskov, J., *Chemical bonding at surfaces and interfaces*; Elsevier: 2011.

(15) Koper, M. T. M. *Nanoscale* **2011**, *3*, 2054–2073.

(16) Van Lent, R.; Jacobse, L.; Walsh, A.; Juurlink, L. B. F. *in preparation.*

(17) Matsushima, T. *Surface Science* **1985**, *157*, 297–318.

(18) Christmann, K; Ertl, G; Pignet, T *Surface Science* **1976**, *54*, 365–392.

(19) Thiel, P. A.; Madey, T. E. *Surface Science Reports* **1987**, *7*, 211–385.

(20) Hodgson, A.; Haq, S. *Surface Science Reports* **2009**, *64*, 381–451.

(21) Henderson, M. A. *Surface Science Rep.* **2002**, *46*, 1–308.

(22) Shavorskiy, A; Gladys, M.; Held, G *Physical Chemistry Chemical Physics* **2008**, *10*, 6150–6159.

(23) Löfgren, P.; Ahlström, P.; Lausma, J.; Kasemo, B.; Chakarov, D. *Langmuir* **2003**, *19*, 265–274.

(24) Smith, R. S.; Huang, C; Wong, E. K. L.; Kay, B. D. *Surface Science* **1996**, *367*, L13–L18.

(25) Löfgren, P; Ahlström, P; Chakarov, D. *Surface Science* **1996**, *367*, L19–L25.

(26) Safarik, D.; Meyer, R.; Mullins, C. *The Journal of chemical physics* **2003**, *118*, 4660–4671.

(27) Smith, R. S.; Matthiesen, J.; Knox, J.; Kay, B. D. *Journal of Physical Chemistry A* **2011**, *115*, 5908–5917.

Chapter 2

The Analysis of Temperature Programmed Desorption Experiments

2.1 Temperature Programmed Desorption (TPD)

TPD is one of the most common techniques in surface science and heterogeneous catalysis. With TPD, desorbed species from a sample can be detected by a quadrupole mass spectrometer (QMS) while the temperature of the sample increases with time. It can provide, amongst others, information regarding the binding energy of the bound species, desorption kinetics, surface coverage and reaction order[1]. The rate of desorption of an adsorbate is given by the following general equation:

$$\mathrm{r}(\theta) = -\frac{\mathrm{d}\theta}{\mathrm{dt}} = \nu_{des}\theta^{\mathrm{n}}\exp(-E_{des}/RT) \tag{2.1}$$

$$\mathrm{T} = \mathrm{T}_0 + \beta t \tag{2.2}$$

r = rate of desorption
θ = coverage in monolayers (ML)
ν_{des} = prefactor
n = order of desorption
E_{des} = activation energy for desorption
R = gas constant
T = temperature (K)
T_0 = initial temperature

β = heating rate
t = time

If the rate of the desorption into the UHV chamber is lower than the pumping speed of vacuum system, the desorption rate is proportional to the pressure rise in the chamber. In a TPD spectrum, the integrated QMS signal is proportional to the amount of adsorbates on the surface and the shape of the desorption feature contains information about the kinetics parameters, including lateral interactions. Although this technique is very simple, cheap and applicable to real crystals, obtaining a high quality spectrum is rather difficult. Also, the interpretation of the data requires meticulous analysis for extracting kinetic information.

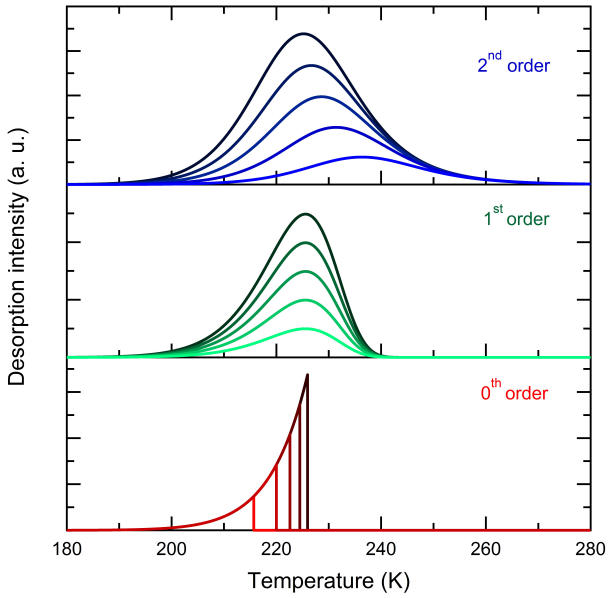

Figure 2.1: Simulated temperature programmed desorption spectra of adsorbed species for initial coverages of 0.2, 0.4, 0.6, 0.8 and 1.0 ML. Top, middle and bottom sections show the second, first and zeroth order desorption, respectively. For each simulation, the activation energy and prefactor are fixed at 60 kJ/mol and 1x10^{13} s^{-1}, respectively.

In figure 2.1, we simulated various TPD spectra at 0.2, 0.4, 0.6, 0.8 and 1.0 ML coverages using rate equation 2.1. Top, middle and bottom sections show second, first and zeroth order of desorption kinetics. For each simulation we set the E_{des} and prefactor at 60 kJ/mol and 1x10^{13} s^{-1}, respectively. In the simulations, the lateral interactions between adsorbed species are ignored.

Zero-order desorption kinetics, for which the rate increases exponentially with temperature and the onsets have a common leading edge, imply a coverage independent desorption rate (bottom panel in figure 2.1). Species which follow zero-order kinetics have a constant coverage and are replenished by another state during desorption. The desorption of water multilayers from clean Pt(111) surfaces is a very well-known example of a zero-order desorption kinetics. For first order desorption kinetics, the rate is proportional to instantaneous coverage and temperature of the peak at maximum desorption rate (T_M) does not increase with increasing coverage (middle panel in figure 2.1). Generally, non-dissociative molecular, e.g., water desorption from Pt(111) terraces at sub-monolayer coverages[2–4], and atomic adsorption, e.g., Xe desorption from graphene[5], yield first order desorption kinetics. For reactions that follow second order desorption kinetics, the rate is proportional to θ^2 (top panel in figure 2.1). With increasing coverage, the peak temperature shifts to lower values while the peaks follow common trailing edges. Molecules that dissociatively-adsorb, e.g., H_2 and O_2[3], on the substrates, generally follow second order desorption kinetics. In the absence of lateral interactions and for well-mixed adlayers, equation 2.1 generally yields accurate results for simple desorption reactions. However, in many adsorption systems lateral interactions between the adsorbates exist. The presence of repulsive or attractive interactions not only make ν_{des} and E_{des} coverage dependent, they can also change the reaction order[6, 7]. Furthermore, the desorption order does not have to be an integer[8] and a TPD spectrum may contain a combination of different desorption orders [9, 10]. To extract accurate kinetic information from TPD spectra, various methods have been developed[7, 11, 12]. In the following sections, some of the most common analysis techniques are discussed.

2.1.1 Redhead analysis

The Redhead analysis[13] is based on the calculation of the activation energy for desorption from the temperature of the peak at maximum desorption rate. Redhead assumed that kinetic parameters are independent of surface coverage and desorption follows first order kinetics. For this method, a very good estimation of the prefactor, ν_{des}, is crucial. Therefore, it is only useful to determine E_{des} when the prefactor is reasonably well known (equation 2.5).

To obtain the Redhead equation, equations 2.1 and 2.2 can be expressed in the following way.

$$\frac{r}{\beta} = \frac{d\theta}{dT} = \frac{\nu_n}{\beta}\theta^n exp(-E_{des}/RT) \tag{2.3}$$

$$\frac{E_{des}}{RT_M} = ln\left(\frac{\nu_n T_M n\theta_M^{n-1}}{\beta}\right) - ln\frac{E_{des}}{RT_M} \tag{2.4}$$

where:
n = 1, and $E_{des} \cong 0.25\ T_M$

$$E_{des} = RT_M[ln(\nu_{des}T_M/\beta) - 3.46] \tag{2.5}$$

2.1.2 Leading edge analysis

This method was introduced by Habenschaden and Küppers[14] and allows the extraction of coverage- and temperature-dependent activation parameters. This method only uses the onset of a TPD spectrum. An Arrhenius plot, ln(r) versus 1/T, yields -E_{des} (slope) and the prefactor (intercept).

Table 2.1: The obtained desorption energies (kJ/mol) and prefactors (s^{-1}) from leading edge (LE) analysis and Redhead analysis at 0.2, 0.4, 0.6, 0.8 and 1.0 ML. For the simulations, E_{des} and prefactors are set to 60 kJ/mol and 1.0x10^{13} s^{-1}, respectively. For extracting the E_{des} from the Redhead equation, the prefactors are set to 1.0x10^{13} s^{-1}.

Method	θ (ML)	Zero order		First order		Second order	
		E_{des}	ν_{des}	E_{des}	ν_{des}	E_{des}	ν_{des}
LE	0.2	60.0	1.0x10^{13}	60.0	1.0x10^{13}	60.0	1.0x10^{13}
Redhead		59.7	—	60.0	—	62.9	—
LE	0.4	60.0	1.0x10^{13}	60.0	8.0x10^{12}	60.0	6.4x10^{12}
Redhead		58.5	—	60.0	—	61.6	—
LE	0.6	60.0	1.0x10^{13}	60.0	6.0x10^{12}	60.0	3.6x10^{12}
Redhead		59.2	—	60.0	—	60.8	—
LE	0.8	60.0	1.0x10^{13}	60.0	4.0x10^{12}	60.0	1.6x10^{12}
Redhead		59.7	—	60.0	—	60.3	—
LE	1.0	60.0	1.0x10^{13}	60.0	2.0x10^{12}	60.0	4.0x10^{11}
Redhead		60.1	—	60.0	—	59.9	—

In table 2.1, we compare the obtained energies from Redhead and leading edge techniques for 0.2, 0.4, 0.6, 0.8 and 1.0 ML. For determining E_{des} from the Redhead equation, the prefactor is set to 1x10^{13} s^{-1}. In our simulation we have used 1000 data points per 1 K. We are aware that obtaining such high quality TPD data from an experiment is nearly impossible due to various reasons, i.e. QMS

sensitivity[15], experimental difficulties, etc. However, to compare the analysis techniques accurately, such a high quality simulation is essential.

Extracting desorption energies using the leading edge technique results in accurate results for the three different desorption orders (2.1). However, the pre-exponential factors obtained by this method change dramatically with the desorption order. For zero order desorption kinetics, it gives precise values for E_{des} and ν_{des}. However, for the first and second order desorption kinetics, it generates spurious results especially at large coverages. The Redhead model only seems accurate when desorption follows first order kinetics on the condition that a correct estimation for the prefactor is made. This is expected as this model is based on T_M, which is sufficiently constant at n = 1 (equation 2.1). Note that even for the first order desorption kinetics, an inaccurate ν_{des} can lead to incorrect desorption energies and prefactors. For example, the error introduced through a prefactor of $1x10^{12}$ s^{-1} is more than 10 % for n = 1.

2.1.3 Complete analysis

The complete analysis yields coverage-dependent desorption energies. Applying the Polanyi-Wigner equation (equation 2.1) on a set of TPD spectra, E_{des} and ν_{des} can be derived at a fixed coverage. This approach is generally useful for extracting kinetic information from single desorption features[11], where deconvolution of the TPD peaks is not required. In the following sections, we will elaborate more on this technique.

In figure 2.2a, we plotted the coverages versus the temperature for for n = 0, 1, and 2. The coverages are calculated by integrating each spectrum in figure 2.1. It is emphasised by dotted, horizontal lines that each spectrum has a different temperature and a different TPD rate at a certain coverage. When ln(r) vs. 1/T is plotted for each fixed coverage (0.1 - 0.8 ML), the slope and the intercept will yield E_{des} and $\ln(\nu_{des})$ + n×ln(r), respectively. Figure 2.2b shows that the complete analysis technique produces more accurate E_{des} and ν_{des} for zero, first and second order desorption, by comparison to previously mentioned methods (table 2.1).

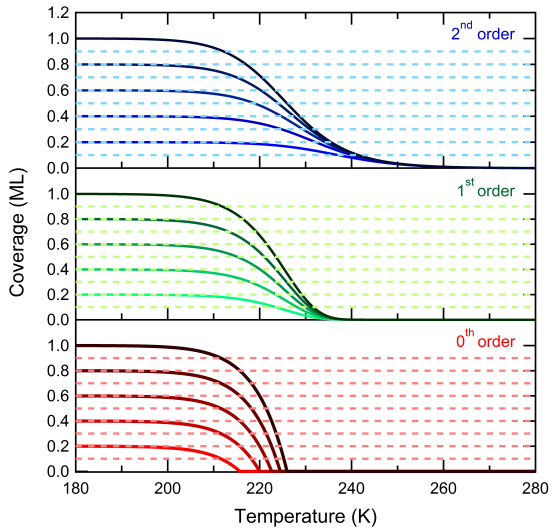

(a)

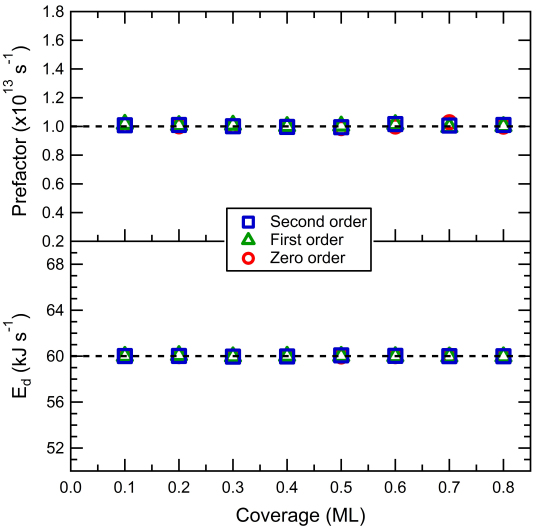

(b)

Figure 2.2: With complete analysis, coverage dependent E_{des} and ν_{des} can be calculated. a) Coverages, obtained from figure 2.1, versus temperature for different desorption orders. The dotted lines indicates the fixed coverages. b) Calculated desorption energies and prefactors using complete analysis method for different desorption orders. The dotted lines are the simulated E_{des} and ν_{des}.

Although precise E_{des} and ν_{des} can be derived from simulated data using complete analysis, a kinetic analysis of experimental TPD data is more complicated. For instance, low signal to noise ratio, non-integer desorption orders[10] and difficulties in background subtraction may strongly influence the accuracy of kinetic calculations. For the complete analysis method, the difficulties in obtaining a set of TPD spectra in a limited coverage regime[9] may result in a discontinuity in E_{des} as a function of coverage. Also, most molecules give rise to a TPD spectrum with multiple desorption features. For the methods mentioned above, the analysis of TPD spectra with multiple peaks generally requires deconvolution, which may result in large errors, due to the difficulties in estimating the onset.

2.1.4 Inverse optimization

Tait et al.[16] have proposed an inverse optimization technique that yields accurate results when multiple desorption features are present in the TPD spectrum. Similar to complete analysis, this method also provides coverage dependent E_{des}. The prefactor, however, is not dependent on the coverage and the temperature. With the inverse optimization technique a continuous E_{des} can be calculated as a function of coverage. The following expression (equation 2.6) is used for the inverse optimization technique for n = 1.

$$\mathrm{E}_{des}(\theta) = -\mathrm{RTln}[\frac{d\theta/dt}{\nu_{des}\theta}] \tag{2.6}$$

To illustrate this method, we show simulated TPD spectra with two desorption features in figure 2.3. For the high temperature peak, at $\sim$ 155 K, we fixed E_{des} and ν_{des} at 40.0 kJ/mol and 1.0x10^{13} s^{-1}, respectively. For the low temperature features, at 130 K, E_{des} and ν_{des} are fixed at 30 kJ/mol and 1.0x10^{11} s^{-1}, respectively. In our simulation for low and high temperature features, first and second order desorption kinetics are chosen, respectively.

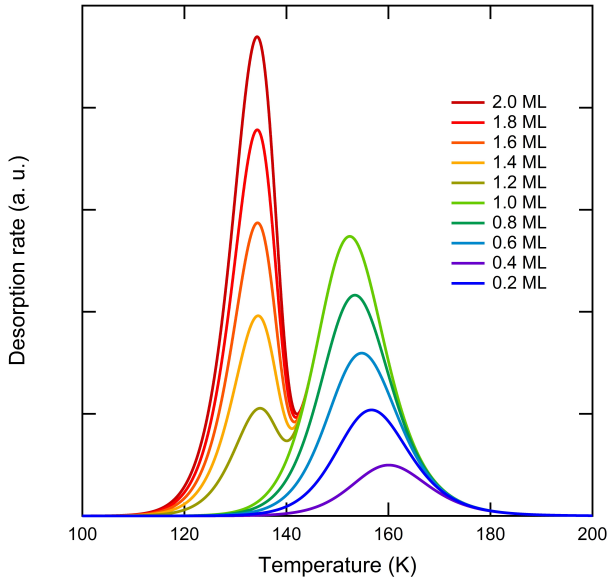

Figure 2.3: Simulated temperature programmed desorption spectra of adsorbing species for coverages up to 2.0 ML. We used first order desorption kinetics with E_{des} = 30 kJ/mol and ν_{des} = 1.0x10^{11} s^{-1} for the low temperature features. For the high temperature peaks, we simulated the data with the following parameters: n = 2, E_{des} = 40.0 kJ/mol and ν_{des} = 1.0x10^{13} s^{-1}.

Similar to a TPD spectrum with a single desorption feature, the kinetics of the low temperature peak in figure 2.3 can be determined accurately using the leading edge analysis. Using the leading edge technique, we obtain an average desorption energy and prefactor of 30.0 kJ/mol and 1.0x10^{11} s^{-1}. These values agree well with the tabulated results. In the following section we elucidate how the inverse optimization method can be applied to the high temperature peak.

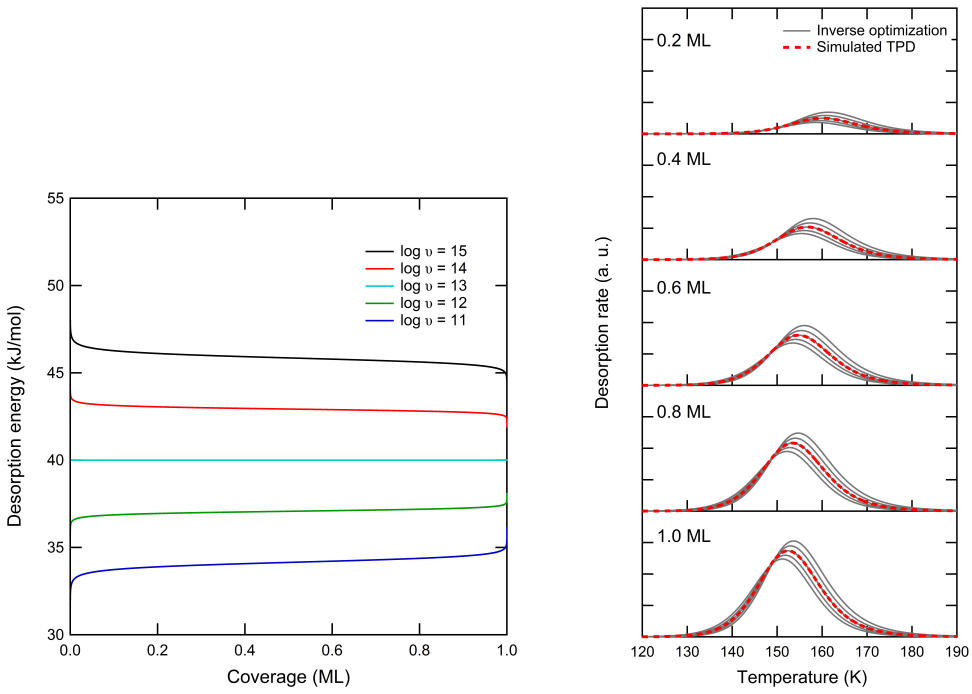

(a) (b)

Figure 2.4: Inverse optimization method[16] can provide a kinetic analysis with minimum discrete points. a) Equation 2.6 leads to various desorption energies when different approximations for the prefactor are made, 10^{11}, 10^{12}, 10^{13}, 10^{14} and 10^{15} s^{-1}. b) TPD models (solid curves) derived from using the prefactors and corresponding E_{des} shown in figure 2.4a. The dotted curves show simulated desorption features (figure 2.3) at 0.2, 0.4, 0.6, 0.8 and 1.0 ML.

Figure 2.4a displays coverage dependent desorption energies using equation 2.6 with different prefactors, 10^{11}, 10^{12}, 10^{13}, 10^{14} and 10^{15} s^{-1}. Each energy plot is obtained using the Polanyi-Wigner equation (equation 2.1). Using the energy curves obtained in figure 2.4a, we created TPD models with different prefactors. In figure 2.4b, the generated TPD models (solid black curves) are compared with the high temperature features of the simulated data (red dotted curves) from figure 2.3. With this methodology, a reliable prefactor, which does not vary with θ, can be determined.

To derive a quantitatively accurate prefactor, in figure 2.5 we have calculated a χ^2 error between the modelled and simulated TPD spectra for each coverage in figure 2.4b. χ^2 error is the sum of the squares of the leftovers compared to

simulation. The solid horizontal line in figure 2.5 expresses $\chi^2 = 0$. The dotted curve is a polynomial fit through the data, which reveal a minimum at $\log\nu_{des}$ = 13. As figure 2.4b also indicates, the most accurate prefactor calculated by inverse optimization method is 10^{13} s^{-1}. Therefore, the E_{des} curve plotted in figure 2.4a for $\log\nu_{des} = 13$ (light blue) represents the actual coverage dependent desorption energy for the high temperature desorption feature (figure 2.3). Figure 2.4a shows that the obtained desorption energy is 40 kJ/mol, and does not change with increasing coverage. These results agree perfectly with the parameters set to generate the simulated data.

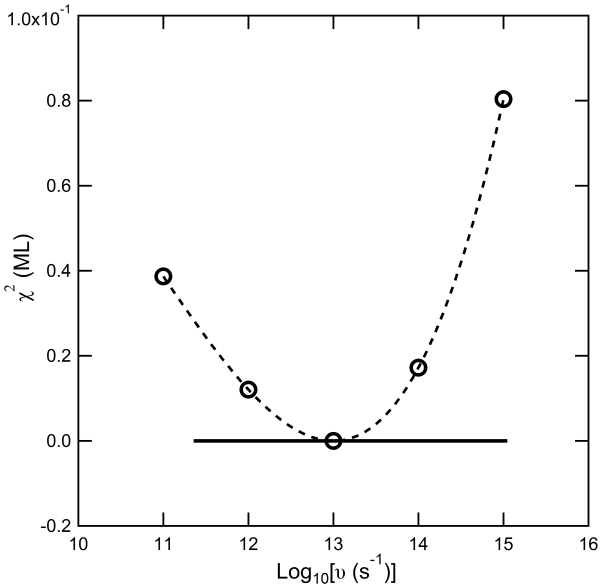

Figure 2.5: The χ^2 error between the modelled and simulated TPD spectra as shown in figure 2.4b. The dotted line indicates the minimum of the polynomial fit (solid line) to the data.

2.2 Conclusions

To conclude, we have compared the most common methods to derive the activation energy and prefactor using very high quality TPD data. With leading edge analysis accurate E_{des} for zero, first and second order desorption kinetics can be obtained when the spectrum consists of a single desorption feature. However, this method fails to derive a correct prefactor for n = 1 and 2. The Redhead analysis should generally be avoided as a small variation in estimating the prefactor may

cause a significant error. Finally, both complete analysis and inverse optimization method generate precise kinetic information. However, the latter yields continuous E_{des} with no discrete points as a function of coverage. Therefore, it may be favored over complete analysis.

2.3 Bibliography

References

(1) Niemantsverdriet, J., *Spectroscopy in Catalysis: An Introduction*; Wiley: 2000.

(2) Van der Niet, M. J. T. C.; Dominicus, I.; Koper, M. T. M.; Juurlink, L. B. F. *Physical Chemistry Chemical Physics* **2008**, *10*, 7169–7179.

(3) Van der Niet, M. J. T. C.; den Dunnen, A.; Juurlink, L. B. F.; Koper, M. T. M. *Journal of Chemical Physics* **2010**, *132*, 174705–174713.

(4) Van der Niet, M. J. T. C.; den Dunnen, A.; Juurlink, L. B. F.; Koper, M. T. M. *Physical Chemistry Chemical Physics* **2011**, *13*, 1629–1638.

(5) Smith, R. S.; May, R. A.; Kay, B. D. *The Journal of Physical Chemistry B* **2015**, *120*, 1979–1987.

(6) Pfnür, H; Feulner, P; Engelhardt, H.; Menzel, D *Chemical Physics Letters* **1978**, *59*, 481–486.

(7) Kolasinski, K. K.; Kolasinski, K. W., *Surface Science: foundations of catalysis and nanoscience*; John Wiley & Sons: 2012.

(8) Van Spronsen, M. A.; Weststrate, K.-J.; den Dunnen, A.; van Reijzen, M. E.; Hahn, C.; Juurlink, L. B. F. *The Journal of Physical Chemistry C* **2016**, acs.jpcc.6b00912.

(9) Badan, C.; Koper, M. T. M.; Juurlink, L. B. F. *The Journal of Physical Chemistry C* **2015**, *119*, 13551–13560.

(10) Radeke, M. R.; Carter, E. A. *Physical Review B* **1996**, *54*, 11803–11817.

(11) Nieskens, D.; van Bavel, A.; Niemantsverdriet, J. *Surface Science* **2003**, *546*, 159–169.

(12) Niemantsverdriet, J. W., *Spectroscopy in catalysis*; John Wiley & Sons: 2007.

(13) Redhead, P. A. *Vacuum* **1962**, *12*, 203–211.

(14) Habenschaden, E; Kuppers, J *Surface Science* **1984**, *138*, 147–150.

(15) Janlamool, J.; Bashlakov, D.; Berg, O.; Praserthdam, P.; Jongsomjit, B.; Juurlink, L. B. F. *Molecules* **2014**, *19*, 10845–10862.

(16) Tait, S. L.; Dohnalek, Z; Campbell, C. T.; Kay, B. D. *Journal of Chemical Physics* **2005**, *122*.

Chapter 3

Experimental Set-up

3.1 Set-up

The experiments in this thesis were carried out using a custom-built vacuum (UHV) surface science chamber, called SHRIMP[1–3] (no acronym). It has a base pressure of 5x10 $^{-11}$ mbar and is equipped with two quadrupole mass spectrometers (QMS). One QMS (Baltzers, Prisma 200) protrudes into the main chamber and is mainly used for residual gas analysis (RGA). Figure 3.1 shows typical residual gases (hydrogen, water, CO, and CO_2) in our set-up after a bakeout. The other QMS (Balzers QMA 400) is kept in a differentially pumped canister that connects to the main UHV chamber via a circular spot with a radius of 2.5 mm, figure 3.2. It is positioned 2 mm from the face of the samples (Surface Preparation Laboratory, Zaandam, the Netherlands) during TPD studies.

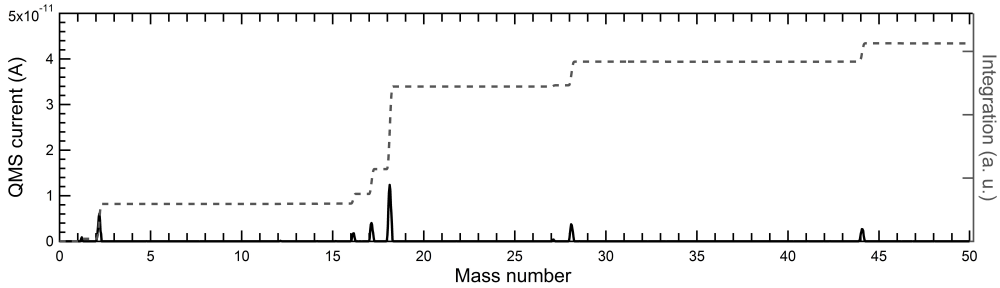

Figure 3.1: A typical residual gas analysis (RGA) after a bakeout shows the corresponding masses for H_2, H_2O, CO, and CO_2.

SHRIMP also contains a sputter gun (Prevac IS40C-PS) and LEED optics (VG

RVL 900). It has three directional dosers, which provide localized effusive dosing onto the sample. Our flat samples are 1 or 2 mm thick with 10 mm diameter, with a purity better than 5N and a an orientation alignment better than 0.1°. The sample can be cooled to 88 K using liquid N_2. Heating can be done radiatively by a filament (Osram, 150 W) mounted behind the sample. Samples can be also heated by electron bombardment using a positive voltage on the crystal assembly while the filament is grounded. For the crystals, temperature is measured with a type-K thermocouple laser welded to the top edge of the samples. For the temperature control, we use a PID controller (Eurotherm 2416) from which the thermocouple is electrically decoupled.

For TPD experiments the heating rate is 0.9 K s^{-1} over a temperature range of 250 K. H_2O from a Millipore Milli-Q gradient A10 system (18.2 MΩ cm resistance) was kept in a glass container and cleaned using multiple freeze-pump-thaw cycles. Before each set of experiments, these cycles were repeated to make sure that water has no contaminants. The glass container was exposed to 5.0 bar He (Linde gas, 5.0). For water and O_2 TPD, the adsorption temperature is below 100 K. To avoid adsorbing H_2 or other residual gases on the surfaces, D_2 is dosed while cooling the sample, between 700 - 100 K. A blank TPD experiment did not yield any H_2, D_2, H_2O or O_2 desorption. To provide minimum contamination on the surface, we turned off all filaments while dosing.

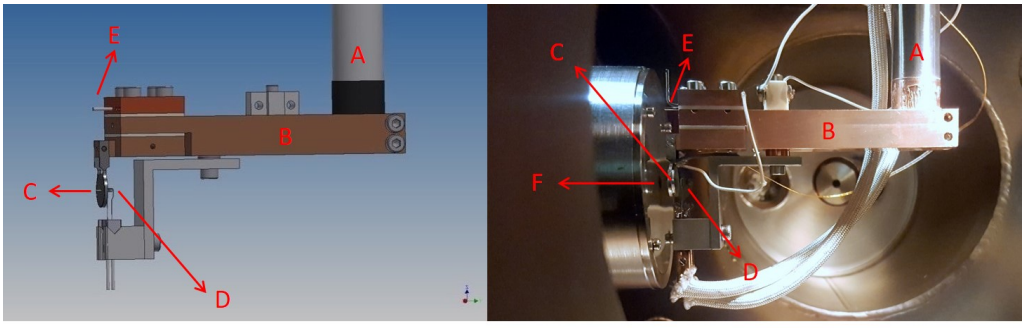

Figure 3.2: TPD studies are performed with a differentially pumped QMS. For the experiments, the samples are positioned 2 mm from the QMS. In our setup, a cryostat manipulator (A) is connected to a copper sample-holder (B). A 150 W filament (D) is attached behind the sample (C). The distance of the sample to the QMS canister (F) is reproduced using a pin (E).

3.2 Temperature programmed desorption

For an accurate kinetic analysis (see chapter 2), a proper background subtraction is needed. Especially when water is dosed onto a sample, we find that stainless steel will also adsorb water. The high vacuum time constant of water results in an increase in the baseline of the water TPD spectra. To remove this effect, we use the following approximation, equation 3.1, to define the baseline (y).

$$\mathrm{y}=\mathrm{y}_0+\frac{1}{2}\triangle\mathrm{y}\times\left(\tanh\left(\frac{T-T_0}{\triangle T}\right)+1\right) \tag{3.1}$$

$\triangle$y = total increase in the height of baseline

T_0 = center of the S-curve (an s-shaped function with finite limits at negative and positive infinities) before T_M

$\triangle$T = arbitrary parameter to smooth out the tanh

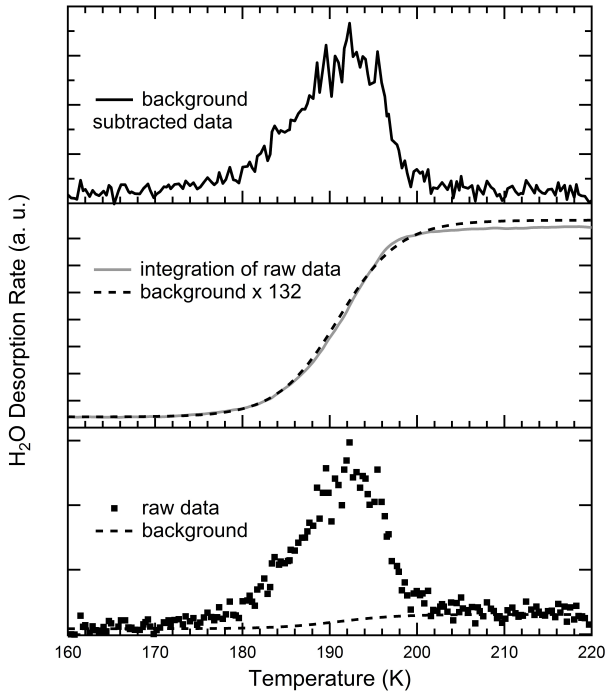

Figure 3.3: Because water sticks to the stainless steel walls of the chamber, the vacuum time constant of H_2O yields an increase in the background of water TPD spectra. An accurate approximation to subtract this baseline is given in equation 3.1. The bottom panel shows a TPD spectrum of water from Pt(211). The middle panel compares the approximation derived by using equation 3.1 with the integrated TPD spectrum. The top panel show the background subtracted spectrum.

Figure 3.3 exemplifies the background subtraction process for a TPD spectrum[4, 5]. In the bottom panel, we obtain a baseline using the approximation described above (equation 3.1). In the middle panel, we compare the baseline curve with the integrated TPD spectrum. As the integral reflects the development of the TPD curve at any point in time, it is crucial that the shape of the baseline curve develops similarly to the TPD spectrum. The top panel shows the baseline subtracted TPD spectrum. We verified that this method does not influence the baseline of the leading edges. In this thesis, all spectra are baseline corrected.

3.3 Low energy electron diffraction

Low electron energy diffraction (LEED) is a very common technique used to determine the surface structure. It uses a well-defined normal incidence of the primary electron beam on the sample. The electrons are scattered back elastically from the well-ordered surface crystallography in all directions. Diffracted electrons are selected by energy filtering grids, before landing on the phosphorescent screen. The well-ordered structure of the surface creates a direct image of the reciprocal lattice of the surface[6, 7].

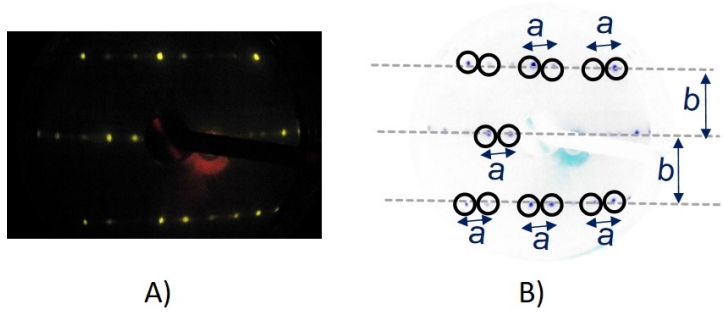

Figure 3.4: Raw (A) and color-inverted (B) LEED images of a clean Pt(221). The average ratio of spot row spacing b over spot splitting a yields 3.06. This agrees well with literature value of 3.00[8].

The surface structure type can be determined by row spacing to spot splitting ratio[8]. In figure 3.4, we show an exemplary picture of a LEED pattern created by a clean Pt(221) surface. From this image we extract a row spacing over spot splitting ratio of 3.06, which is in good agreement with the tabulated value of 3.00[8]. This agreement indicates long-range order with the expected average terrace width. We repeated the same analysis for other samples (Pt(111), Pt(211), Pt(221), Pt(533) and Pt(553)) used in this research and also found excellent agreements with literature values.

In addition to average terrace width, the step height can also be determined with LEED. This analysis is done by assigning the electron energies (E_{el}) at which the (00) beam shows singlets and doublets[9]. Henzler[10] derived a means to determine the step height as a function of energy as shown in equation 3.2.

$$V_{00} = \frac{150}{4} \times \frac{s^2}{d^2} \tag{3.2}$$

where V_{00} is the energy of the incoming electrons in eV, d is the step height in Å and s is an (unknown) integer for singlet spot appearance and half integer for doublet spot appearance.

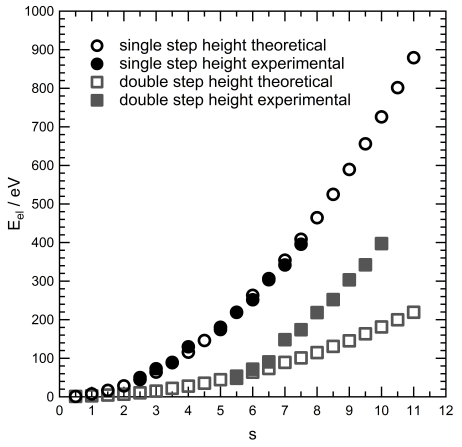

Figure 3.5: The step height analysis of Pt(533) using equation 3.2. Open circles: theoretical values of E_{el} for s with one-atom high steps. Open squares: theoretical values of E_{el} for s with two-atom high steps. Closed circles and squares are the fit of experimental data for s with one and two atomic high steps, respectively[11].

Figure 3.5 compares the theoretical and experimental energies of different s for single and double step heights on Pt(533), equation 3.2. The open circles and open squares are theoretical energies at various values of s for both one and two atom high steps, respectively. The closed circles and closed squares shows the obtained experimental E_{el} for single and double step heights[11]. The figure clearly shows that the circles coincide accurately whereas the squares do not. This analysis proves that Pt(533) consists of steps separated by single atoms. Applying the same (00) analysis on different spots of the sample confirms that the anticipated structure is well-defined over the entire crystal. With the same method, we confirmed that all the high-miller-index samples used in this thesis have monoatomic step height.

3.4 Bibliography

References

(1) Badan, C.; Koper, M. T. M.; Juurlink, L. B. F. *The Journal of Physical Chemistry C* **2015**, *119*, 13551–13560.

(2) Badan, C.; Heyrich, Y.; Koper, M. T. M.; Juurlink, L. B. F. *The Journal of Physical Chemistry Letters* **2016**, 1682–1685.

(3) Badan, C.; Farber, R. G.; Heyrich, Y.; Koper, M. T.; Killelea, D. R.; Juurlink, L. B. *The Journal of Physical Chemistry C* **2016**, *120*, 22927–22935.

(4) Van der Niet, M. J. T. C.; den Dunnen, A.; Juurlink, L. B. F.; Koper, M. T. M. *Journal of Chemical Physics* **2010**, *132*, 174705–174713.

(5) Van der Niet, M. J. T. C.; den Dunnen, A.; Juurlink, L. B. F.; Koper, M. T. M. *Physical Chemistry Chemical Physics* **2011**, *13*, 1629–1638.

(6) Ellis, W. P. *Surface Science* **1974**, *45*, 569–584.

(7) Ellis, W. P.; Schwoebel, R. L. *Surface Science* **1968**, *11*, 82–98.

(8) Vanhove, M. A.; Somorjai, G. A. *Surface Science* **1980**, *92*, 489–518.

(9) Mom, R. V.; Hahn, C.; Jacobse, L.; Juurlink, L. B. *Surface Science* **2013**, *613*, 15–20.

(10) Henzler, M *Surface Science* **1970**, *19*, 159–171.

(11) Van der Ham, K. Working Towards Ethanol Dissociation on Pt(533)., MA thesis, the Netherlands: Leiden Institute of Chemistry, Leiden University, 2013.

Chapter 4

How well Does Pt(211) Represent Pt[n(111)x(100)] Surfaces in Adsorption/Desorption?

4.1 Abstract

We have investigated to what extent Pt(211) is representative for Pt[n(111)x(100)] surfaces in adsorption/desorption behavior of water, hydrogen, and oxygen through temperature programmed desorption. In contrast to surfaces with n > 3, H_2O adsorbs to Pt(211) in a crystalline fashion far below the usual crystallization temperature of amorphous solid water. For D_2, we find that desorption from (100) steps is independent of terrace length for n ≥ 3, but desorption from the neighboring (111) terraces varies. Larger terraces result in larger variations in binding energies as a consequence of decreasing proximity of adsorption sites to the step edge. For O_2, we observe enhanced dissociation on Pt(211) resulting in a much larger maximum O-coverage than surfaces with n > 3. The TPD characteristics suggest formation of 1-

dimensional PtO_2 structures, which are only formed for n=3 with this (100) step type. Hence, Pt(211) can by no means be considered representative of Pt(111) terraces truncated by (100) steps. Our results stress that great caution is required when extrapolating results from theoretical studies based on this smallest unit cell containing the (100) step edge to catalysis by actual particles.

Based on: Badan, C.; Koper, M. T. M.; Juurlink, L. B. F., J. Phys. Chem. C 2015, 119, 13551-13560.

4.2 Introduction

As an exceptional catalyst for industrial, automotive and fuel cell catalysis, platinum has been the subject of numerous theoretical and experimental studies. Because of its multiple uses, global production and consumption of platinum has increased intensely in the last 30 years although it remains one of the most expensive precious metals[1]. To reduce costs, Pt either needs to be replaced by an alternative, less expensive catalyst material or its catalytic activity needs to be enhanced to lower the required volume while achieving the same kinetic rates. For the latter, it is vital to improve our understanding of structure-activity and structure-selectivity relations[2]. One way to elucidate the influence of local surface structure to chemical reactions is to compare reactivity of various well-defined, high and low-Miller-index single-crystal catalyst surfaces under well-controlled conditions.

Prototypical surface science and gas-surface dynamics studies for Pt involve CO, H_2, O_2 or H_2O. In this paper, we focus on the adsorption and desorption of the latter three molecules. These three molecules prove to be excellent probes as they represent for Pt(111) and its vicinal surfaces both non-dissociative (H_2O[3, 4]) and dissociative adsorption (O_2[5, 6] H_2[7, 8]) with varying ranges of activation barriers and either directly dissociating (H_2[9, 10]) or passing through well-defined intermediate states (O_2[11, 12]). In addition, they yield adsorbates with both weak (H) and strong lateral interactions (O), also leading to large variations in maximum surface coverage. For the infinite (111) terrace, the maximum coverage is 1 H/Pt[7] while for O it is 0.25 O/Pt atom[13] using, respectively, H_2 and O_2 as gaseous reactants. Beyond attractive or repulsive interaction, H_2O tends to form long-range networks on Pt(111)[14].

It has been shown that the geometry of the step type may have varying effects on adsorption, ranging from inducing hydrophobic vs hydrophilic behavior for co-adsorbed D and H_2O[15] and preferring O vs OH adsorption at the step edge for co-adsorbed O and H_2O[16]. We now investigate whether *terrace width* is a second parameter that must be explicitly treated in theoretical modelling of platinum catalysis. Here, we use the same three probe molecules and temperature programmed desorption (TPD) as our main technique. In particular, we focus on differences observed for Pt surfaces containing the (100) step edge. The (211) surface, also indicated as [3(111)x(100)] in the van Hove-Somorjai notation[17], is often taken as the reference for (100) step edge effects in DFT studies comparing binding energies and activation barriers to dissociation on (111) (e.g. refs[18–20]). We will show that the (211) surface shows significant differences from [n(111)x(100)] surfaces for $n > 3$ and conclude that (211) is not a surface that can be chosen to generally represent structural effects for (100) step edges.

4.3 Experimental

Experiments are carried out using a custom-built vacuum (UHV) surface science chamber which is primarily used for LEED and TPD studies. The system and our standard procedures have been described elsewhere[21, 22]. This system has a base pressure of 5×10^{-11} mbar. The chamber is equipped with two quadrupole mass spectrometers (QMS). One QMS (Baltzers, Prisma 200) protrudes into the main chamber and is mainly used for residual gas analysis (RGA). The other QMS (Baltzers QMA 400) is kept in a differentially pumped canister that connects to the main UHV chamber via a circular spot with a radius of 2.5 mm. The crystal is positioned 2 mm from the face of the sample during TPD studies. The apparatus also contains, amongst others, a sputter gun (Perkin Elmer 20-045) and LEED optics (VG RVL 900). Lastly, it contains three directional dosers which provide localized effusive dosing onto the sample. For the experiments described in this paper, single-crystals, (Surface Preparation Laboratory, Zaandam, the Netherlands) are 1 or 2 mm thick and 10 mm in diameter. The sample can be cooled to ∼95 K by pouring LN2 into the cryostats reservoir. The crystals are heated radiatively by a filament (Osram, 250 W) mounted behind the sample. Samples can be also heated by electron bombardment using a positive voltage on the crystal assembly while the filament is grounded. For the crystals, temperature is measured by a type-K thermocouple laser welded to the top edge of the samples. For temperature control, we use a PID controller (Eurotherm 2416) from which the thermocouple is electrically decoupled.

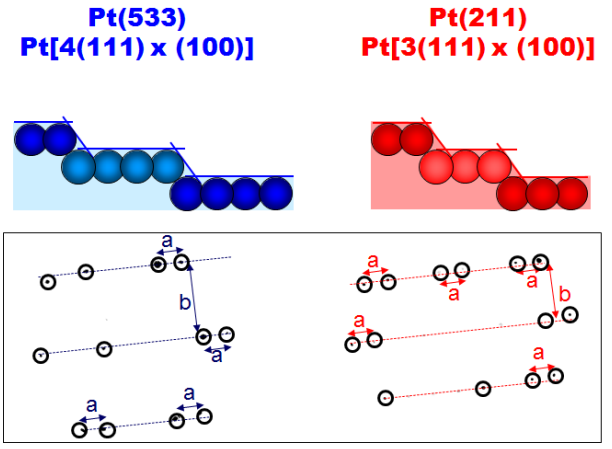

Figure 4.1: Schematic side views (top) and inverted LEED patterns (bottom) of clean Pt(533) (left) and Pt(211) (right).

Crystals are cleaned by repetitive sputtering-annealing cycles. We sputter using Ar^+ (Messer, 5.0) at 500 V and 2 μA for 20 minutes and anneal at 900 K in an O_2 atmosphere (5×10^{-8} mbar) for 5 minutes. Finally we anneal the crystal at 1200 K for 5 minutes. LEED was periodically used to check surface order. The top panel of figure 4.1 shows schematic side view representations of the Pt(533) and Pt(211) that consists of 4 and 3 atom wide (111) terraces with (100) steps, respectively. The bottom panel shows the LEED spots from color-inverted photos taken of the LEED diffraction patterns after cleaning these surfaces. From these images, we deduce spot row spacing to spot splitting ratios (indicated by the dotted lines and double-headed arrows) of 3.24 for Pt(533) and 2.38 for Pt(211). These values correspond well to the literature values of 3.28 and 2.45[17].

Water (Millipore, 18.2Ω) was dosed onto our Pt crystals using a custom-built 10 mm diameter capillary array doser at a distance large enough to ensure a uniform flux across the entire cleaned surface[23]. The water was degassed by multiple freeze-pump-thaw cycles and backfilled with 1.1 bar He (6N, Air Products) prior to experiments. Water, D_2 (Linde 2.8) and O_2 (Messer, 5.0) are dosed directly onto the surface with $T_s \leq 100$ K. During dosing all filaments were switched off to minimize contamination by H atoms. The gases were generally dosed onto the crystal for different durations at a fixed pressure. The pressure is determined by an uncalibrated cold cathode gauge. For all TPD experiments, the sample was heated with ~ 0.9 K s^{-1} to a temperature well above completion of desorption. Subsequently, the sample is annealed to 1200 K again for 5 minutes. For experiments involving D_2, m/z = 2 (H_2), 3 (HD) and 4 (D_2) were monitored. We found no significant desorption of H_2 and HD. Baseline correction and fitting procedures are described in detail elsewhere[16, 24].

To determine the absolute coverages for H_2O, and O_2 we used flat Pt(111) as reference. In chapter 5 and 7, we explain our reference method in greater detail. For deuterium, the maximum integrated TPD signal is set to a saturation value of 0.9 ± 0.05 ML as reported previously[25]. To obtain kinetic parameters, we have attempted to apply several methods. A complete analysis[26] for D_2, H_2O, and O_2 unfortunately yields unreliable results as trailing edges show significant overlap. Minor variations in the background subtraction affect the onset for the individual TPD features too strongly to obtain consistent desorption energies and frequency factors using a leading edge analysis[27]. The inversion-optimization method[28] can only be applied to a spectrum of multiple peaks when those represent a single desorption order. This seems not to be the case in our spectra. Our attempts to separate the individual peaks and analyze them individually did not result in a determination of kinetic parameters with a significant degree of accuracy.

4.4 Results and discussion

4.4.1 Water

Figure 4.2 shows TPD spectra of H_2O desorbing from the clean Pt(211) surface. Water desorption is characterized by two main features. The maximum rate of desorption for the higher temperature peak appears at ∼193 K. For the lower temperature peak, it shifts from 150 to 165K for these coverages. The onset of desorption appears at ∼140 K. We do not observe an explicit desorption peak appearing between 170 and 180 K as is generally observed for Pt[n(111)(100)] surfaces with n≥4[29]. Based on previous studies, the low and high temperature desorption peaks may be attributed respectively to desorption of water molecules from the second or consecutive water layers[16, 29, 30], and molecules in contact with the bare Pt surface, in particular the (100) step sites[16, 29]. In comparison to other Pt surfaces with the same step type but wider terraces, we find significant differences that deserve a detailed comparison.

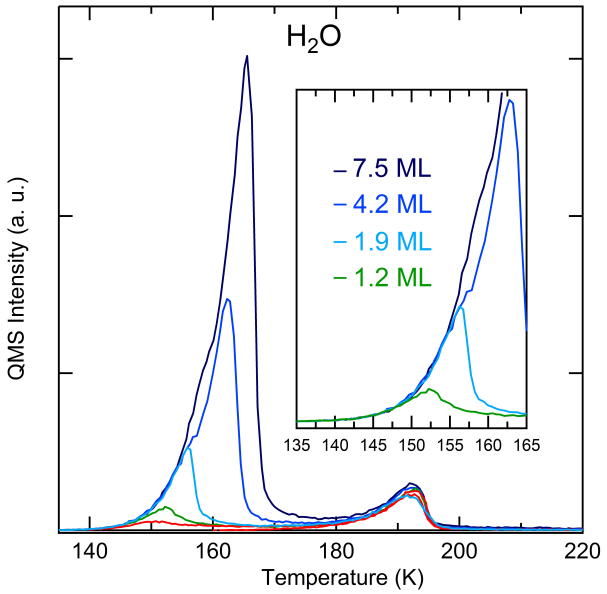

Figure 4.2: TPD spectra of various amounts of H_2O desorbing from clean Pt(211) at 0.9 K s^{-1}.

The multilayer desorption peak appears only after saturation of the high temperature peak. Although it exhibits characteristics of 0^{th}-order desorption kinetics, the inset shows that the second and consecutive water layers are not equi-

valent. For coverages between 1 and 2 ML, leading edges overlap perfectly. For coverages larger than 2 ML, leading edges also overlap but clearly show a steeper onset than for the second water layer. The latter TPD spectra also exhibit the characteristic deflection at ∼158 K in desorption rate that indicates crystallization of amorphous solid water (ASW) to crystalline ice (CI) during the temperature ramp[31–33]. We find no evidence of a crystalline layer from LEED measurements.

Finally, the leading edges for the lower temperature desorption of coverages between 1 and 2 ML align perfectly with the desorption rate for $>$ 2 ML after crystallization. From these results, we conclude that the second layer of H_2O on Pt(211) is of a crystalline nature prior to the onset of desorption. As it seems unlikely that a crystalline layer forms on top of a disordered layer, the water layer directly in contact with the Pt(211) substrate, which desorbs around 200 K, is expected to be crystalline at the onset of desorption of the second layer. Although our current data does not exclude that crystallization occurred during the temperature ramp between 100 and 140 K, we see no reason why this would involve only the first two layers and leave thicker layers as ASW to be crystallized only around 158 K. Hence, we believe that the surface structure of Pt(211) induces crystalline water growth at 100 K already with the second water layer also being of crystalline. The third and consecutive layers grow at 100 K as ASW on top of this crystalline structure. Although similar water growth has been observed, e.g. for ASW growth on top of a single CI layer on Pt(111)[34–37], we believe the observed behavior involving two crystalline water layers prior to ASW growth at such a low surface temperature is unique. We have attempted to find additional diffraction spots using LEED for various water coverages but found none.

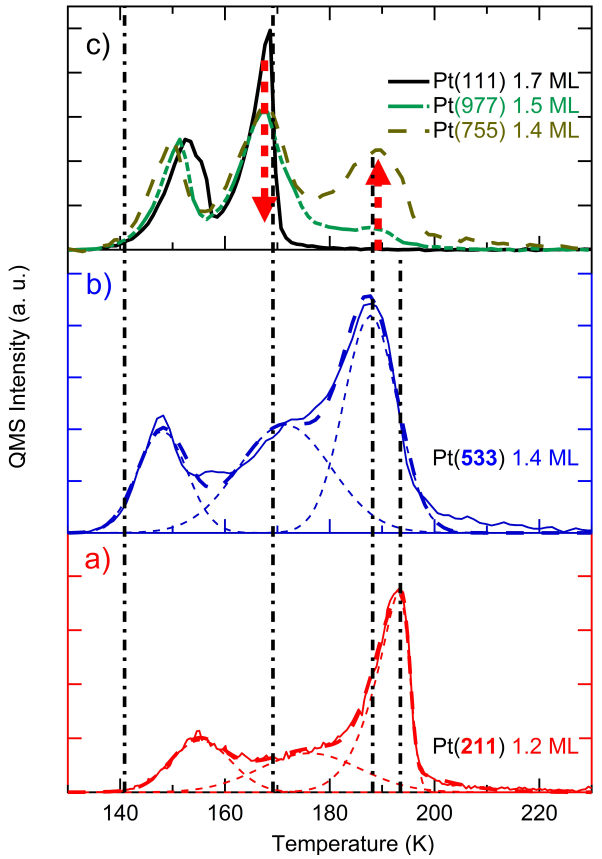

Figure 4.3: Comparison of H_2O TPD spectra for a) Pt(211) b) Pt(533) and c) Pt(755), (977) and (111)[29]. The dashed-dotted vertical lines guide the eye. Arrows indicate peak progression upon increasing step density.

Figure 4.3 compares TPD spectra of H_2O desorbing from Pt(533) and Pt(211), middle and bottom sections, respectively. In the top panel, we also show our TPD spectra of H_2O from Pt(111), Pt(977) and Pt(755)[29]. The dotted lines in the data for Pt(533) and Pt(211) represent the three desorption peaks from a fitting procedure on the basis of three modified Gaussian functions to model desorption of water in different environments. These components are used for qualitative comparison only and we assign no value to it other than that this simple procedure reproduces the actual spectra quite well. Similar to Pt(211), Pt(533) gives rise to two distinct water desorption features. However, here the high temperature peak shows a maximum desorption rate at 188 K. This is the same temperature

observed for the maximum desorption rate of (100) step-bound water on Pt(755) and Pt(977). For Pt(533), a shoulder appears at ∼170 K[16]. By comparison to the other stepped surfaces and Pt(111), this was previously associated with desorption of water bound on (111) terrace sites[29]. The onset of the multilayer desorption feature and the step peak from Pt(533), Pt(977) and Pt(755) appear at lower temperatures as compared to Pt(211) (dashed-dotted vertical lines). On the basis of these results, we suggest that there is a discontinuity in water adsorption behavior to Pt[n(111)x(100)] surfaces that appears when reducing the terrace width below n=4.

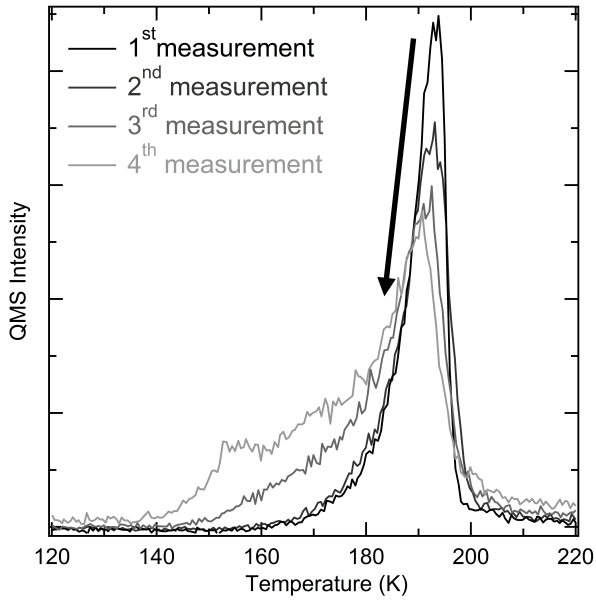

Figure 4.4: TPD spectra of nearly identical H_2O coverages desorbing from Pt(211). After each TPD measurement the sample was cooled, without heating to the temperature where oxygen starts desorbing.

We noted that the TPD data in figure 4.2 for Pt(211) suggest a crystalline nature for the first two layers (see chapter 5). The considerably higher desorption temperature for the water layer in contact with the Pt surface as compared to surfaces with wider terraces may result from an additional stabilization for water bound to the (100) step edge[29]. As the terraces are very narrow, one can imagine that step-bound water interacts not only through H-bonding along the step edge[38, 39], but also directly with water bound to neighboring steps. On the other hand, one may also consider the upward temperature shift to reflect (par-

tial) dissociation of water at step edge. Fajin et al. recently calculated binding energies for individual H_2O molecules and the OH_{ads} + H_{ads} products to Pt(211) using density function theory (DFT)[40]. Although dissociation was found to be exothermic, the activation energy was higher than the adsorption energy (0.66 eV and 0.41 eV, respectively). Hence, they concluded that dissociation was not to be expected. Although our current data is not conclusive, we have reason not to discard dissociation entirely. First, although our Pt(211) surfaces shows all LEED characteristics of a well-behaved step structure with mono-atomic high steps, kinks in these steps are very likely present. Dissociation at kinks and at steps for water clusters may well compete with desorption during the temperature ramp, as was found in DFT calculations for isolated molecules on Pt(321)[41]. Second, figure 4.4 shows small but continuous changes in TPD spectra for repeated water doses with consecutive temperature ramps when the surface is not annealed at temperatures above the associative desorption temperature of O_2 in between water doses. We observe that after each experiment, the intensity of the step peak drops. This may suggest that the first water layer indeed dissociates in part producing some H and OH groups. These products may desorb recombinatively as H_2O leaving a clean surface, but this would not explain changes in consecutive TPD spectra. On the other hand, OH groups may also recombinatively desorb as H_2O leaving O_{ads} on the surface. This may explain observed changes in consecutive experiments.

4.4.2 Deuterium

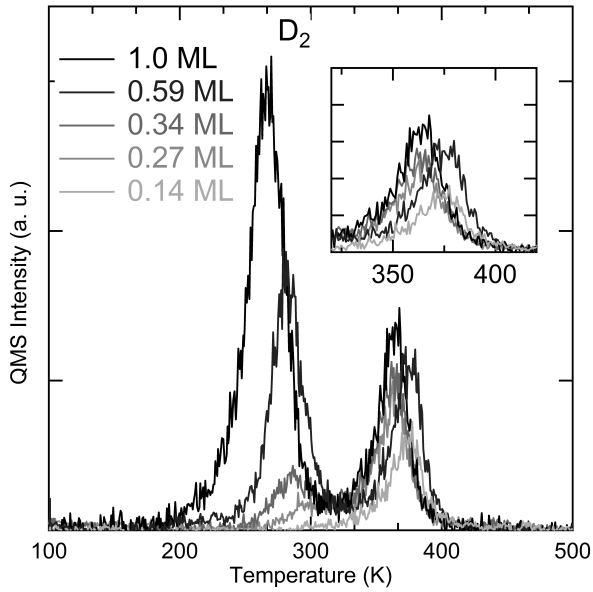

Figure 4.5: D_2 TPD spectra for Pt(211) for various initial coverages. The inset shows desorption from the (100) steps in greater detail.

In figure 4.5 we show TPD spectra for various amounts of D_2 associatively desorbing from Pt(211). For low initial coverages, a high temperature desorption peak saturates at 374 K. After saturation, a second peak appears, its maximum shifting continuously from 315 to 277 K. A comparison to previous studies suggests that the high temperature peak originates from recombinative desorption occurring at (100) step sites, while the low temperature peak results from desorption from (111) terrace sites[16, 25, 42, 43]. For desorption from terraces, trailing edges overlap mostly. This behavior characterizes second-order desorption kinetics and may be expected from associative desorption from a uniform surface with no dependence of binding energy on surface coverage. For desorption from the (100) steps, the inset of figure 4.5 shows more detail although it does not allow us to draw conclusions regarding the kinetic order of desorption.

In figure 4.6 we compare TPD spectra of the highest obtained D_{ads} coverage on Pt(533) and Pt(211), on the top and bottom panels, respectively. The two spectra consist of two peaks at saturation, both of which are reproduced rather accurately using Gaussian line shape fits. On Pt(533), the step and terrace desorption peaks saturate at 376 K and 264 K. In contrast to desorption of H_2O, for

D_2 the (100) steps of Pt(211) and Pt(533) give rise to maximum desorption rates at nearly identical temperatures, although the desorption feature for the (100) step on Pt(533) is slightly broader. This suggests that the binding energy of D_2 on the (100) steps of Pt(211) and Pt(533) are very similar. The maximum desorption rates for the (111) terraces shows larger differences. On Pt(211) it appears 11 K higher than for Pt(533) and the width of the desorption peaks broaden for the latter by more than a factor of two. These differences suggest that D atoms have, on average, a higher binding energy on the three-atom wide (111) terraces of Pt(211) than the four-atom wide (111) terraces of Pt(533) and that the wider terrace shows more variation in binding energy. These conclusions are fully in line with recent calculation for the binding energy variation of H to such surfaces. For both Pt(211)[44] and Pt(533)[45] binding energies were calculated and found to be highest for H atoms bound to the (100) step edge. When moving away from the bottom steps toward the next downward step along the terrace, the binding energy in the step edge and on three-fold hollow sites on the terrace progressively drop toward the value found for Pt(111).

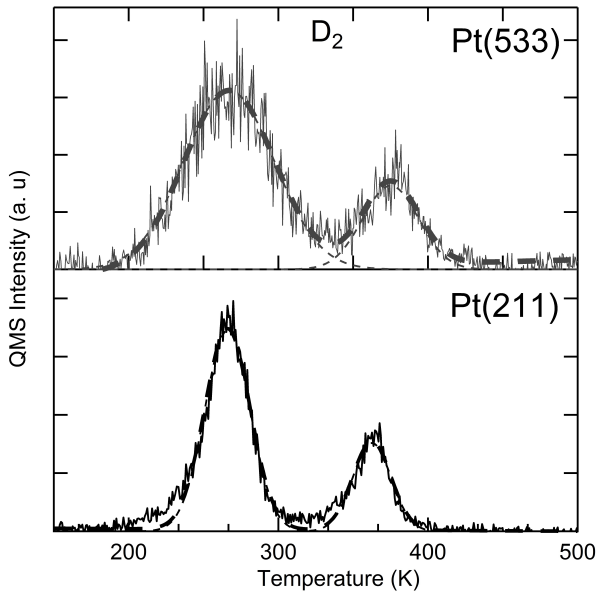

Figure 4.6: Comparison of D_2 TPD spectra for (top) Pt(533) and (bottom) (211) for maximum surface coverage.

We have also studied the effect of the terrace length on the ratio of terrace desorption to step desorption for deuterium on Pt[n(111)(100)] for $n = 3$, 4 and

6. Using fits as exemplified in figure 4.6, we find the ratio of terrace-bound D to step-bound D for n = 6, n = 4 and n = 3 to be 5.2, 3.1 and 2.7, respectively. As expected, for Pt[4(111)(100)] and Pt[6(111)(100)], the ratio of terrace-bound to step-bound D ratio is nearly proportional to *(n-1)*. For Pt[2(111)(100)] this ratio is markedly higher than what is predicted for $n = 3$. Again, we find a clear deviation from expected behavior which is also well beyond our uncertainty limits when n drops below 4.

4.4.3 Oxygen

In figure 4.7 we show TPD spectra for associative O_2 desorption from the maximum coverage created by dissociation of O_2 from background dosing for Pt(533) and Pt(211) in the top and bottom panels, respectively. The solid lines show our experimental data while the dashed lines are fits using Gaussian functions. Again, these are only used for integration purposes and do not represent physical processes. In order to compare relative sizes of TPD peaks, the fit to the high temperature peak for Pt(211) used the parameters for the width and central temperature determined for the same peak in the Pt(533) data[16]. Briefly, Pt(533) gives rise to two easily identifiable desorption peaks in the TPD spectrum between 550 and 900 K. The low temperature peak at 663 K results from associative desorption from (111) terrace sites. The desorption feature at 774 K strongly resembles high temperature desorption from other stepped Pt surfaces and is not present when using Pt(111)[46–49]. Hence, it is attributed to associative desorption from O atoms bound to (100) step sites. Comparison to theoretical calculations suggest that this is bridge-bonded oxygen at the (100) steps with every second bridge site being occupied[45, 50, 51].

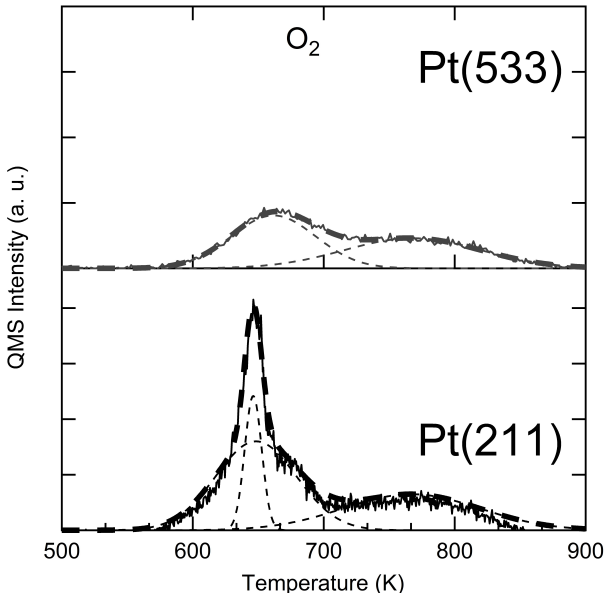

Figure 4.7: Comparison of O_2 TPD spectra for (top) Pt(533) and (bottom) (211) for maximum surface coverage. O_2 was dosed at Ts $\sim$ 100 K.

In the TPD trace for maximum coverage in bottom panel of figure 4.7, Pt(211) shows three desorption features. These are more easily identified in TPD traces appearing in figure 4.8 for varying initial coverages. There, we also separately show the regimes where O_2 desorbs from a molecularly adsorbed state between 100 and 200 K and the associative desorption occurring at much higher temperatures. At low initial coverage, a high temperature peak shows a maximum desorption rate at $\sim$780 K which strongly resembles the high temperature desorption feature for Pt(533)[16]. After saturation of the peak at highest temperature, a shoulder develops that turns into a distinct maximum at 677 K. Even higher initial doses lead to the third desorption peak that saturates with a maximum desorption rate at 646 K. This peak is considerably narrower than the former two peaks. The leading edge initiates at 570 K and shows unexpected behavior of zeroth-order desorption kinetics. The comparison between the peak shapes in figure 4.7 clearly shows that, again, there is a pronounced effect to this minor variation of terrace width from $n = 3$ to 4.

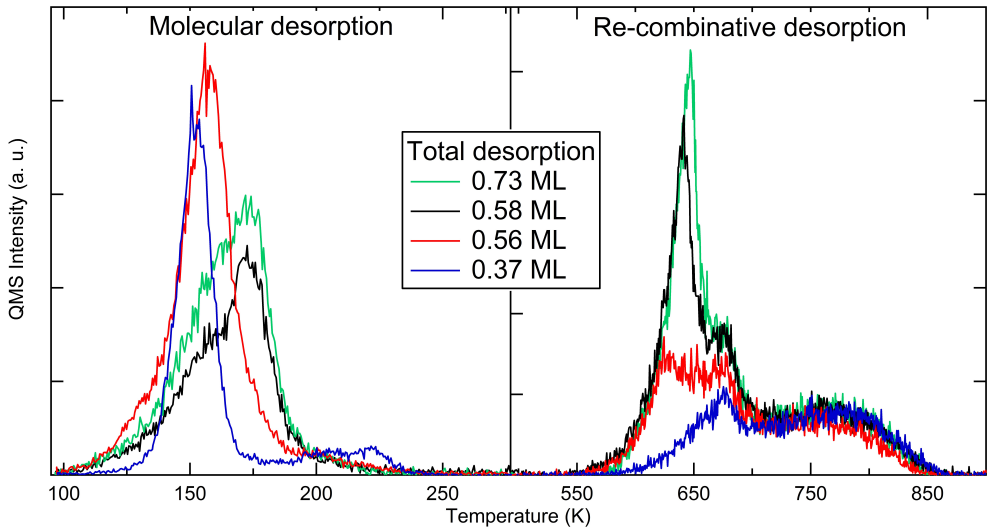

Figure 4.8: TPD spectra of varying amounts of O_2 desorbing from Pt(211). The low temperature panel (left) shows desorption of molecularly adsorbed O_2; high temperature panel (right) shows recombinative desorption of O_{ad}.

Our series of TPD spectra shown in figure 4.8 match those of a previous study on O_2 desorption from Pt(211) by Winkler et al.[52]. Although they also observed the sharp peak with overlapping leading edges and a well-defined shoulder between 650 and 700 K, they provided no suggestion for the origin of these two peaks appearing in the regime where O_2 is known to desorb from Pt(111). In a more recent study that used Pt(533) and O_2 adsorption from background dosing, the same single desorption feature in the temperature regime between 550 and 700 K was found that we report for Pt(533) in figure 4.7[16]. When using a supersonic molecular beam to dissociate O_2 on Pt(533), Gee and Hayden found a similar but considerably smaller third desorption peak in the same temperature regime. They attributed it to associative desorption of an atomic state due to the dissociation of O_2 at (100) steps[25]. Following the previous suggestions that a maximum coverage of 0.25 ML is obtained by background dosing on Pt(533) and a ratio of $O_{ads,step}$:$O_{ads,ter}$ of approximately 0.11:0.14[16, 25], we estimated the amounts of O contribution to the three desorption peaks observed for Pt(211). Here, we assume that the higher step density of Pt(211) also yields a proportionally higher total desorption from (100) steps around 750 K. We obtain a coverage of 0.15 ML for the desorption of bridge-bonded oxygen at the step and 0.29 ML for the combined lower temperature desorption. Pt(211) thus yields a maximum total O_{ads} coverage of 0.44 ML. We have analyzed the O-covered surface in detail by

LEED but find no evidence for an ordered overlayer structure.

To shed light on the origin of the more complex desorption and higher apparent O_{ads} coverage for the (211) surface, we consider other (TPD) studies that have focused on Pt oxidation and show a similar characteristic sharp feature at the lower side of the well-known recombinative desorption features. For Pt(553) (or Pt[(4(111)x(110)]), we have previously reported a similar sharp feature in desorption studies that only appeared when the surface was not properly annealed in between exposures and temperature ramps[15] . When plotting the highest obtained coverage for Pt(211) and Pt(553) in a single graph, these sharp peaks overlap nearly perfectly (not shown here). For the (332) surface (Pt[5(111)x(110)], which is very similar to Pt(533), Wang et al. have previously shown by a combined core-level spectroscopy and DFT study that an increased O-surface coverage resulted in 1-dimensional (1D) PtO_2 chains forming at these steps[53, 54]. A similar PtO_2 chain structure had also been suggested by a combined STM-DFT study for the top ridge of the reconstructed Pt(110)-(1x2) surface[55]. Note that the step edge for Pt(553), Pt(332) and this reconstructed (110) surface consist of the exact same spatial arrangement of the Pt atoms forming the edge. It is a triangular arrangement on either side of the lowest coordinated Pt atoms. On the basis of XPS, TPD, STM and DFT studies, Weaver and coworkers came to the conclusion that similar 1-D PtO_2 chains can even be produced on Pt(111) using an atomic oxygen source. The 1-D PtO_2 chains directly relate to the sharp β_1 desorption feature in their TPD spectra[56–59]. A similar TPD feature was much earlier observed for high O-coverages on Pt(111) produced from NO_2 dissociation[60] and also appears for the hexagonally reconstructed Pt(100) surface[61]. A study by Gland on Pt(111) and Pt[11(111)x(110)] did not reveal the sharp recombinative desorption feature for the stepped surface, although the additional molecular desorption feature that appears characteristic for steps was present[46, 47].

Considering these previous results, the appearance of the sharp feature in our TPD traces for Pt(211) between 600 and 650 K may be interpreted to suggest that the (100) step edge on Pt(211) is capable of producing 1D-chains of PtO_2. This is remarkable as the Pt(533) surface with the same (100) step type has no or very little tendency to do so. Only at high incident energy, the onset of this characteristic desorption feature is observed in TPD experiments following adsorption from a supersonic molecular beam[62]. Wang et al. did not find this peak using background dosing onto Pt(533)[63]. We also do not observe it for Pt(533), even after high exposures at room temperature. Hence, if this TPD peak for Pt(211) is indeed related to the formation of 1D-PtO_2 chains at higher O_2 exposures, the ease with which the feature appears in our study suggests that the barrier to O_2 dissociation leading to a coverage beyond 0.25 ML critically

depends on terrace width and changes between $n = 3$ and $n = 4$.

We scrutinize our TPD results in figure 4.8 to obtain a better view of the requirement to obtain the desorption feature that resembles desorption from 1-D PtO_2 chains. At a total desorption equivalent to 0.37 ML O (blue) we identify one major and two small features for desorption from molecular states at 153 K, 202 K and 222 K. Following the interpretation by Wintterlin et al. for Pt(111), we attribute the feature at 153 K to desorption of O_2 bound in molecular clusters to (111) terrace sites[64]. During desorption of O_2 molecules, other O_2 molecules dissociate as the barriers for these processes are similar. Desorption at slightly higher temperatures (between 200 and 250 K) may be due to O_2 adsorbed to bare (100) steps. At the initial dose leading to a total desorption of 0.37 ML, we find predominantly recombinative desorption from regular step-bound O_{ads}. These atoms may have dissociated at terrace sites and diffused to step sites during the temperature ramp, but may also have dissociated at the step. At 0.56 ML total O coverage (red), the main molecular desorption peak broadens and shifts to 157 K. In the recombinative desorption regime, the lower temperature desorption peak at 626 K has appeared. Increasing the initial dose further to 0.58 total O_{ads} coverage (black), the desorption of molecularly bound O_2 suddenly changes. The lowest desorption peak drops in intensity and a peak at 172 K dominates. In the right panel, the sharp feature with apparent zeroth-order desorption kinetics grows in rapidly. For 0.73 ML total O coverage (green), even more O_2 desorbs from molecular states, while the recombinative desorption saturates.

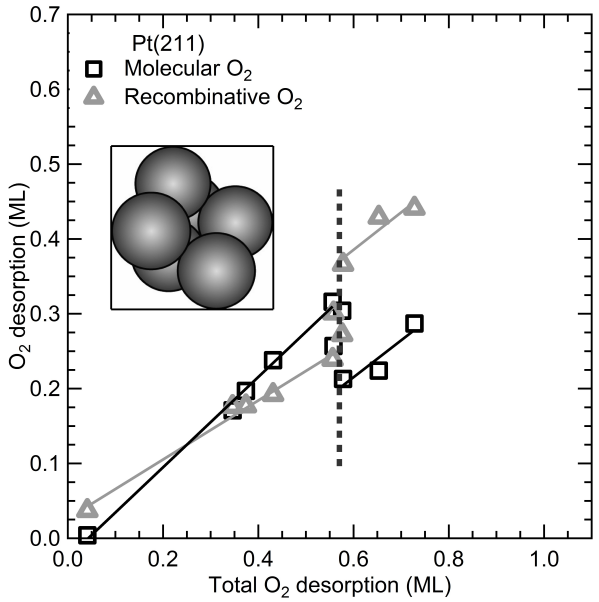

Figure 4.9: Integrated O_2 TPD signals for molecular and recombinative desorption as a function on initial O_2 coverage on Pt(211). The dotted-vertical line indicates the critical coverage near 0.56 ML.

To clarify the sudden change around a total desorption near 0.56 ML, we separately quantify in figure 4.9 the observed molecular and recombinative O_2 desorption as a function of total O_2 desorption. Both show a linear dependence before and after 0.56 ML, however the partitioning between molecular and recombinative desorption drastically changes above this coverage. From competing desorption and dissociation during the initial stages of the temperature ramp, the latter benefits from high initial O_2 coverages. For Pt(111), Miller et al. showed that attractive adsorbate-adsorbate interactions affect the dissociation of O_2[65]. In particular, they found that the desorption energy increased while the dissociation energy decreased for the molecular coverage regime of 0 - 0.25 ML O_2. This is to be compared to 0 - 0.50 ML O_{ads} coverage in our figure 4.9. Our results show that partitioning between desorption and dissociation below 0.56 ML for Pt(211) is not strongly affected by the initial coverage over this range as both components show nearly identical changes with initial coverage. If lateral interactions affect the partitioning in this regime, it actually favors desorption in contrast to what Miller et al. suggest for Pt(111). However, we observe for the stepped surface a sudden increase in the dissociation relative to desorption at ∼0.56 ML O (or 0.28 ML O_2), whereas for Pt(111) the opposite trend was predicted. There, the barrier

to dissociation increased from 0.24 eV to 0.74 eV between O_2 adsorbate structures representing a total of 0.5 and 1.0 ML O. Hence, the (100) step introduces an additional effect in providing an alternative site or pathway for dissociation with an additional lowering of the activation barrier. At 0.56 ML total initial O, a turning point is reached above which desorption from the molecular state is reduced. It leads to an upward temperature shift in the molecular desorption regime and a rapid growth of the feature that resembles the feature observed for 1-D PtO_2 chains.

If PtO_2 chains form at the step edge during the temperature ramp, it must stoichiometrically be reflected in the TPD traces. Considering the development of the three associative desorption peaks in our TPD spectra, the previously mentioned ratio of 0.15:0.29 for the single high and two combined lower temperature peaks are more likely to represent an approximate ratio of 1:1:1 for three types of O atoms desorbing from to step, terrace, and step sites. As at lower total coverages oxygen binds at the step with only one O atom per 2 Pt atoms (every second bridge site), this makes the Pt:O stoichiometry for the highest obtained coverage in our spectra 1:1 and not 1:2 for Pt_{step}:O. For an ordered overlayer forming PtO at the step and an O-atom bound to a three-fold site at the terrace, the ultimate coverage would become 0.50 ML, whereas we find a maximum of 0.44 ML. Not reaching the highest coverage is reasonable that the atomically-bound oxygen is formed from dissociation of molecularly-bound O_2 that may also desorb in a parallel process. It is also supported by the lack of long-range order for an overlayer in LEED patterns.

We finally speculate on the origin of the different tendencies to form the high coverage structure, along the step for $n = 3$ and $n = 4$. First, we recall that the (100) step type has a triangular arrangement of Pt atoms on one side and a square arrangement on the other side. For the (100) and (110) step types, other adsorption sites for O are preferred in the low coverage regime[45, 50]. For the (110) step type, oxygen atoms adsorb preferentially in the three-fold hollow on the upper terrace, whereas for the (100) step the bridge site is preferred. Molecular O_2 adsorption occurs prior to dissociation with the O-O bond parallel to the step edge[51, 66, 67]. The differences in TPD traces for stepped surfaces and the (111) plane suggest that the O_2 dissociation and desorption occurs at the terrace prior to the step ($\sim$150 K vs. 220-250 K). The difference between Pt(211) and Pt(533) in producing the additional sharp TPD features thus seems related to the initial O_2 dissociation and the exact sites where oxygen atoms adsorb on the narrow (111) plane. Apparently, for the 3-atom wide terrace with a (100) step, this occurs such that it alters subsequent dissociation/desorption at the step. It leads to more facile dissociation and to a desorption feature that we attribute to

PtO-like chains at the step.

We note that TPD results can be misleading with regards to stoichiometry and desorption sites. For example, in a previous combined theoretical and experimental study we showed that three peaks in the desorption of H_2 from Pt(110)(1x2) are not a consequence of three different desorption sites[68]. Hence to confirm the proposed stoichiometry, other techniques are needed. figure 4.10 shows two schematics of potential surface structures for ordered overlayers of atomic oxygen on Pt(533) and Pt(211) that would explain the similarity in TPD structures for O coverages well below the maximum coverage and the ratios of integrated TPD peaks. It assumes a maximum coverage of 0.25 ML for Pt(533)[62] and suggests a true maximum coverage of 0.50 ML for O/Pt(211). On Pt(533), the strongest adsorption site on the terrace is the FCC hollow[45], which is the first atomic oxygen to be created during the temperature ramp when other terrace-bound O_2 desorbs. Consecutive O_2 desorption from step sites creates space for additional dissociative adsorption at the (100) steps. The narrower terrace of Pt(211), leads to HCP-bound O instead of FCC-bound O if the step edges again are also covered by O_2. We suggest that this may drive the higher level of consecutive O_2 dissociation at the step during the temperature ramp for Pt(211) leading to a ratio of 1:1 for Pt_{step}:O.

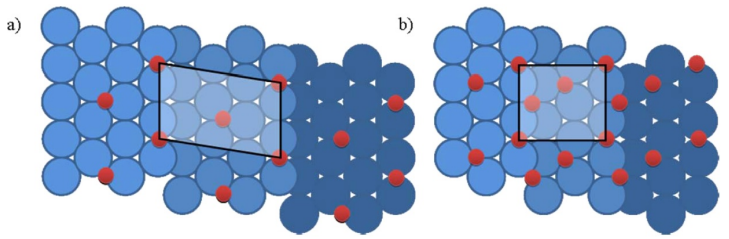

Figure 4.10: Idealized adsorbate structures for a) O/Pt(533) with a 1:1 O_{step}:$O_{terrace}$ ratio and 0.25 ML and b) O/Pt(211) representing, a 2:1 O_{step}:$O_{terrace}$ ratio and 0.50 ML.

4.5 Conclusions

In this study we have shown that surfaces having the same step type and terrace geometries may show very different behaviors even for changes in terrace width of only one atom. For D_2, recombinative desorption from the step edge seems not affected by the width of the neighboring terraces. This is in line with our previous molecular beam adsorption studies, where we found that the reactivity on Pt(211) may be used to quantitatively predict the reactivity for all other surfaces of the

same type in the zero-coverage limit[10, 69]. However, the presence of the step affects the binding energy for H atoms on the terrace mostly close to the step edge. We observe this effect in recombinative desorption. A narrow terrace only contains sites that are all affected by the step, whereas a wider terrace contains sites more strongly resembling the infinite (111) plane. Hence, the wider the terrace, the larger the variation in binding energy and the broader the desorption feature from terrace sites. For water adsorption to Pt(211), we find crystalline growth at temperatures where on Pt(533) and surfaces with even wider terrace ASW forms. Here, the surface structure steers adsorption and affects mobility of molecules such that it enhances lateral ordering of adsorbates on (211). We expect that this is a consequence of the distance between step edges where water generally tends to accumulate. The crystallinity of water and exact structure may be confirmed and further investigated experimentally by, e.g., STM and RAIRS studies, or by theory. Finally, O_2 dissociation is also affected by terrace width. We find a considerably larger O coverage on this surface resulting from enhanced dissociation of molecularly adsorbed O_2 at high initial coverage. A simple quantitative analysis of our TPD results shows that we likely form a stoichiometric ratio of 1:1 for Pt_{step}:O.

Our results thus give reason to be cautious in extrapolating results from theoretical studies on the smallest unit cell to larger structures. For H_2, the lowering of the dissociation barrier locally at the step is probably not affected by terrace length. However, the effect that the step has on binding sites near the step is strong close to the step and weakens with distance. Hence the potential influence of the step to altering diffusion, reaction and desorption at the terrace is dependent on terrace length. We observe these effects directly in our TPD experiments and see different behavior already when comparing 3 and 4 atom wide terraces. This obviously also directly relates to overall kinetics of chemical reaction as with increasing particle diameter the terrace size increases and ratio of step-to-terrace sites drops. For O_2 dissociation, we suggest that the exact location of O atoms formed at the terrace influences consecutive dissociation at the step. Here, the barrier to dissociation at the step is affected by the terrace length, but only through the location of the terrace-bound O atom. Finally, for H_2O adsorption, the delicate balance between lateral interactions and individual binding energies seems not allow for any extrapolation from studies using a single small unit cell.

4.6 Bibliography

References

(1) Reith, F; Campbell, S. G.; Ball, A. S.; Pring, A; Southam, G English *Earth-Science Reviews* **2014**, *131*, 1–21.

(2) Wang, H.; An, K.; Sapi, A.; Liu, F.; Somorjai, G. A. *Catalysis Letters* **2014**, *144*, 1930–1938.

(3) Thiel, P. A.; Madey, T. E. *Surface Science Reports* **1987**, *7*, 211–385.

(4) Ranke, W *Surface Science* **1989**, *209*, 57–76.

(5) Matsushima, T. *Surface Science* **1985**, *157*, 297–318.

(6) Rettner, C. T.; Mullins, C. B. English *Journal of Chemical Physics* **1991**, *94*, 1626–1635.

(7) Christmann, K; Ertl, G; Pignet, T *Surface Science* **1976**, *54*, 365–392.

(8) Bădescu, Ş.; Salo, P.; Ala-Nissila, T; Ying, S.-C.; Jacobi, K.; Wang, Y.; Bedürftig, K.; Ertl, G. *Physical review letters* **2002**, *88*, 136101.

(9) Luntz, A. C.; Brown, J. K.; Williams, M. D. *Journal of Chemical Physics* **1990**, *93*, 5240–5246.

(10) Groot, I. M. N.; Kleyn, A. W.; Juurlink, L. B. F. *Angewandte Chemie-International Edition* **2011**, *50*, 5174–5177.

(11) Luntz, A. C.; Grimblot, J; Fowler, D. E. *Physical Review B* **1989**, *39*, 12903–12906.

(12) Luntz, A. C.; Williams, M. D.; Bethune, D. S. *Journal of Chemical Physics* **1988**, *89*, 4381–4396.

(13) Derry, G. N.; Ross, P. N. *Surface Science* **1984**, *140*, 165–180.

(14) Hodgson, A.; Haq, S. *Surface Science Reports* **2009**, *64*, 381–451.

(15) Van der Niet, M. J. T. C.; den Dunnen, A.; Juurlink, L. B. F.; Koper, M. T. M. *Physical Chemistry Chemical Physics* **2011**, *13*, 1629–1638.

(16) Van der Niet, M. J. T. C.; den Dunnen, A.; Juurlink, L. B. F.; Koper, M. T. M. *Journal of Chemical Physics* **2010**, *132*, 174705–174713.

(17) Vanhove, M. A.; Somorjai, G. A. *Surface Science* **1980**, *92*, 489–518.

(18) Watwe, R. M.; Cortright, R. D.; Norskov, J. K.; Dumesic, J. A. *Journal of Physical Chemistry B* **2000**, *104*, 2299–2310.

(19) Greeley, J; Rossmeisl, J; Hellman, A; Norskov, J. K. English *Zeitschrift Fur Physikalische Chemie-International Journal of Research in Physical Chemistry & Chemical Physics* **2007**, *221*, 1209–1220.

(20) Peterson, A. A.; Grabow, L. C.; Brennan, T. P.; Shong, B.; Ooi, C.; Wu, D. M.; Li, C. W.; Kushwaha, A.; Medford, A. J.; Mbuga, F.; Li, L.; Norskov, J. K. *Topics in Catalysis* **2012**, *55*, 1276–1282.

(21) Janlamool, J.; Bashlakov, D.; Berg, O.; Praserthdam, P.; Jongsomjit, B.; Juurlink, L. B. F. *Molecules* **2014**, *19*, 10845–10862.

(22) Van Reijzen, M. E.; van Spronsen, M. A.; Docter, J. C.; Juurlink, L. B. F. *Surface Science* **2011**, *605*, 1726–1731.

(23) Yates Jr, J. T. *Springer, New York* **1998**, *27*, 181–0013.

(24) Den Dunnen, A.; van der Niet, M. J. T. C.; Koper, M. T. M.; Juurlink, L. B. F. *Journal of Physical Chemistry C* **2012**, *116*, 18706–18712.

(25) Gee, A. T.; Hayden, B. E.; Mormiche, C; Nunney, T. S. English *Journal of Chemical Physics* **2000**, *112*, 7660–7668.

(26) Nieskens, D.; van Bavel, A.; Niemantsverdriet, J. *Surface Science* **2003**, *546*, 159–169.

(27) Habenschaden, E; Kuppers, J *Surface Science* **1984**, *138*, 147–150.

(28) Tait, S. L.; Dohnalek, Z; Campbell, C. T.; Kay, B. D. *Journal of Chemical Physics* **2005**, *122*.

(29) Den Dunnen, A.; van der Niet, M. J. T. C.; Badan, C.; Koper, M. T. M.; Juurlink, L. B. F. *Physical Chemistry Chemical Physics* **2014**, 8530–8537.

(30) Petrik, N. G.; Kimmel, G. A. English *Journal of Chemical Physics* **2004**, *121*, 3736–3744.

(31) Speedy, R. J.; Debenedetti, P. G.; Smith, R. S.; Huang, C; Kay, B. D. *Journal of Chemical Physics* **1996**, *105*, 240–244.

(32) Dohnalek, Z; Ciolli, R. L.; Kimmel, G. A.; Stevenson, K. P.; Smith, R. S.; Kay, B. D. English *Journal of Chemical Physics* **1999**, *110*, 5489–5492.

(33) Van der Niet, M. J. T. C.; Dominicus, I.; Koper, M. T. M.; Juurlink, L. B. F. *Physical Chemistry Chemical Physics* **2008**, *10*, 7169–7179.

(34) Smith, R. S.; Matthiesen, J.; Knox, J.; Kay, B. D. *Journal of Physical Chemistry A* **2011**, *115*, 5908–5917.

(35) Kimmel, G. A.; Petrik, N. G.; Dohnalek, Z; Kay, B. D. *Physical Review Letters* **2005**, *95*, 166102–166106.

(36) Kimmel, G. A.; Petrik, N. G.; Dohnalek, Z.; Kay, B. D. *Journal of Chemical Physics* **2006**, *125*, 44713–44725.

(37) Kimmel, G. A.; Petrik, N. G.; Dohnalek, Z.; Kay, B. D. *Journal of Chemical Physics* **2007**, *126*, 114702–114712.

(38) Endo, O.; Nakamura, M.; Sumii, R.; Amemiya, K. *Journal of Physical Chemistry C* **2012**, *116*, 13980–13984.

(39) Nakamura, M.; Sato, N.; Hoshi, N.; Soon, J. M.; Sakata, O. *Journal of Physical Chemistry C* **2009**, *113*, 4538–4542.

(40) Fajín, J. L. C.; D. S. Cordeiro, M. N.; Gomes, J. R. B. *The Journal of Physical Chemistry A* **2014**, *118*, 5832–5840.

(41) Donadio, D.; Ghiringhelli, L. M.; Delle Site, L. *Journal of the American Chemical Society* **2012**, *134*, 19217–19222.

(42) Collins, D. M.; Spicer, W. E. *Surface Science* **1977**, *69*, 85–113.

(43) Lu, K. E.; Rye, R. R. *Surface Science* **1974**, *45*, 677–695.

(44) Olsen, R. A.; Kroes, G. J.; Baerends, E. J. *Journal of Chemical Physics* **1999**, *111*, 11155–11163.

(45) Kolb, M. J.; Calle-Vallejo, F.; Juurlink, L. B. F.; Koper, M. T. M. *The Journal of chemical physics* **2014**, *140*, 134708.

(46) Gland, J. L.; Sexton, B. A.; Fisher, G. B. *Surface Science* **1980**, *95*, 587–602.

(47) Gland, J. L.; Sexton, B. A.; Fisher, G. B. *Surface Science* **1980**, *95*, 587–602.

(48) Steininger, H; Lehwald, S; Ibach, H *Surface Science* **1982**, *123*, 1–17.

(49) Avery, N. R. *Chemical Physics Letters* **1983**, *96*, 371–373.

(50) Gambardella, P; Sljivancanin, Z; Hammer, B; Blanc, M; Kuhnke, K; Kern, K *Physical Review Letters* **2001**, *87*.

(51) Šljivančanin, Z.; Hammer, B. *Surface Science* **2002**, *515*, 235–244.

(52) Winkler, A.; Guo, X.; Siddiqui, H. R.; Hagans, P.; Yates, J. T. *Surface Science* **1988**, *201*, 419–443.

(53) Wang, J. G.; Li, W. X.; Borg, M.; Gustafson, J.; Mikkelsen, a.; Pedersen, T. M.; Lundgren, E.; Weissenrieder, J.; Klikovits, J.; Schmid, M.; Hammer, B.; Andersen, J. N. *Physical Review Letters* **2005**, *95*, 1–4.

(54) Ogawa, T.; Kuwabara, A.; Fisher, C. A. J.; Moriwake, H.; Miwa, T. *Journal of Physical Chemistry C* **2013**, *117*, 9772–9778.

(55) Helveg, S; Lorensen, H. T.; Horch, S; Laegsgaard, E; Stensgaard, I; Jacobsen, K. W.; Norskow, J. K.; Besenbacher, F *Surface Science* **1999**, *430*, 533–539.

(56) Hawkins, J. M.; Weaver, J. F.; Asthagiri, A. *Physical Review B* **2009**, *79*, 125434.

(57) Devarajan, S. P.; Hinojosa Jr., J. A.; Weaver, J. F. *Surface Science* **2008**, *602*, 3116–3124.

(58) Weaver, J. F.; Chen, J. J.; Gerrard, A. L. *Surface Science* **2005**, *592*, 83–103.

(59) Weaver, J. F.; Kan, H. H.; Shumbera, R. B. *Journal of Physics-Condensed Matter* **2008**, *20*.

(60) Parker, D. H.; Bartram, M. E.; Koel, B. E. *Surface Science* **1989**, *217*, 489–510.

(61) Shumbera, R. B.; Kan, H. H.; Weaver, J. F. English *Surface Science* **2007**, *601*, 4809–4816.

(62) Gee, A. T.; Hayden, B. E. *The Journal of Chemical Physics* **2000**, *113*, 10333–10343.

(63) Wang, H; Tobin, R. G.; Lambert, D. K.; DiMaggio, C. L.; Fisher, G. B. *Surface Science* **1997**, *372*, 267–278.

(64) Wintterlin, J; Schuster, R; Ertl, G English *Physical Review Letters* **1996**, *77*, 123–126.

(65) Miller, D. J.; Oberg, H; Naslund, L. A.; Anniyev, T; Ogasawara, H; Pettersson, L. G. M.; Nilsson, A English *Journal of Chemical Physics* **2010**, *133*, 224701–224707.

(66) Sano, M; Ohno, Y; Yamanaka, T; Matsushima, T; Quinay, E.; Jacobi, K *The Journal of chemical physics* **1998**, *108*, 10231–10238.

(67) Yamanaka, T; Matsushima, T; Tanaka, S; Kamada, M English *Surface Science* **1996**, *349*, 119–128.

(68) Gudmundsdottir, S.; Skulason, E.; Weststrate, K.-J.; Juurlink, L.; Jonsson, H. *Physical Chemistry Chemical Physics* **2013**, *15*, 6323–6332.

(69) Groot, I. M. N.; Kleyn, A. W.; Juurlink, L. B. F. *Journal of Physical Chemistry C* **2013**, *117*, 9266–9274.

Chapter 5

Surface Structure Dependence in Desorption and Crystallization of Thin Interfacial Water Films on Pt

5.1 Abstract

In this work we study the influence of substrate structure on desorption and crystallization of water deposited at 100 K on Pt. We use ultrathin water films adsorbed to well-defined, but highly corrugated Pt(211) and Pt(221) surfaces. Desorption spectra reveal variations in the wetting and subsequent layers that critically depend on step type. Crystallization is induced at much lower substrate temperatures as compared to Pt(111). The CI-like layer is also significantly more stable on stepped surfaces as evidenced by a higher desorption energy. Crystallinity of the CI-like layers is maintained over a thickness that varies strongly with step type.

Based on: Badan, C.; Heyrich, Y.; Koper, M. T. M.; Juurlink, L. B. F., J. Phys. Chem. Lett., 2016, 1682-1685

5.2 Introduction

Adsorption of water onto surfaces has been studied in great detail and reviewed several times over the past decades[1–3]. On cold (< 120 K) surfaces, it forms metastable amorphous solid water (ASW)[4–7]. ASW is considered relevant to chemical, biological, physical, astrophysical and material sciences [8–14]. ASW undergoes a phase transformation into crystalline ice (CI) upon heating. This transformation can be detected by temperature programmed desorption (TPD) as a TPD spectrum shows a deflection[4, 15] when the desorption rate drops due to the lower vapor pressure of CI[16].

Water in contact with platinum is often studied in relation to electrochemistry. Pt has good catalytic properties for many electrochemical reactions[17]. It has also become a general model system for the water-metal interface as the interaction amongst water molecules is delicately balanced by the interaction with the substrate [1]. For studies of ASW, CI and the kinetics of the phase transition, the atomically flat Pt(111) plane has often been used[6, 15, 18]. The role of surface corrugation has received more attention only recently. Water molecules tend to gather at steps on Pt(111) surfaces[19]. Steps also enhance ASW crystallization [20], control the formation of ice I_h and I_c[13], and influence long-range interaction in water films[21].

In this paper, we present results comparing ultrathin water layer desorption and crystallization from two stepped platinum surfaces with extremely narrow (111) terraces. These terraces are too narrow to support the preferred hexagonal base unit of CI without interference of the steps. Using such Pt samples, we not only incorporate edges between planes at densities similar to those on actual nanoparticles, we also test whether one may tune properties of interfacial ice through substrate structure. We compare results of TPD measurements for surfaces with different step types but similar step densities and use Pt(111) as our reference.

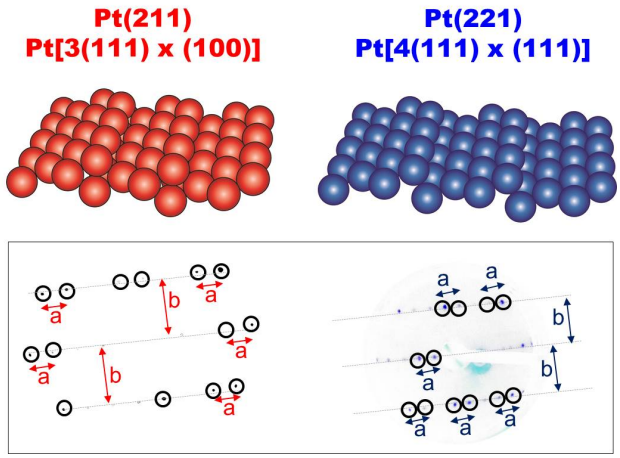

Figure 5.1: Schematic representations and inverted LEED patterns of clean Pt(211) (red) and Pt(221) (blue) on the left and right panels, respectively.

5.3 Experimental Section

Experiments were performed using a home-built (UHV) system with a base pressure of 5×10^{-11} mbar. The system and our standard procedures are discussed in detail elsewhere [22]. Briefly, a quadrupole mass spectrometer (QMS, Baltzers QMA 400) is placed in a differentially pumped canister that connects to the main UHV chamber via a 5 mm diameter circular orifice. The apparatus also contains LEED optics (VG RVL 900), a sputter gun (Prevac IS40C-PS) and three directional dosers. During water (Milipore, 18.2 Ω) deposition, the sample is positioned in front of the capillary array doser with an aperture area that ensures a homogeneous flow over the cleaned sample. Our samples are Pt single crystals (Surface Preparation Laboratory, Zaandam, the Netherlands) of 10 mm diameter and 1 mm thick, with a purity better than 5N and an orientation alignment better than 0.1°). They are positioned 2 mm from the QMS canister's orifice for TPD measurements. Samples are heated radiatively by a filament (Osram, 250 W) positioned behind the crystal or by electron bombardment. Samples are cooled by their connection to a liquid nitrogen reservoir. For all samples, experiments are performed in the same UHV chamber with the same thermocouple connections and the same measurement conditions. We have performed LEED studies on all surfaces. The bare surfaces show the expected diffraction patterns. For the stepped surfaces, we find no evidence for long-range order in the adsorbate

after water adsorption, in line with poor ordering recently observed for H_2O on Pt(553)[23].

5.4 Results and discussion

The top panel of figure 5.1 shows schematic representations of Pt(211)[22] and Pt(221). They are described as consisting of 3 atom wide (111) terraces with (100) steps, and 4 atom wide (111) terraces with (111) steps. The latter description is identical to a 3 atom wide terrace with a (110) step. The bottom panel shows color-inverted photographs of LEED patterns observed for the clean surfaces. From these images we extract spot row spacing (b) to spot splitting (a) ratios of 2.38 for Pt(211) and 3.06 for Pt(221). These values correspond well to literature values of 2.45 and 3.00 [24]. It indicates long-range order with the expected average terrace width for both surfaces.

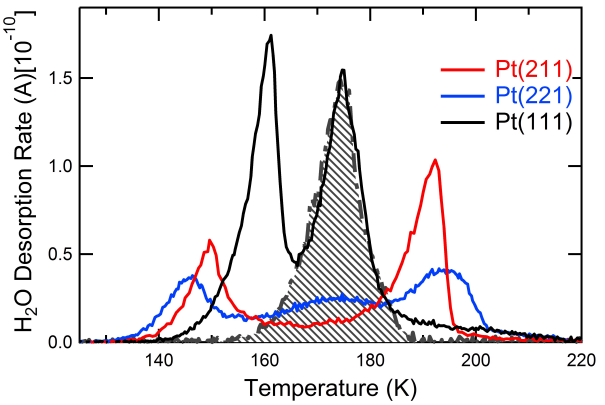

Figure 5.2: TPD spectra of water desorbing from Pt(111), Pt(211) and Pt(221). For TPD experiments the heating rate is 0.91 K s^{-1} over the temperature range shown here.

Figure 5.2 shows TPD spectra of 1 - 2 ML water desorbing from Pt(111), Pt(211), and Pt(221). Desorption between $\sim$ 140 and 165 K results from water adsorbed onto the wetting layer, which is in direct contact with the metal. This 'multilayer' desorption will be discussed below in detail. The crossed area in figure 5.2 corresponds to our best estimate for the complete H_2O wetting layer on Pt(111) and serves as our reference. We refer to it is as 1 $ML^{(111)}$. The small tail in its TPD spectrum at $>$ 190 K is a signature of surface imperfections, such as steps and kinks[25, 26], but may also result in part from a long vacuum time

constant for H_2O. We ignore it in our calibration. Based on various fittings and integrations of the peaks in the Pt(111) spectrum, we estimate our reference to be accurately determined to within $\sim 7\%$. This reference is subsequently used to determine relative coverages in desorption experiments from the other Pt surfaces.

Similar to stepped Pt surfaces with broader terraces [25, 27], Pt(211) and Pt(221) exhibit a clear desorption feature at ~ 194 K. It is attributed to desorption of water molecules adsorbed at step sites [25, 28]. However, the size of this peak varies significantly. As compared to Pt(211), the smaller size of this peak for Pt(221) is balanced by a distinct desorption feature at ~ 174 K, which is characteristic of water desorbing from Pt(111) terraces. This latter peak is also observed on Pt(553)[23, 27], which has the same (111) step type, but a 1-atom wider terrace. The separate appearance of two desorption peaks for these surfaces suggests that water bound to the (111) step and water adsorbed on the (111) terrace are poorly coupled. It may reflect the stable, square arrangement of water molecules in two parallel strands decorating the upper and lower edge of the (111) step[23]. This structure does not provide a good anchor for stable hexagonally-arranged structures on the Pt(111) terrace.

In contrary to Pt(221), Pt(211) does not give rise to a clear desorption peak around 174 K. However, a series of (100)-stepped Pt surfaces up to 8-atom wide terraces[21] do exhibit a distinct peak here, although it is poorly developed for Pt(533)[22]. The absence on Pt(211) thus seems related to the extreme narrow terrace width of Pt(211). Endo et al. and Nakamura et al. have proposed that H_2O_{ad} initially forms a 1-dimensional zig-zag line along the top edge of (100) step sites for Pt(211)[29, 30]. For higher coverages and a 1-atom wider terrace, density functional theory (DFT) calculations show multiple stable structures with nearly identical energies, all containing linear double-stranded water decorating the (100) step edge[31]. Our TPD spectra thus suggest that, contrary to Pt(221), the Pt(211) surface contains no true (111)-terrace-bound water, likely for a lack of space.

The desorption feature appearing at the lowest temperature in figure 5.2 indicates the presence of second or additional water layers [22, 26, 27, 32]. Our direct comparison of the three surfaces using a single UHV apparatus with identical temperature measurement allow us to observe a clear difference in the onset of this "multilayer" desorption feature. The lateral shift signals that the underlying wetting layer and, thus, the metal surface structure tune the desorption of additional water layers. To determine how far the influence of the surface structure reaches into an adsorbed water multilayer, we investigated the desorption of ultrathin layers up to 10 ML^{111} average thickness.

Figure 5.3 displays TPD spectra for Pt(211) and Pt(221) in the top and bot-

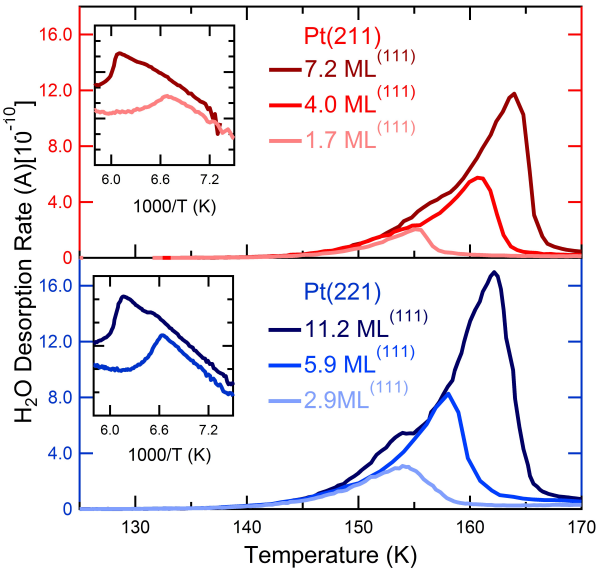

Figure 5.3: TPD spectra of water desorbing from clean Pt(211) (red) and Pt(221) (blue), on the top and bottom panels, respectively. Note that only multilayer desorption features are shown. The inset figures exhibit the Arrhenius plots from the TPD data.

tom panels, respectively. For clarity, we only present the multilayer desorption regime ($<$ 170 K). A typical multilayer desorption spectrum exhibits an exponential increase in desorption rate as a function of temperature with zero-order desorption kinetics [4, 6, 22, 27]. The leading edges for Pt(211) and Pt(221) in figure 5.3 also display a deflection at $\sim$ 156 K and 152 K, respectively, for the largest coverages shown here. After the deflection, the desorption rates align with the traces for lower coverages. This deflection has been well-studied for thick layers of water grown on Pt(111) and other surfaces and indicates crystallization of ASW to CI. [4–6, 25, 32, 33].

The insets in figure 5.3 show typical Arrhenius plots obtained from the same set of TPD spectra. Applying the Arrhenius rate equation, desorption rate = $\nu_0 \times \exp(-E_{des}/RT)$, we extract activation energies (E_{des}) from the slopes of the traces. These activation energies are interpreted as desorption energies. We do this separately for the temperature regimes where the TPD spectra suggest that we observe desorption from two distinct water phases, i.e. prior to and beyond the inflection[5]. We repeat this for various water films grown in the 1-10 ML$^{(111)}$ range. The same analysis also yields frequency factors.

The obtained desorption energies are displayed in figure 5.4 as a function of the (average) water layer thicknesses expressed in terms of our 1 $ML^{(111)}$ reference. The solid lines passing through our data only guide the eye, although the horizontal parts are based on local averages of the data. The horizontal dotted lines are the reported values for E_{des} of ASW and CI grown on Pt(111) [5, 6]. The drop in desorption energy over a narrow range of layer thickness and the rather similar values in comparison the CI and ASW at low and high coverage respectively, strongly suggests that we indeed have two different phases of water desorbing from our samples. As we do not have other means to determine the structure, we refer to them as ASW and crystalline ice-like (CI-like) water.

Comparing the values for E_{des} found for the thicker layers, we find that both stepped surfaces yield values ca. 1 kJ mol^{-1} lower than reported values for ASW. The minor difference is likely a result of the very limited temperature regime over which we need to fit our data as a consequence of using ultrathin films. At the same time, for the thinnest multilayers our values exceed the value reported for CI [5, 6, 34]. We obtain 57.9 and 56.7 kJ mol^{-1} for Pt(211) and Pt(221), respectively, which is to be compared to 55.9 kJ mol^{-1} for Pt(111) [5]. Again, our values may be influenced by limitations resulting from the low film thickness. Nevertheless, the clear difference between the obtained results even for the same layer thickness suggests that our very thin CI-like layers are not quite the same as bulk CI. In addition, the layer thickness required to start observing desorption from an ASW phase differs by a factor of two between the two surfaces. The CI-like phase is ~ 6 monolayers thick on Pt(221) and only ~ 3 ML on Pt(211). Finally, recognizing that variations between different laboratories occur in establishing desorption energies, we note that the absolute difference between CI-like and ASW layers for our stepped surfaces is significantly larger than that for Pt(111). Hence, if the desorption energy of ASW for our stepped surfaces is off and should align with the indicated value for Pt(111), then the CI-like layers on our stepped surfaces are stabilized even more as compared to Pt(111). Obviously, this only holds if the ASW in our ultrathin layers is structurally the same as thick ASW layers.

Crystallization of ASW depends, amongst other variables, on film thickness and desorption rate[7]. For thicker films and low evaporation rates, it occurs at the interface with the vacuum [7, 32, 35]. For ultrathin films, such as those used in this study, it may be expected to occur at the interface with the substrate [7, 15]. If in our experiment ASW is formed upon deposition of water at 100 K, then the surface structure here clearly influences the crystallization rate. On Pt(221) the rate is considerably higher than on Pt(211). On the former, a thicker initial ASW layer is required for ASW to survive while progressing through the temperature

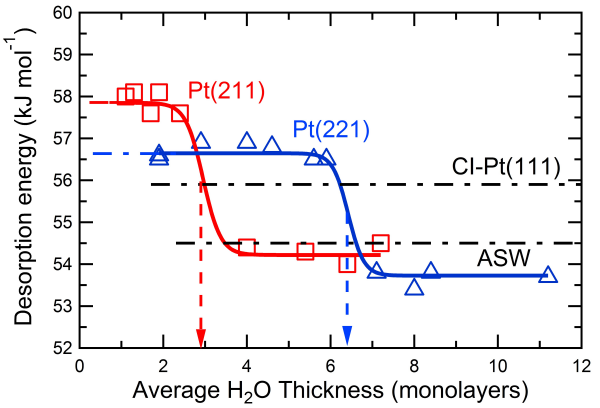

Figure 5.4: Energies for desorption at different water coverages on clean Pt(211) (red squares) and Pt(221) (blue triangles) [22]. The dash-dotted lines are the literature values for the average desorption energies for CI and ASW on Pt(111)[5, 6, 34]. The solid lines fitted through the data are only a guide for the eye.

ramp and exhibiting its specific desorption characteristics in TPD spectra. Higher crystallization rates may reflect more inhomogeneity in the film[4, 15].

On the other hand, the high level of corrugation of the Pt surfaces is not expected to provide sites large enough for CI nuclei to form. The critical radius for nucleation is estimated to be 0.6 +/- 0.4 nm [7]. Backus et al. used a Pt(533) surface to shut down potential crystallization at the interface when studying crystallization of thicker layers[32]. That surface has wider terraces than the surface used here. If crystallization is not induced by the temperature ramp, the CI-like desorption for the first layers on both surfaces indicates that water forms a crystalline structure upon deposition at 100 K. Crystallinity is maintained over various layer thicknesses depending on the details of the structure of the wetting layer and ASW grows on top of the thin CI-like layer. This stacked two-phase model may appear at odds with previous observations of crystalline growth of water deposited at 100 K on CI [15], but the CI-like layers on our nano-structured surfaces are likely not of an ice I type as both clearly show higher desorption energies.

5.5 Conclusions

Concluding, we find significant differences in thermal desorption characteristics for ultrathin water films grown on two similarly stepped Pt(111) surfaces. Differences in comparison to the extended (111) plane are even larger. The step type clearly

affects the structure of interfacial water both in the monolayer and thin film regime. We find CI-like phases at the interface which have a significantly higher desorption energy than bulk CI. We suggest that crystalline adsorption induced by the high level of corrugation at 100 K explains why crystallinity is maintained over different distances into the bulk and depends on details of the type of corrugation. However, we can not exclude that crystallization occurs at the interface during the temperature ramp. In that case, the differences in desorption rate still reflect variations in ASW structure in the layers nearest the surface.

5.6 Bibliography

References

(1) Hodgson, A.; Haq, S. *Surface Science Reports* **2009**, *64*, 381–451.

(2) Henderson, M. A. *Surface Science Rep.* **2002**, *46*, 1–308.

(3) Thiel, P. A.; Madey, T. E. *Surface Science Reports* **1987**, *7*, 211–385.

(4) Smith, R. S.; Huang, C; Wong, E. K. L.; Kay, B. D. *Surface Science* **1996**, *367*, L13–L18.

(5) Smith, R. S.; Matthiesen, J.; Knox, J.; Kay, B. D. *Journal of Physical Chemistry A* **2011**, *115*, 5908–5917.

(6) Löfgren, P.; Ahlström, P.; Lausma, J.; Kasemo, B.; Chakarov, D. *Langmuir* **2003**, *19*, 265–274.

(7) Ahlstrom, P.; Lofgren, P.; Lausma, J.; Kasemo, B.; Chakarov, D. *Physical Chemistry Chemical Physics* **2004**, *6*, 1890–1898.

(8) Ghormley, J. A.; Hochanadel, C. J. *Science* **1971**, *171*, 62–64.

(9) Fecht, H. J. *Nature* **1992**, *356*, 133–135.

(10) Stevenson, K. P.; Kimmel, G. A.; Dohnalek, Z; Smith, R. S.; Kay, B. D. *Science* **1999**, *283*, 1505–1507.

(11) Auslaender, O. M.; Yacoby, A; de Picciotto, R; Baldwin, K. W.; Pfeiffer, L. N.; West, K. W. *Science* **2002**, *295*, 825–828.

(12) Levinger, N. E. *Science* **2002**, *298*, 1722–1723.

(13) Thürmer, K.; Nie, S. *Proceedings of the National Academy of Sciences of the United States of America* **2013**, *110*, 11757–11762.

(14) Svishchev, I. M.; Kusalik, P. G. *Journal of the American Chemical Society* **1996**, *118*, 649–654.

(15) Löfgren, P; Ahlström, P; Chakarov, D. *Surface Science* **1996**, *367*, L19–L25.

(16) Kouchi, A. *Nature* **1987**, *330*, 550–552.

(17) Koper, M. T. M. *Nanoscale* **2011**, *3*, 2054–2073.

(18) Haq, S.; Harnett, J.; Hodgson, A. *Surface Science* **2002**, *505*, 171–182.

(19) Morgenstern, M; Michely, T; Comsa, G *Physical Review Letters* **1996**, *77*, 703–706.

(20) Picolin, A.; Busse, C.; Redinger, A.; Morgenstern, M.; Michely, T. *The Journal of Physical Chemistry C* **2009**, *113*, 691–697.

(21) Den Dunnen, A.; van der Niet, M. J. T. C.; Badan, C.; Koper, M. T. M.; Juurlink, L. B. F. *Physical Chemistry Chemical Physics* **2014**, 8530–8537.

(22) Badan, C.; Koper, M. T. M.; Juurlink, L. B. F. *The Journal of Physical Chemistry C* **2015**, *119*, 13551–13560.

(23) Kolb, M. J.; Farber, R. G.; Derouin, J.; Badan, C.; Calle-Vallejo, F.; Juurlink, L. B. F.; Killelea, D. R.; Koper, M. T. M. *Physical Review Letters* **2016**, *116*, 136101.

(24) Vanhove, M. A.; Somorjai, G. A. *Surface Science* **1980**, *92*, 489–518.

(25) Grecea, M. L.; Backus, E. H. G.; Riedmuller, B; Eichler, A; Kleyn, A. W.; Bonn, M *Journal of Physical Chemistry B* **2004**, *108*, 12575–12582.

(26) Gee, A. T.; Hayden, B. E.; Mormiche, C; Nunney, T. S. English *Journal of Chemical Physics* **2000**, *112*, 7660–7668.

(27) Van der Niet, M. J. T. C.; den Dunnen, A.; Juurlink, L. B. F.; Koper, M. T. M. *Journal of Chemical Physics* **2010**, *132*, 174705–174713.

(28) Skelton, D. C.; Tobin, R. G.; Fisher, G. B.; Lambert, D. K.; DiMaggio, C. L. *Journal of Physical Chemistry B* **2000**, *104*, 548–553.

(29) Endo, O.; Nakamura, M.; Sumii, R.; Amemiya, K. *Journal of Physical Chemistry C* **2012**, *116*, 13980–13984.

(30) Nakamura, M.; Sato, N.; Hoshi, N.; Soon, J. M.; Sakata, O. *Journal of Physical Chemistry C* **2009**, *113*, 4538–4542.

(31) Kolb, M. J.; Wermink, J.; Calle-Vallejo, F.; Juurlink, L. B. F.; Koper, M. T. M. *Physical Chemistry Chemical Physics* **2015**, DOI: 10.1039/C5CP04468E.

(32) Backus, E. H. G.; Grecea, M. L.; Kleyn, A. W.; Bonn, M. *Physical Review Letters* **2004**, *92*, 236101–236104.

(33) Kimmel, G. A.; Petrik, N. G.; Dohnalek, Z.; Kay, B. D. *Journal of Chemical Physics* **2007**, *126*, 114702–114712.

(34) Kimmel, G. A.; Ciolli, R. L.; Stevenson, K. P.; Smith, R. S.; Dohnálek, Z. *Journal of Chemical Physics* **2000**, *112*, 5932–5941.

(35) Wu, Y. C.; Kallis, A.; Jiang, J.; Coleman, P. G. *Physical Review Letters* **2010**, *105*, 066103–066106.

Chapter 6

The Interaction Between Water and Sub- and Pre-adsorbed Deuterium on Pt(211)

6.1 Abstract

We have studied the effects of pre- and post-dosing of deuterium on water desorption from (Pt[n(111)x(100)], n = 3), Pt(211), by temperature programmed desorption (TPD) experiments. Similar to other (100)-stepped Pt(111) surfaces with 4, 6, and 8 atom-wide terraces, Pt(211) with its 3 atom-wide terrace shows a maximum H-D exchange leading to HD and HDO formation at $\theta_{H_2O} < 0.5$ ML. The Pt(211) surface also becomes hydrophobic upon presaturating the surface with deuterium. A kinetic analysis of TPD spectra for a range of ultrathin water layer thicknesses shows that preadsorbed deuterium induces crystallinity over a larger range as compared to the bare Pt(211) surface. We explain this in terms of smoothening of the corrugation experienced by the first water layer. Similar studies using post-dosing of D_2 on adsorbed water layers does not seem to alter the H_2O structure as there is no detectable influence on the desorption energetics. Finally, we show that inherent (110)

kink defects in the (100)-type steps on this surface can be quantified by pre-deuterating the surface prior to water desorption. Their signature is especially useful when attempting to judge the surface quality without access to scanning probe techniques with (near) atomic resolution.

Based on: Badan, C.; Koper, M. T. M.; Juurlink, L. B. F., in preparation

6.2 Introduction

Water interfaces have become increasingly important for many areas of science particularly in electrochemistry[1, 2], astrophysics[3–5], chemistry[6, 7], biology[8] and physics[9, 10]. To reveal the underlying origins of the H_2O-metal interaction, adsorption of water onto metallic surfaces has been reviewed extensively over the past decades[11–13]. These studies highlight that the interfacial water structure depends, amongst other variables, on the adsorption temperature[14], substrate structure[15, 16], deposition technique[5], and the co-adsorbate[17, 18].

Platinum is considered a very good catalyst for several electrochemical reactions where interaction of water with the catalytic surface is relevant[19]. Prototypical surface science studies often use Pt(111) as a model to understand chemical and physical processes, such as adsorption, desorption, diffusion, occurring at the water-metal interface. Real catalytic surfaces, however, have a complex geometry with various types of defects such as kinks and steps. Because these defect sites increase the total reactivity of the surface especially for molecularly adsorbed species, the role of the steps and kinks in relation to water adsorption have gained more attention recently[16, 20–24]. Essentially, single atomic steps at surfaces control the formation of cubic ice (I_c) and hexagonal ice[7] (I_h) and enhance crystallinity[15, 16]. They affect long-range interaction in H_2O films and play a crucial role in wetting behaviour of the stepped Pt surfaces[23]. Although water preferentially adsorbs at the upper side of step edges[25], different H_2O structures, depending on the surface type, exist. For instance, water on Pt(553) wets the (110) step edges forming tetragons[21], whereas Pt(211) exhibits a zig-zag structure along its (100) step sites[26, 27].

Co-adsorption of water with hydrogen is particularly important in elucidating the chemistry taking place at the anode of low temperature fuel cells and the reversible hydrogen electrode[12, 13, 28]. Furthermore, the gas-surface interaction of H_2 with H_2O is critical in astrophysical environments because the physical and chemical properties of water play a crucial role in chemical and dynamical growth of the interstellar medium[17, 18]. Although numerous studies of water-metal interaction with various Pt model surfaces have been undertaken for decades, the co-adsorption of water and hydrogen on metallic surfaces has not received much attention.

In this study, we expand our knowledge of water-metal and gas-surface interactions using a highly stepped Pt surface with a very narrow (111) terrace, which has defect densities similar to actual nanoparticles. With high quality TPD measurements in combination with isotopic labeling, we study the effects of post-and-pre-deuteration on water desorption. Our results show the critical impact of the sequence of the D_2 exposure on the desorption energetics of water

and on the isotopic partitioning.

6.3 Experimental Section

Our equipment and the detailed procedures used for angle-resolved TPD experiments are discussed in detail elsewhere [15, 29]. Briefly, we performed our experiments using a home-built (UHV) system with a base pressure of 5×10^{-11} mbar. The chamber equips, amongst others, a differentially pumped quadrupole mass spectrometer (QMS, Baltzers QMA 400), a sputter gun (Prevac IS40C-PS), and LEED optics (VG RVL 900). Our samples are Pt single crystals prepared by Surface Preparation Laboratory, Zaandam, The Netherlands. They are 10 mm in diameter and 1-2 mm thick and have a purity better than 5N and an orientation better than 0.1^o. The polished side of the samples are cleaned under UHV conditions by repetitive sputtering and annealing cycles. During water (Milipore, 18.2 Ω) deposition, the sample is located at a fixed distance from the capillary array doser at T < 100 K. For the $H_2O/D_2/Pt(211)$ experiments, the cleaned surface is first exposed to D_2 by background dosing until the saturation coverage is reached. To lower the contamination by H or other residual gases, we start dosing at 700 K. For the $D_2/H_2O/Pt(211)$ experiments, first various amounts of water are dosed on the bare surface. Next, the surface is exposed to more than 250 Langmuir D_2 at < 100 K. For the TPD experiments, the heating rate was 0.92 Ks^{-1}. All our experiments are performed in the same UHV system with the same measurement conditions. We have also performed LEED experiments on Pt(211)[29]. The clean surface exhibits the expected diffraction pattern.

6.4 Results and discussion

Figure 6.1 displays H_2O TPD spectra from fully (1 ML) D_2 pre-covered Pt(211) at 0.9 Ks^{-1}. The dotted curve is 7.5 ML water desorbing from clean Pt(211). The inset figure shows more detailed spectra between 145 K - 165 K. The schematic shows three separate water layers, as indicated in orange, green and blue (same color-coding with the TPD spectra). Our previous studies[15, 29] showed that water cannot form hexagonal structures on bare Pt(211), (Pt[n(111)x(100)], n = 3) due to too narrow terrace sites. However, it can still build a 2D hydrogen-bonded network when adsorbed on Pt(211)[22, 26, 27]. When water desorbs from the bare Pt(211), TPD exhibits two peaks centered around 194 and 165 K. (dotted spectrum). The high and low temperature peaks are associated with the desorption from the (100) step sites and desorption from the second or subsequent water layers, respectively[30, 31].

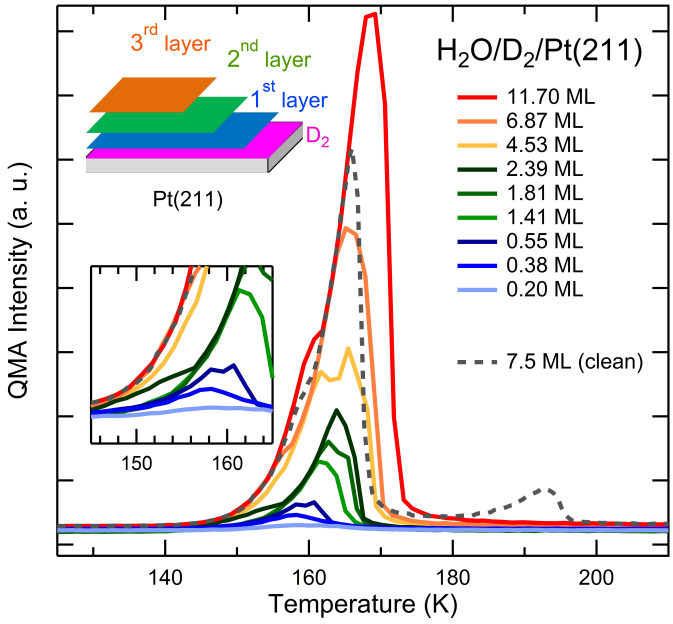

Figure 6.1: Water desorption from 1 ML D_2 pre-dosed Pt(211). The dotted curve shows water desorption from bare Pt(211). The inset figure shows the detailed spectra between 145 K and 165 K. The inset schematic illustrates the layer-by-layer growth of H_2O on the hydrogenated surface.

Water desorption from a fully hydrogenated Pt(211) appears in a broad, single desorption peak centered around 165 K, the same temperature as the water multilayer peak from the bare surface (dotted spectrum). We have previously shown that similar (100) stepped Pt(111) surfaces, (Pt[n(111)x(100)], n = 4, 6, and 8) also give rise to a nearly identical feature at this temperature[24, 32]. Following our previous studies[32], we attribute the single TPD peak to confined 3D water clusters near the step edge. Additionally, the spectra (between 0 and 12 ML) seem to have non-overlapping leading edges, but we note three different coverage regions (0 - 2 ML, 2 - 4.5 ML and 4.5 - 12 ML) for which the leading edges do overlap perfectly. At these coverage regimes, TPD shows zero-order desorption kinetics. The separation in the spectra suggests a layer-by-layer growth on the fully hydrogenated Pt(211) as illustrated in the inset schematic of figure 6.1. Later on, we provide a detailed kinetic analysis to shed light on the origin of these separated water layers.

Figure 6.2 shows traces of varying amounts of water desorbing from Pt(211)

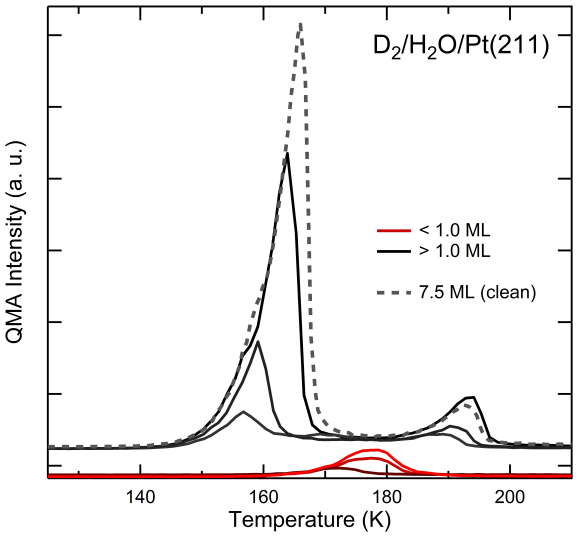

Figure 6.2: TPD spectra of increasing amounts of H_2O desorbing from 250 L D_2 post-dosed on Pt(211). The dotted spectrum is 7.5 ML of water desorbing from the bare surface.

onto which D_2 was dosed after H_2O dosing. To obtain these spectra, we exposed various amounts of H_2O to the clean surface at 95 - 100 K. Next, 250 L of deuterium were background dosed on the water covered surface at the same temperature. We confirm that 250 L of D_2 exposure on the bare Pt(211) is more than the amount which is enough to fully hydrogenate the surface under background dosing conditions[29]. The red and black spectra correspond to coverages of θ_{H_2O} < 1.0 ML and > 1.0, respectively. To show the clear difference in the spectra for coverages < 1.0 ML and > 1.0, we used different offsets. The dotted spectrum is 7.5 ML of H_2O desorbing from the clean surface. Below 1.0 ML of water coverage, the desorption from post-deuterated Pt(211) takes place in a single peak, centered below 180 K. In the sub-monolayer coverage regime, water desorption from clean Pt(211) appears at higher temperatures, 195 K[15, 29]. This significant temperature shift indicates that post-dosed D_2 lowers the binding energy for water. In our previous D_2 and H_2O co-adsorption study on Pt(533), Pt(755) and Pt(977)[32], we reported a similar behaviour. With increasing water exposure, the lowering effect in binding energy seems to vanish as the desorption peak at 180 K shifts to a higher temperature. Moreover, the TPD spectra look nearly identical to water desorption spectra from the clean surface (dotted spectrum) at higher water coverages.

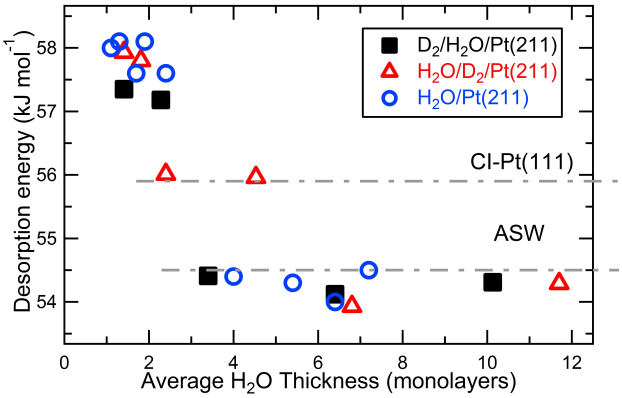

Figure 6.3: Energies of desorption at different water coverages. The red triangles and black squares indicate $H_2O/D_2/Pt(211)$ and $D_2/H_2O/Pt(211)$, respectively. The blue circles represent the E_d of water on a clean surface.

Although an ideal multilayer desorption feature displays an exponential increase in desorption rate with increasing temperature, the onsets of the H_2O multilayer desorption from clean, pre-hydrogenated and post-hydrogenated Pt(211) display a deflection at $\sim$ 156 K (figure 6.1 and 6.2). This deflection in the TPD spectrum below 170 K has previously been associated with crystallization of amorphous solid water (ASW) to crystalline ice (CI)[14, 15, 33, 34]. We have shown in chapter 5 in detail how very small differences in substrate structure influence crystallization of ultra thin water films significantly[15]. In the following section, we will show the role of co-adsorbed D on the crystallization of water on Pt(211).

Figure 6.3 illustrates the desorption energies (E_{des}) of H_2O as a function of water thickness. Water layer thicknesses are expressed in terms of our 1 $ML^{(111)}$ reference, as discussed in detail elsewhere[15]. The blue circles, black squares and red triangles represent $H_2O/Pt(211)$, $D_2/H_2O/Pt(211)$ and $H_2O/D_2/Pt(211)$, respectively. We obtained E_{des} by leading edge analysis[15]. The horizontal lines indicate the desorption energies of ASW and CI grown on Pt(111)[14, 33]. We note that our obtained E_{des} for ASW phase is ca. 1 kJ mol^{-1} lower than the reported values for thick water layers on Pt(111)[33, 35]. We believe that this minor difference may be associated with using a very narrow temperature regime to obtain the corresponding desorption kinetics. Nevertheless, our values indicate a clear difference between the water layers.

We have previously shown[15] that, when water is adsorbed below 100 K, CI-like and ASW layers grow on Pt(211) with desorption energies of 57.9 and 54.5 kJ

mol^{-1} (blue circles), respectively. For $D_2/H_2O/Pt(211)$, the obtained desorption energies are nearly identical to water desorption from the bare Pt(211). In both experiments crystallinity is maintained in the first two layers. This suggests the formation of very similar CI-like and ASW phases on bare and post-hydrogenated surfaces. On the other hand, for $H_2O/D_2/Pt(211)$ we note three different E_{des} at $\sim$ 57.8, 56.0 and 54.5 kJ mol^{-1}. This is also reflected on the TPD spectrum in figure 6.1. Because of distinct E_{des} obtained for three different water layers, TPD shows separated regimes between 0 - 2 ML, 2 - 4.5 ML and 4.5 - 12 ML. We attribute the calculated desorption energies for $H_2O/D_2/Pt(211)$ at 57.8 and 54.5 kJ mol^{-1} to CI-like and ASW phases, respectively. The obtained energies also suggest that CI-like formation is maintained in the first two layers similar to H_2O on the clean and post-deuterated Pt(211). However, between θ_{H_2O} = 2 - 5 ML, the desorption energy drops to 56 kJ mol^{-1}, signaling a different water phase. We note that this obtained E_{des} is identical to reported desorption energy of CI on Pt(111)[33, 35] (horizontal dotted lines in figure 6.3). Hence, we suggest that this phase is still crystalline. Finally, at $\theta_{H_2O} > 6$ ML, the E_{des} drops to 54.5 kJ mol^{-1} revealing the formation of ASW similar to water on clean and pre-deuterated Pt(211).

On D_2 pre-covered Pt(211), water grows crystalline in the first five layers (two layers as CI-like, three layers as CI). By comparison to clean and post-hydrogenated surfaces, the crystallinity is maintained over three additional layers on pre-hydrogenated surface. Picolin et al.[16] previously showed that highly corrugated surfaces suppress the formation of CI layers. Also in our previous study, we reported that crystallinity is maintained over a larger thickness on the less corrugated Pt surface[15]. Hence we suggest that pre-deuterating the surface introduces a smoothening effect to the corrugated surface.

To elucidate to what extent the sequence of the co-adsorbed D_2 influences the isotopic exchange, we show the isotopic partitioning of HD and HOD from the D_2 and H_2O co-adsorption experiments as a function of H_2O coverage in figure 6.4. The data in this figure are obtained by monitoring HD and HOD desorption rates during our TPD experiments as shown in figure 6.1 and 6.2. The top and middle panels show the isotopic exchange of HD and HOD, respectively. The bottom panel displays the absolute amounts of D_2 desorbing from post-and-pre-deuterated Pt(211). Our preliminary H_2O and D_2 experiments on clean Pt(211) showed no desorption traces of HD and HOD. Hence, the obtained coverages are only due to the isotopic exchange between H_2O and D_2. The red data points correspond to water dosed onto D_2 pre-covered Pt(211), $H_2O/D_2/Pt(211)$, and the black data points indicate the water dosed onto D_2 post-covered Pt(211), $D_2/H_2O/Pt(211)$. The dotted lines fitted through the data are only a guide for

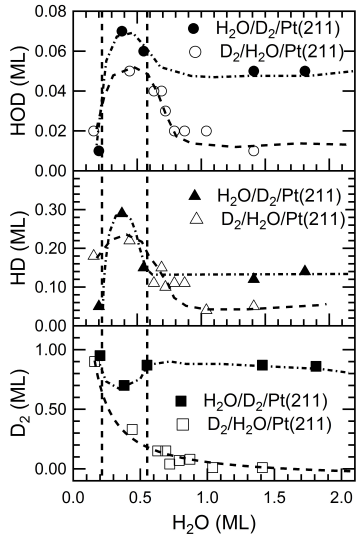

Figure 6.4: The top and middle panels show isotopic partitioning of HOD and HD as a function of water coverage, respectively. The bottom panel shows D_2 coverage. The solid (red) and empty (black) markers indicate $H_2O/D_2/Pt(211)$ and $D_2/H_2O/Pt(211)$, respectively. The lines fitted to the data are only a guide for the eye.

the eye.

We observe that both $H_2O/D_2/Pt(211)$ and $D_2/H_2O/Pt(211)$ give rise to a maximum amount of HOD and HD exchange at $\theta_{H_2O} \approx 0.4$ ML. On a fully deuterated Pt(533), Pt(755), and Pt(977) the maximum isotopic partitioning is also obtained at a nearly identical coverage[32, 36]. The combined results suggest that the HD and HOD exchange on a fully deuterated Pt is not influenced by the terrace length.

In our co-adsorption experiments, we observe two distinct behaviours for deuterium desorption (bottom panel in figure 6.4). For $D_2/H_2O/Pt(211)$, the amount of deuterium desorbing ($D_{2,des}$) from Pt(211) decreases with water coverage, $\theta_{H_2O} < 1.0$ ML. Under these conditions deuterium adsorption seems only achievable when water does not wet the entire surface. This agrees with the lack of significant isotopic exchange for the $D_2/H_2O/Pt(211)$ system at $\theta_{H_2O} > 1.0$ ML. On the other hand, when reversing the desorption order, $H_2O/D_2/Pt(211)$, the $D_{2,des}$ from Pt(211) is nearly 1.0 ML and hardly drops with prolonged water exposure. The adsorbed water molecules does not displace the dissociated D_{ad} on the surface. In addition, in figure 6.5, we show the TPD spectra of D_2 and H_2O

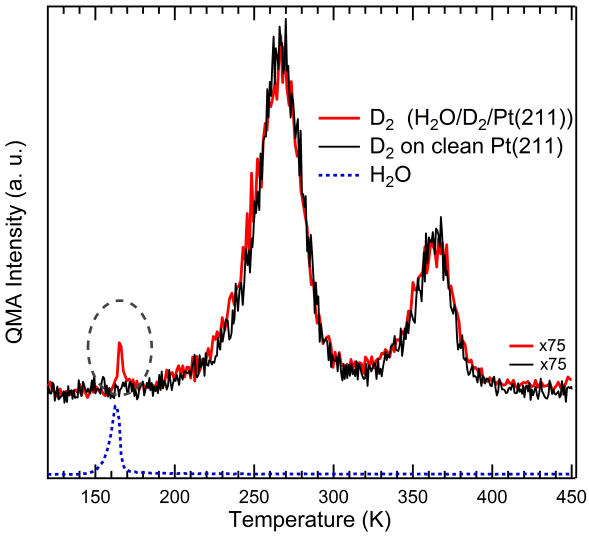

Figure 6.5: TPD spectra of D_2 (red) and H_2O (blue) for $\theta_D = 1.0$ ML pre-dosed on Pt(211). The black spectrum is 1.0 ML of D_2 desorbing from clean surface[29]. The dotted, grey circle shows the early D_2 desorption as a result of trapping.

desorbing from pre-deuterated Pt(211). We have previously shown the deuterium desorption from Pt(211) in chapter 4. Briefly D_2 desorption takes place in two peaks. The high and low temperature peaks are attributed to desorption from (100) steps and (111) terraces, respectively. For $H_2O/D_2/Pt(211)$, the D_2 spectrum (red spectrum) gives an additional peak, which is not observed when D_2 is dosed on the clean Pt(211) (black spectrum), at 160 K. Note that the onset of the water desorption (blue dotted spectrum) coincides with the desorption of this additional D_2. The desorption intensity of this feature, which corresponds to $\sim$0.01 ML of D_2, does not increase with prolonged water exposure.

Smith et al. have observed a similar desorption feature for CCl_4 desorption on water post-dosed Au(111). They attributed this peak to the nucleation and growth of CI from ASW[37]. For $H_2O/D_2/Pt(211)$, the peak at 160 K cannot signal the crystallization because water is already crystalline in the first five layers, as shown in (figure 6.3). Furthermore, theoretical[38] and astrophysical[39] studies for D_2 desorption show that hydrogen may bind chemically, but without dissociation, near steps at < 50 K. In this study, as mentioned earlier, we dose D_2 on the bare surface at significantly higher temperatures, 95 - 100 K. Therefore molecular D_2 cannot be trapped by the post-dosed H_2O to give a delayed desorption feature at 160 K.

Van der Niet et al.[24] have also reported a similar D_2 desorption feature on a water post-covered Pt(553), Pt[4(111)x(110)], at 163 K. Unlike H_2O/D_2/Pt(211), this peak grows in intensity as a function of water coverage and delays the onset of deuterium desorption feature. They suggested that this peak is associated with H_2O adsorbing on the (110) steps. Once the water, adsorbed on these (110) step sites, starts to desorb, the underlying D_{ad} can desorb as well. Although Pt(211) is only supposed to have three atom wide (111) terraces truncated by (100) steps, the actual sample contains (110) steps as defect sites too. Following van der Niet et al.[24], we associate the peak at 160 K with the D_2 desorption from the (110) step defects on Pt(211). Therefore, the integral of the D_2 peak at 160 K, 0.01 ML, reflects the absolute amount of (110) step defects, 1 %, present on the crystal. Their occurrence may be due to both a minor azimuthal miscut of the crystal and their entropically required presence for a perfectly stepped crystal at temperatures well above T = 0 K. Figure 6.6 shows the schematic representation of the (110) step defects on a Pt(211) crystal. The arrows indicate the sites, introduced by these defects. These defects clearly have different adsorption sites than the regular (100) step sites. The dissociated D_{ad} can adsorb onto these defect sites and give rise to the desorption feature at 160 K, as shown in figure 6.5.

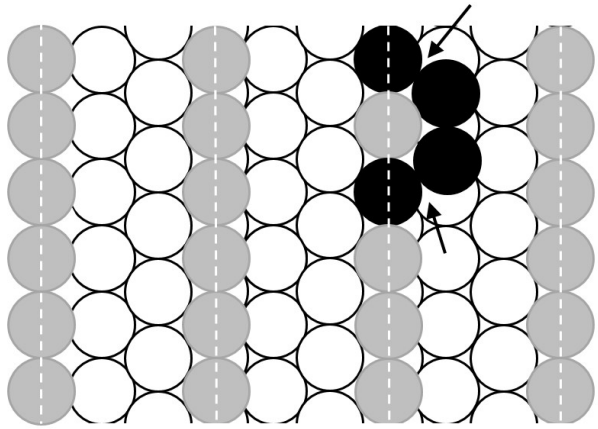

Figure 6.6: Schematic representation of a Pt(211) crystal with (110) step defects. The arrows indicate the (110) step defects that give rise to the desorption feature at 160 K as shown in figure 6.5.

6.5 Conclusion

In conclusion, we have shown that H_2O adsorbed on post- and pre-hydrogenated Pt(211) have markedly different characteristics. Fully deuterating the surface prior to water adsorption makes Pt(211) hydrophobic, similar to other (100) stepped Pt(111) surfaces with n = 4, 6, and 8. Post-deuteration does not change the wetting behaviour of the surface but lowers the binding energy of water at $\theta_{H_2O} < 1.0$ ML. Both co-adsorption experiments yield the maximum isotopic partitioning at the sub-monolayer water coverages. Furthermore, the desorption kinetics have been studied systematically for different water coverages. We find that post-deuteration of the surface does not influence crystallization kinetics of water. However, pre-deuteration of the highly corrugated surface introduces a smoothening effect. This effect introduces an additional CI phase, that is not observed when H_2O is adsorbed on clean or post-hydrogenated surface. Additionally, crystallization of water on pre-hydrogenated Pt(211) is maintained over a double thickness by comparison to water on clean and post-hydrogenated surface. Finally, we have shown that (110) step defects on pre-deuterated Pt[n(111)x(100)] samples can be revealed to an extent as low as 1 % or lower. We believe that our results give new insights into water-metal and gas-surface reactions taking place on metal surfaces, in particular concerning the crystallinity of water layer layers in dependence of the structural and chemical nature at the underlying substrate.

6.6 Bibliography

References

(1) Filhol, J.-S.; Neurock, M. *Angewandte Chemie International Edition* **2006**, *45*, 402–406.

(2) Rossmeisl, J.; Nørskov, J. K.; Taylor, C. D.; Janik, M. J.; Neurock, M. *The Journal of Physical Chemistry B* **2006**, *110*, 21833–21839.

(3) Nisini, B. *Science* **2000**, *290*, 1513–1514.

(4) Kouchi, A. *Nature* **1987**, *330*, 550–552.

(5) Mayer, E.; Pletzer, R. *Nature* **1986**, *319*, 667–674.

(6) Stevenson, K. P.; Kimmel, G. A.; Dohnalek, Z; Smith, R. S.; Kay, B. D. *Science* **1999**, *283*, 1505–1507.

(7) Thürmer, K.; Nie, S. *Proceedings of the National Academy of Sciences of the United States of America* **2013**, *110*, 11757–11762.

(8) Baldwin, R. L. *Science* **2002**, *295*, 1657–1658.

(9) Fecht, H. J. *Nature* **1992**, *356*, 133–135.

(10) Carrasco, J.; Hodgson, A.; Michaelides, A. *Nature materials* **2012**, *11*, 667–674.

(11) Hodgson, A.; Haq, S. *Surface Science Reports* **2009**, *64*, 381–451.

(12) Henderson, M. A. *Surface Science Rep.* **2002**, *46*, 1–308.

(13) Thiel, P. A.; Madey, T. E. *Surface Science Reports* **1987**, *7*, 211–385.

(14) Löfgren, P; Ahlström, P; Chakarov, D. *Surface Science* **1996**, *367*, L19–L25.

(15) Badan, C.; Heyrich, Y.; Koper, M. T. M.; Juurlink, L. B. F. *The Journal of Physical Chemistry Letters* **2016**, 1682–1685.

(16) Picolin, A.; Busse, C.; Redinger, A.; Morgenstern, M.; Michely, T. *The Journal of Physical Chemistry C* **2009**, *113*, 691–697.

(17) Amiaud, L; Fillion, J.; Baouche, S; Dulieu, F; Momeni, A; Lemaire, J. *The Journal of chemical physics* **2006**, *124*, 094702.

(18) Fillion, J.-H.; Amiaud, L.; Congiu, E.; Dulieu, F.; Momeni, A.; Lemaire, J.-L. *Physical Chemistry Chemical Physics* **2009**, *11*, 4396–4402.

(19) Koper, M. T. M. *Nanoscale* **2011**, *3*, 2054–2073.

(20) Fajín, J. L. C.; D. S. Cordeiro, M. N.; Gomes, J. R. B. *The Journal of Physical Chemistry A* **2014**, *118*, 5832–5840.

(21) Kolb, M. J.; Farber, R. G.; Derouin, J.; Badan, C.; Calle-Vallejo, F.; Juurlink, L. B. F.; Killelea, D. R.; Koper, M. T. M. *Physical Review Letters* **2016**, *116*, 136101.

(22) Peköz, R.; Wörner, S.; Ghiringhelli, L. M.; Donadio, D. *The Journal of Physical Chemistry C* **2014**, *118*, 29990–29998.

(23) Den Dunnen, A.; van der Niet, M. J. T. C.; Koper, M. T. M.; Juurlink, L. B. F. *Journal of Physical Chemistry C* **2012**, *116*, 18706–18712.

(24) Van der Niet, M. J.; den Dunnen, A.; Koper, M. T.; Juurlink, L. B. *Physical review letters* **2011**, *107*, 146103.

(25) Morgenstern, M; Michely, T; Comsa, G *Physical Review Letters* **1996**, *77*, 703–706.

(26) Endo, O.; Nakamura, M.; Sumii, R.; Amemiya, K. *Journal of Physical Chemistry C* **2012**, *116*, 13980–13984.

(27) Nakamura, M.; Sato, N.; Hoshi, N.; Soon, J. M.; Sakata, O. *Journal of Physical Chemistry C* **2009**, *113*, 4538–4542.

(28) Roman, T.; Groß, A. *Catalysis today* **2013**, *202*, 183–190.

(29) Badan, C.; Koper, M. T. M.; Juurlink, L. B. F. *The Journal of Physical Chemistry C* **2015**, *119*, 13551–13560.

(30) Grecea, M. L.; Backus, E. H. G.; Riedmuller, B; Eichler, A; Kleyn, A. W.; Bonn, M *Journal of Physical Chemistry B* **2004**, *108*, 12575–12582.

(31) Gee, A. T.; Hayden, B. E. *The Journal of Chemical Physics* **2000**, *113*, 10333–10343.

(32) Den Dunnen, A.; van der Niet, M. J. T. C.; Badan, C.; Koper, M. T. M.; Juurlink, L. B. F. *Physical Chemistry Chemical Physics* **2014**, 8530–8537.

(33) Smith, R. S.; Matthiesen, J.; Knox, J.; Kay, B. D. *Journal of Physical Chemistry A* **2011**, *115*, 5908–5917.

(34) Backus, E. H. G.; Grecea, M. L.; Kleyn, A. W.; Bonn, M. *Physical Review Letters* **2004**, *92*, 236101–236104.

(35) Löfgren, P.; Ahlström, P.; Lausma, J.; Kasemo, B.; Chakarov, D. *Langmuir* **2003**, *19*, 265–274.

(36) Van der Niet, M. J. T. C.; Dominicus, I.; Koper, M. T. M.; Juurlink, L. B. F. *Physical Chemistry Chemical Physics* **2008**, *10*, 7169–7179.

(37) Smith, R. S.; Huang, C; Wong, E.; Kay, B. D. *Physical review letters* **1997**, *79*, 909.

(38) McCormack, D. A.; Olsen, R. A.; Baerends, E. J. *The Journal of chemical physics* **2005**, *122*, 194708.

(39) Hornekær, L.; Baurichter, A.; Petrunin, V. V.; Luntz, A. C.; Kay, B. D.; Al-Halabi, A *The Journal of chemical physics* **2005**, *122*, 124701.

Chapter 7

Step-Type Selective Oxidation of Pt Surfaces

7.1 Abstract

Herein, we report on a combined TPD and STM study of O_2 adsorption and dissociation on various Pt surfaces with widely varying (111) terrace widths. Our quantitative TPD results show that (110) stepped surfaces adsorb considerably more oxygen at 100 K, regardless of terrace width, than either (100) stepped surfaces or planar Pt(111). These results suggest that O_2 dissociates on the (110) stepped surfaces at 100 K, well lower than required for temperature-induced dissociation on (111) planes. The amount of oxygen desorbing from recombinative desorption of adsorbed oxygen atoms is also greater on (110) stepped surfaces. In addition, the partitioning of adsorbed oxygen between molecular and dissociative states depends on the step geometry; (110) stepped surfaces show an uptake plateau indicative of a threshold surface concentration for low-temperature dissociation, whereas (100) stepped surfaces do not. Scanning tunneling microscope (STM) images for various O coverages and surface deposition temperatures confirm low temperature dissociation on a (110) stepped surface. The STM

images also show that terrace width is not a factor in the lowered dissociation barriers for O_2 on (110) stepped surfaces.

Based on: Badan, C.; Farber R. G.; Heyrich, Y.; Koper, M. T. M.; Killelea, D. R.; Juurlink, J. Phys. Chem. C, 2016, DOI: 10.1021/acs.jpcc.6b05482

7.2 Introduction

The interaction of oxygen with Pt and other late transition metal surfaces is crucial for many applications of heterogeneous oxidation catalysis such as fuel processing and remediation of exhaust gases[1–4]. In actual industrial catalytic systems, the degree of surface oxidation is key to the catalytic reactivity and behavior. Therefore, numerous experimental and theoretical studies have been conducted to determine the nature of this strong oxidation dependence. Thus far, well defined, low defect surfaces, such as Pt(111) and Pt(100), have revealed much about how O_2 adsorbs and dissociates on Pt surfaces and how the Pt surface is altered upon oxidation[1, 2, 5–7].

O_2 dissociates on Pt(111) to form adsorbed oxygen (O_{ad}), and prolonged O_2 exposures will saturate the surface with an adsorbed oxygen coverage ($\theta_{O_{ad}}$) of 0.25 monolayers (ML) in a (2x2)-O adsorbate layer. Formation of O_{ad} on Pt(111) is a precursor-mediated process where O_2 first sticks to the surface as molecularly chemisorbed O_2 ($O_{2,ad}$). The temperature of the surface (T_s) determines the lifetime and coverage of $O_{2,ad}$ ($\theta_{O_{2,ad}}$); dissociation into O_{ad} is in competition with molecular desorption to O_2 (g). Both processes are thermally activated, but the barrier to desorption is typically lower than dissociation. This results in a surface temperature effect where elevated T_s provide the energy needed for dissociation, but shorten the precursor residence time. If the T_s is too low, there is insufficient thermal energy to dissociate O_2, resulting in stable $O_{2,ad}$. When the surface is warmed, $O_{2,ad}$ is then able to dissociate, but in competition with desorption[1, 8, 9]. $O_{2,ad}$ has also been identified on planar and stepped Pt surfaces using scanning tunneling microscopy (STM)[10], temperature programmed desorption (TPD)[11], and electron-energy-loss spectroscopy (EELS)[12]. On Pt(111), recombinative desorption of dissociated O atoms occurs between 500 K and 850 K in a TPD experiment[11, 13–21]. O_2 exposure at elevated temperatures (400 - 600 K) results in excess of 0.25 ML O, the maximum coverage for oxygen adsorption on Pt(111). Additionally, surface oxidation at coverages greater than 0.25 ML has been observed when using oxygen sources other than O_2[6, 7, 13, 16, 17, 22] such as atomic oxygen[17], electron bombardment of an O_2 covered surface[15], or using NO_2[23] or O_3[24]. The reaction probability is coverage dependent; specifically at low coverages, the dissociation of O_2 on Pt surfaces is enhanced by the presence of O_{ad}[18, 23].

On the more corrugated Pt(110) surface, O_2 dissociation also exhibits a similar temperature dependence. Only $O_{2,ad}$ forms below 180 K, but O_2 can dissociate to O_{ad} at higher temperatures[25]. The saturation coverage of O_{ad} on Pt(110) is 0.25 ML, forming a (2x1) O adlayer, that is the most stable structure for a wide range of conditions[26]. Extended exposures to either atomic oxygen (AO) or high

pressure O_2 exposures lead to higher coverage surface structures, whose stability is strongly temperature dependent[27, 28].

It is well known that steps and other defect sites increases the total reactivity of the surface, particularly for molecularly adsorbed species[1, 29] such as chemisorbed O_2. Theoretical calculations and experimental studies attribute the observed increase in reactivity to the local lowering of the dissociation barriers in close proximity to the step sites[30, 31] as well as to changes in the d-band local density of states of the Fermi energy at kinks on the stepped surface[1]. While it is known that steps and kinks are an essential component for dissociation on metal surfaces, it is unknown whether dissociation mechanisms are enhanced by particular step geometries.

In this study, we investigated the extent to which step geometry influences oxygen dissociation on Pt surfaces. We have used Pt[n(111)x(100)] and Pt[n(111)x(110)] surfaces with n = 3 and 4, respectively. These highly corrugated surfaces have step densities similar to those found on nanoparticles. TPD experiments on several different Pt crystal surfaces were performed in a single UHV chamber with identical thermocouple connections and measurement conditions allowing for direct comparison of the obtained data. As a complement to high resolution TPD data, scanning tunneling microscopy (STM) was used to study the temperature and coverage dependence of O_2 dissociation on Pt(553), which can be further used to explain the dissociation behavior at (110) step types.

7.3 Experimental Section

The equipment and detailed procedures used for angle-resolved TPD experiments at Leiden University have been described elsewhere [18, 32]. Briefly, we use a home-built UHV system with a base pressure of 5×10^{-11} mbar. The chamber is equipped with a differentially pumped quadrupole mass spectrometer (QMS, Baltzers QMA400) that only detects desorption from the polished side of our disk-shaped Pt single crystals. The canister's volume is ∼1.5 L, most of which is occupied by the QMS itself. It is pumped by a 240 L/s turbomolecular pump positioned along the QMS rods, ensuring high pumping speed in the entire volume. In this study, we have used five samples with different surface orientations, most of which were cut from a Pt single crystal boule (Surface Preparation Laboratory, Zaandam, The Netherlands). They are all 10 mm diameter and 1-2 mm thick, have a purity better than 5N, and are aligned with an orientation better than 0.1° from the indicated surface. We cleaned the polished side of our crystals under UHV conditions by repetitive sputtering-annealing cycles. Additionally, all samples were heated at 1200 K for 5 min after each TPD experiment. The samples were

heated radiatively and/or by electron bombardment using a filament (Osram, 250 W) positioned ~ 2 mm behind the crystal. Liquid N_2 was used for cooling during surface preparation and subsequent experiments. The surface temperature, T_s, was measured using K-type thermocouples; each sample has a permanently affixed thermocouple laser welded to its top edge. We have used low energy electron defraction (LEED) (VG RVL 900) to check the surface order and have shown the relevant LEED patterns elsewhere [18, 19, 32]. The calculated spot-row spacing to spot-splitting ratios of these surfaces correspond well to literature values[33]. The LEED patterns confirm long-range order with the expected average terrace width for each of the Pt surfaces. We have also performed a beam energy analysis of the (0,0) spot-splitting of each of the Pt surfaces to confirm that steps are of mono-atomic height [34].

Oxygen (Messer, 5.0) was dosed directly onto the polished surface of the single crystals between 95 K and 100 K using a leak valve with a 6 mm diameter tube attached inside the UHV chamber. We dosed at a fixed distance between sample and the end of this tube. This ensured localized, highly reproducible, O_2 deposition for all five single crystal samples used in this study. During dosing, all filaments in the UHV chamber were switched off. The pressure was monitored by a cold cathode gauge. The heating rate for all subsequent TPD experiments was 1.0 K s^{-1}. To allow for quantitative comparison of TPD spectra obtained from different crystals, the assembly holding our samples contains an isolated copper stud that protrudes from the polished surface just above the crystal. We positioned the samples with high accuracy relative to the 5 mm diameter orifice in the differentially pumped QMS's housing by retracting the sample a fixed distance after the copper wire made electrical contact with the housing. Coverages were obtained from TPD experiments by integrating the QMS signal. The integrated O_2 TPD signal between 500 and 900 K from Pt(111) with saturation coverage of 0.25 ML was used as a reference[11, 14, 15, 35, 36]. Additional details regarding the experimental apparatus, O uptake on Pt surfaces, and calibration of the TPD data are provided in the Supporting Information.

Scanning tunneling microscopy (STM) experiments were performed at Loyola University. Equipment and procedures have been described previously in detail [37]. Briefly, the Pt(553) surface was cleaned following published procedures[20]. Surface cleanliness was confirmed via Auger electron spectroscopy and a sharp LEED pattern[19]. The cleaned Pt(553) surface was dosed at either $T_s = 100$ K or 400 K by backfilling the chamber with O_2. The exposure was verified with a QMS monitoring the O_2 partial pressure. After O_2 exposure, the crystal was cooled to around 90 K, inserted into the STM, and then further cooled to 30 K for imaging. Oxygen coverage was measured via TPD, and agreed well with the

TPD measurements taken in Leiden, as reported in a previous publication[38]. TPDs taken after imaging showed neither any decrease in O_2 desorption nor the accumulation of background gases on the sample. All STM images were obtained with Pt/Ir tips in constant-current scanning mode.

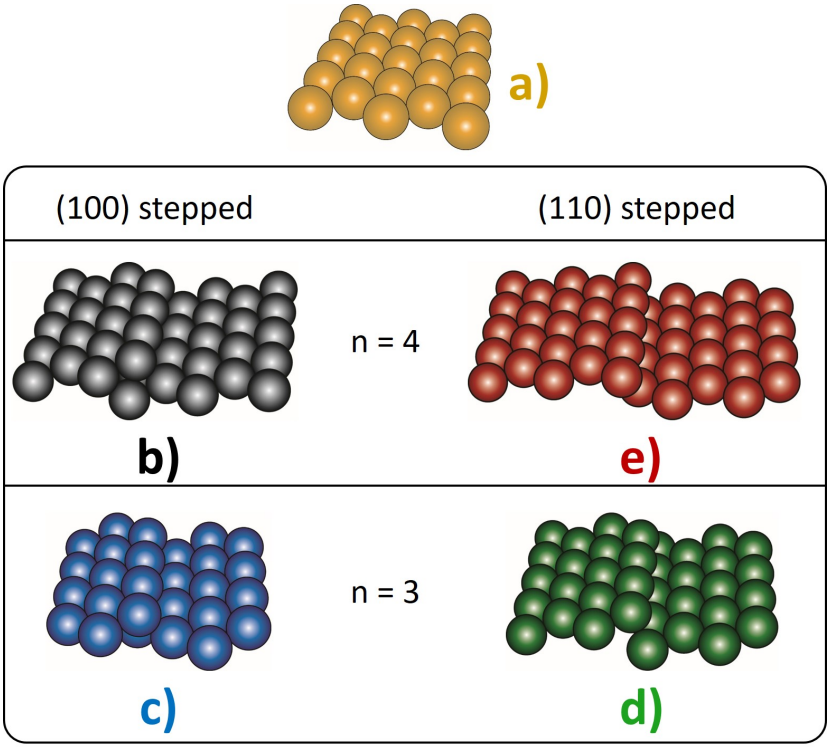

Figure 7.1: Schematic representation of a) Pt(111), b) Pt(533), c) Pt(211), d) Pt(221) and e) Pt(553). The LEED patterns are shown elsewhere [18, 19].

Figure 7.1 shows a schematic representation of Pt(111), Pt(533), Pt(221), Pt(553) and Pt(211) surfaces used in this study. Pt(211) and Pt(221) surfaces consist of three atom wide (111) terraces truncated with (100) and (110) step sites, respectively. Pt(533) and Pt(553) surfaces have four atom wide (111) terraces with (100) and (110) step geometries. Surfaces having 'n' atom wide (111) terraces with (110) step geometries can also be described as surfaces with 'n+1' atom wide (111) terraces truncated with (111) steps.

7.4 Results and discussion

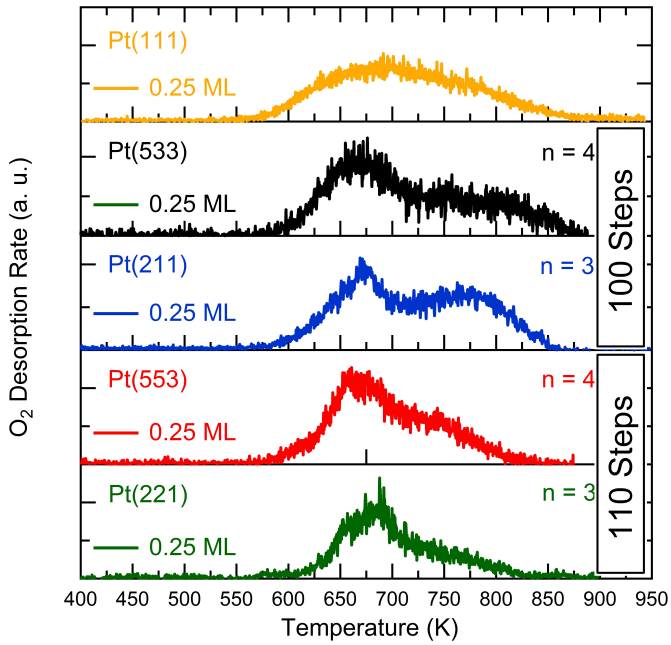

Figure 7.2: O_2 TPD spectra for Pt(111), Pt(211), Pt(221), Pt(553) and Pt(533) at 0.25 ML of recombinative oxygen coverage. n = terrace length of the (100) or (110) stepped surfaces.

Figure 7.2 shows TPD spectra for the recombinative desorption of O_2 from Pt(111), Pt(533), Pt(211), Pt(553), and Pt(221) after dosing with molecular oxygen at T_s = 100 K. The value of 'n' shown in Figure 7.2, indicates the terrace width of the Pt surfaces with (100) or (110) step geometries. As shown in previous work, O_2 desorption from Pt(111) occurs in a single, broad desorption peak[11, 14, 15, 35, 36, 39, 40] centered between 550 K and 750 K. This feature shows typical characteristics of second-order desorption kinetics. The maximum desorption rate for O_{ad} shifts to lower temperatures with increasing coverage and saturates at $\theta_{O_{ad}}$ = 0.25 ML. The TPD peak shape and the relative desorption kinetics are in good agreement with previous reports for Pt(111). Figure S2 in the supporting information quantitatively compares the uptake curve for Pt(111) to previous studies[11, 15].

On stepped surfaces, the broad desorption peak seen on Pt(111) separates into two desorption features. For both Pt(211) and (221), the lower temperature

feature is from recombinative desorption of O_{ad} from (111) terrace sites, whereas the higher temperature peak results from recombinative desorption from step sites [19–21, 41–43]. At $\theta_{O_{ad}} = 0.25$ ML, the peak desorption rate occurs at varying temperatures depending on step geometry. O_2 desorbs at a ~ 25 K lower temperature from (110) stepped surfaces than from (100) stepped surfaces, as reported previously[19]. The difference in desorption temperature was explained by density functional theory (DFT) calculations[44, 45] as arising from O atoms binding more strongly to (100) step sites than (110) step sites. Figure S1 in the supporting information provides additional information on the comparison and quantification of coverages for the various Pt surfaces.

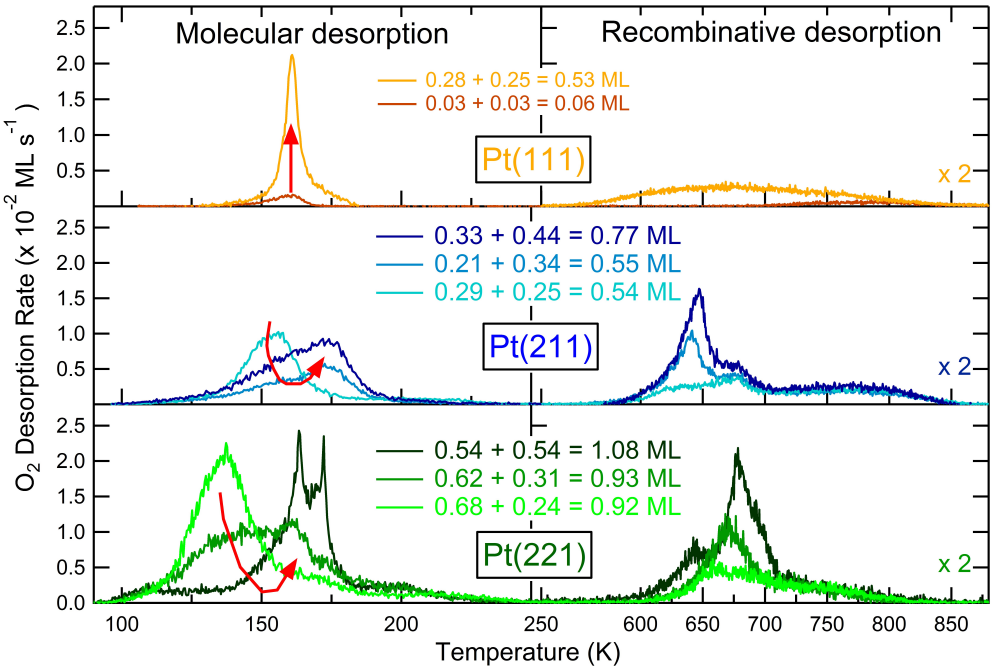

Figure 7.3: O_2 TPD spectra for a range of O_2 coverages obtained for O_2 doses at $T_s = 100$ K. The panels correspond to Pt(111) in the top panel, Pt(211) with (100) steps in the middle panel, and Pt(221) with (110) steps in the bottom panel.The left column shows desorption of molecularly adsorbed O_2, the right column shows recombinative desorption of O_{ad}.

O_2 dissociation at high temperature is not the only way oxygen can stick to Pt surfaces. At lower temperatures ($T_s < 150$ K), O_2 can molecularly adsorb as $O_{2,ad}$; an intact O_2 molecule chemisorbed to the surface. At low temperatures,

dissociatively chemisorbed O goes through an $O_{2,ad}$ precursor and both O_{ad} and $O_{2,ad}$ will be present on the surface. The total oxygen coverage (θ_O^{tot}) and the fraction of O_{ad} and $O_{2,ad}$ are strongly dependent on T_s[1, 8]. In order to thoroughly compare the O_2 adsorption behavior for the various crystal faces, TPD experiments were carried out in the $O_{2,ad}$ and O_{ad} temperature regimes; results are shown in figure 7.3. $O_{2,ad}$ desorbs from Pt(111) at 160 K, as seen in the top-left panel of figure 7.3, and O_{ad} atoms recombinatively desorb in the previously discussed broad, second-order desorption peak[19] (figure 7.2) shown in the top-right panel of figure 7.3. On Pt(111), exposures of up to 900 Langmuir (1 Langmuir = 10^{-6} Torr s^{-1}) O_2 demonstrate that $\theta_{O_{2,ad}}$ saturates at 0.28 ML, just slightly greater than the saturation coverage of 0.25 ML for O_{ad}, yielding θ_O^{tot} of 0.53 ML. We note that after extended O_2 exposures, the $O_{2,ad}$ desorption peak slightly shifted to a higher temperature, but the integrated intensity (total O) was unchanged. The total coverage of 0.53 ML is in good agreement with previous work done by Steininger et al., which, however, only explored O_2 exposures up to 40 Langmuir, so the desorption temperature shift was not observed[15].

The center panels of figure 7.3 show O_2 TPD data for Pt(211), 3-atom wide terraces with (100) steps, for three different θ_O^{tot}, 0.54 ML, 0.55 ML, and 0.77 ML. The partitioning between $\theta_{O_{ad}}$and $\theta_{O_{2,ad}}$ developed in an interesting fashion with increasing θ_O^{tot}. At θ_O^{tot} = 0.54 ML (figure 7.3, light blue), $O_{2,ad}$ desorbs in a single desorption peak at 155 K corresponding to $\theta_{O_{2,ad}}$= 0.29 ML (figure 7.3 center, left). The higher temperature TPD features (figure 7.3, center, right) arise from recombinative desorption of O_{ad}, and exhibit the saturation coverage of 0.25 ML discussed previously. With slightly larger exposure of O_2, the total O coverage modestly increased to 0.55 ML; however, the TPD features changed dramatically (figure 7.3, blue). At θ_O^{tot} = 0.55 ML, the intensity of the original $O_{2,ad}$ peak at 155 K diminished significantly, $\theta_{O_{2,ad}}$ decreased from 0.29 ML to 0.21 ML, and appears to split into two components; the original 155 K peak and a new peak at 174 K. The higher temperature desorption features also changed. The shoulder at 647 K develops into a sharp, well-defined peak while the higher temperature feature at 667 K did not increase with oxygen coverage. Likewise, the desorption of O_{ad} from steps between 700 K and 900 K was unchanged for all coverages discussed here. Continued exposure of Pt(211) to O_2 at T_s = 100 K saturated at θ_O^{tot} = 0.77 ML (figure 7.3, dark blue), and the TPD features were unaltered with additional O_2 exposure. At θ_O^{tot} = 0.77 ML, $\theta_{O_{2,ad}}$ increased to 0.33 ML and the shape of the desorption peak is similar to the peaks seen for θ_O^{tot} = 0.55 ML. Likewise, a monotonic increase in the higher temperature features is evident. The sharp peak at 647 K increased in intensity, and the other features remained the same. We have previously found that the stoichiometry and sharp desorption feature at 647 K

indicates formation of PtO lines on the (100) steps[18]. The general similarity that both Pt(111) and Pt(211) reach a saturation coverage suggest that dissociation of molecularly adsorbed oxygen only occurs during the temperature ramp. The sudden change in peak shape and distribution over molecular versus recombinative desorption around 0.55 ML indicates threshold behavior for dissociation. Above $\theta_{O_{ad}} = 0.25$ ML dissociation is enhanced during the temperature ramp at the expense of molecular desorption.

We now discuss O_2 desorption from Pt(221), which also has 3-atom wide terraces, like Pt(211), but the arrangement of the atoms along the step edges differ. Pt(221) has (110) step geometry instead of (100) as was the case for Pt(211). The lower panels in figure 7.3 show TPD data for O_2 desorption from Pt(221) with $\theta_O^{tot} = 0.92$ ML (light green), 0.93 ML (green), and 1.08 ML (dark green). It is worth noting that the oxygen coverages are significantly greater on Pt(221) than either Pt(211) or Pt(111). For θ_O^{tot} 0.92 ML and below, the TPD features uniformly increase in intensity with exposure. For $\theta_{O_{2,ad}}$ up to 0.68 ML, $O_{2,ad}$ desorbs in two desorption peaks, a larger one near 140 K and a shoulder at 163 K. The higher temperature O_{ad} recombinative desorption peak at $\theta_{O_{ad}} = 0.24$ ML is broad with a sharp feature around 650 K. Once $\theta_{O_{ad}}$ reached 0.24 ML, sticking of O_2 at Ts = 100 K formed $O_{2,ad}$. However, once θ_O^{tot} reached 0.92 ML, a dramatic change in the relative amounts of O_{ad} and $O_{2,ad}$ was observed. Recombinative desorption suddenly increases in size at the expense of molecular desorption. The sharp peak seen at 650 K intensifies and the peak temperature shifts upward towards 680 K. Additionally, a peak sharpens at 647 K. The molecular desorption regime also shows a concomitant shift toward higher desorption temperatures, and a new peak grows in at 173 K. For the highest coverage studied, $\theta_O^{tot} = 1.08$ ML, desorption is evenly split over the molecular and recombinative regimes with $\theta_{O_{2,ad}} = \theta_{O_{ad}} = 0.54$ ML. This behavior is in marked contrast to what was observed on Pt(211) with (100) step geometry, and planar Pt(111). Whereas both Pt(111) and (211) reached a terminal surface coverage with similar exposures, the continued evolution of $O_{2,ad}$ and O_{ad} desorption features indicates the Pt(221) surface is not saturated. Further details can be found in figure S2 in the supporting information.

The partitioning of oxygen into O_{ad} and$O_{2,ad}$ with respect to θ_O^{tot} is shown in figure 7.4 for Pt(111), Pt(211), Pt(553), and Pt(221). Pt(553) and Pt(221) have (110) step geometry and the step geometry is (100) on Pt(211). Figure 4 shows how the total amount of oxygen adsorbed during O_2 exposures at = 100 K desorbs either molecularly or recombinatively during TPD. All coverages are expressed with respect to the TPD integral for $\theta_{O_{ad}} = 0.25$ ML on Pt(111). Although the angular desorption characteristics vary for different desorption peaks on Pt(111)[46], these effects are not significant in our measurements and do not

interfere with directly comparing the relative coverages of the different surface species, as demonstrated in the Supporting Information. In each of the four plots in figure 7.4, the solid lines are local fits to data while dotted lines indicate critical oxygen coverages. The gray areas in figures 7.4a and 7.4b indicate the highest obtained oxygen coverage on Pt(111) and Pt(211) under background dosing conditions. It is clear that Pt(111) and Pt(211), with (100) step geometry, have substantially lower saturation coverages than Pt(211) and Pt(553) surfaces with (110) step geometry. Neither Pt(221) nor (553) showed evidence of saturation in our TPD experiments and the abscissa are the limits of total coverage probed in our experiments.

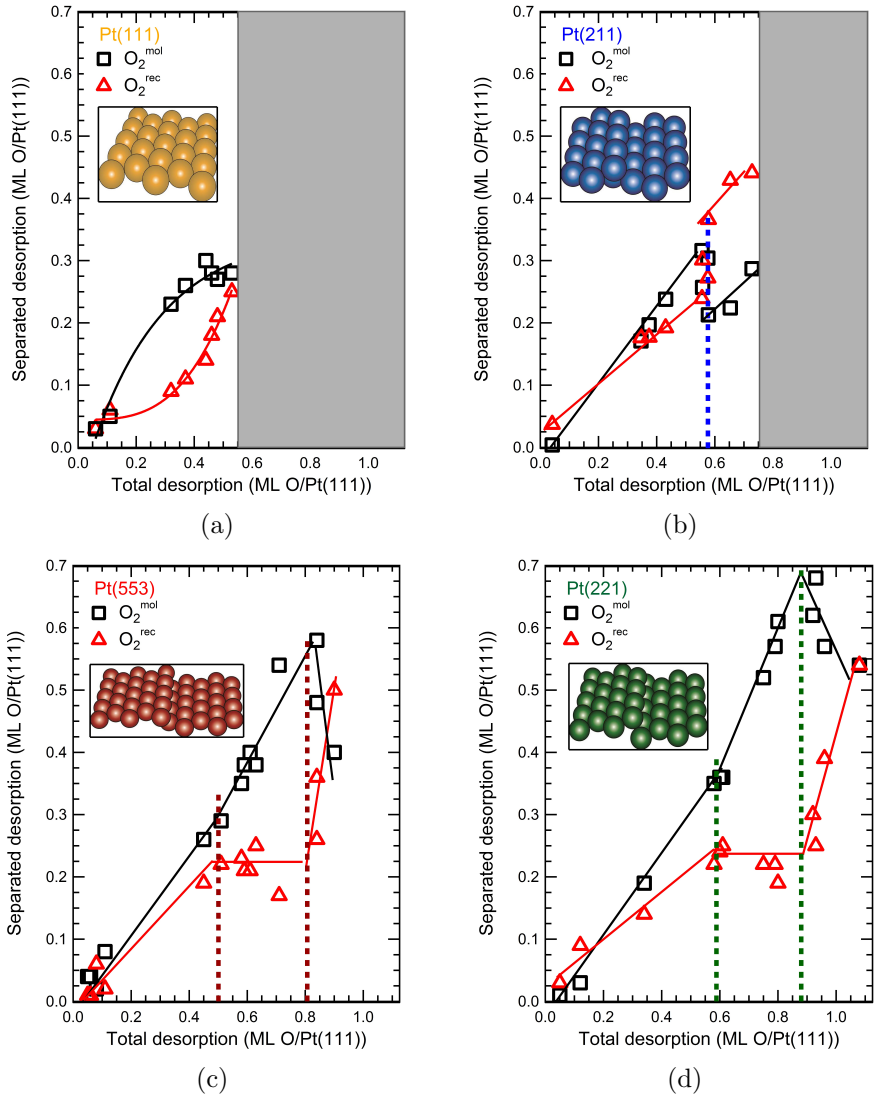

Figure 7.4: Integrated O_2 TPD signals for molecular and recombinative desorption as a function on initial O_2 coverage on a) Pt(111), b) Pt(211)[18], c) Pt(553) and d) Pt(221). The inset images show the surface representations and the solid lines are the fitted to the experimental data. The dotted lines emphasize the critical regions on the surfaces. The grey areas in figure 7.4a and figure 7.4b express the saturation coverage on Pt(111) and Pt(211).

We first consider the possible origins for the increase in O_2 uptake from planar

Pt(111) to the (100) stepped surfaces, which retain (111) atomic arrangements on the flat terraces. As discussed, O_2 adsorbs molecularly at 100 K on Pt(111), with a terminal $\theta_O^{tot} = 0.53$ ML. Dissociation only occurs during the temperature ramp, resulting in at most 0.25 ML O_{ad}, as shown by red triangles in figure 7.4a. It is important to note that dosing Pt(111) with O_2 at $T_s = 400$ K exclusively yields O_{ad} which saturates at $\theta_{O_{ad}} = 0.25$ ML. On Pt(211), saturation $\theta_{O_{ad}}$ is increased by 0.24 ML compared to Pt(111), representing a 45% increase in coverage. The number of Pt atoms per unit surface area is greater on corrugated Pt(211) than Pt(111). The ratio of geometric surface areas is 1.10, respectively, as described in detail in the Supporting Information. Now, if only $O_{2,ad}$ is packed on the Pt(211) surface at $T_s = 100$ K, then the packing density must be correspondingly higher on Pt(211) than on Pt(111), because of the increased surface area. This difference in geometric surface area accounts for, at most, 30% more $O_{2,ad}$ per unit area on Pt(211) than on Pt(111). Although attributing the increase in θ_O^{tot} exclusively to the changes in geometric surface is seemingly straightforward, it does not entirely account for the 45% increase observed. Low temperature dissociation of $O_{2,ad}$ could lead to the increase in θ_O^{tot}, but the differences are small enough that the observed uptake could be accounted for by the increased surface area.

Changes in the TPD spectra could indicate low temperature dissociation of $O_{2,ad}$. Lower $\theta_{O_{2,ad}}$ do not show any changes in the molecularly adsorbed O_2 TPD desorption features on Pt(211) (figure 7.3) up to $\theta_{O_{2,ad}} = 0.29$ ML. The absence of any changes in peak shapes suggests no coverage effects in the interactions between adsorbates. On Pt(211), the $O_{2,ad}$ molecular desorption peak is only 5 K lower than Pt(111), suggesting only small differences in the interadsorbate interactions. However, as θ_O^{tot} increases, the shifts in desorption features clearly shows changes in the interadsorbate interactions. For molecular desorption on Pt(211), the shift in intensity between the two desorption peaks, and the accompanying changes in the O_{ad} desorption features, point towards evolution in the nature of the surface. Although $\theta_{O_{2,ad}}$ does not increase very much, the $\theta_{O_{2,ad}}$ desorption peak shifts to 174 K. It is possible that these shifts are caused by the presence of atomic oxygen on the surface at low temperatures. As noted before, for Ts = 100 K O_2 exposures, dissociation of O_2 occurs during the TPD ramp, and above the $O_{2,ad}$ desorption temperature. Therefore, in order for O_{ad} to alter the interadsorbate interactions, it must dissociate at much lower temperatures than occurring for thermally induced dissociation on Pt(111). Although some dissociation may have occurred at the dosing temperature or early on in the ramp as a consequence of the combined presence of the (100) steps and a densely packed initial O_2 overlayer, we do not find that the changes on desorption peak temperature or θ_O^{tot} in our data to be particularly convincing to argue for or against dissociation at 100 K.

Alternatively, for the surfaces with (110) step geometry, the changes in the TPD spectra strongly indicate dissociative adsorption at 100 K. As shown in figure 7.4d, the changes in oxygen uptake on Pt(221) are far more pronounced. Not only does the desorption shift from single peak at 140 K to two peaks at 164 K and 173 K, but θ_O^{tot} increases by at least $\theta_O^{tot} = 0.50$ ML, an 85% increase from Pt(111). A similar increase is observed for Pt(553), shown in figure 7.4c. The increased number of adsorption sites because of the larger geometric surface area, while close for Pt(211), is far from sufficient to account for the increase in θ_O^{tot} on Pt(221). Pt(221) has a 16% larger geometric surface area that Pt(111), so in order to account for the 85% increase in oxygen coverage, a 60% increase in packing density of $O_{2,ad}$ would be required. This is not a plausible expectation because the majority of the surface is still regular (111) terraces. Formation of a second layer of $O_{2,ad}$ at 100 K is not supported by the TPD data; an overlayer would exhibit a significantly decreased desorption temperature[47, 48], which was not observed. As increases in geometric surface area, packing density, or overlayers are not adequate to account for the excess oxygen adsorption observed, low temperature dissociation of O_2 on (110) steps must be considered. Dissociation of $O_{2,ad}$ results in an overlayer consisting of $O_{2,ad}$ and O_{ad} covering the terraces and steps of the surface. This conclusion is supported by significant changes in the predominant $O_{2,ad}$ desorption peak. At $\theta_{O_{2,ad}} = 0.68$ ML, the peak desorption temperature is 20 K lower than on Pt(111); the temperature difference was only ≈ 5 K on Pt(211). A Redhead analysis of the larger difference for Pt(221) suggests a drop in desorption energy from the molecular state of 7.0 kJ mol^{-1}, when assuming a prefactor of 1x10^{-13} s^{-1}. Both Pt(221) and Pt(553) surfaces display similar O uptakes and distributions between molecular and recombinative desorption, suggesting the narrow step widths on Pt(221) are not the cause of the enhanced uptake. As the marked change in O uptake is more prominent going from Pt(211) to Pt(221), with similar step-widths and abundance of (111) terraces, it is the (110) step geometry that dissociates $O_{2,ad}$ and causes the increase in O uptake.

With the (110) surfaces inducing $O_{2,ad}$ dissociation at moderate to high coverages established, we now consider whether dissociation occurs for low θ_O^{tot}, i.e. along the initial increase in figure 7.4c and 7.4d. The plateau in both traces at $\theta_{O_{ad}} \approx 0.25$ ML supports the notion that this is indeed the case. For the lowest θ_O^{tot}, O_2 adsorption is evenly split between O_{ad} and $O_{2,ad}$. After this initial period of rapid O_2 dissociation, dissociation is self-limited to a maximum of 0.25 ML O/Pt. For θ_O^{tot} greater than ≈ 0.6 ML on Pt(221), or 0.5 ML for Pt(553), recombinative desorption plateaus while molecular desorption increases linearly for either surface. This suggests that the adsorption energy (E_{ads}) is independent of $\theta_{O_{2,ad}}$ in this coverage regime, and the chemical species present and surface

structures are invariant. However, we are unable to unambiguously attribute the increase in coverage to low-temperature $O_{2,ad}$ dissociation from the TPD results alone, because this argument holds true if dissociation for smaller initial coverages occurs between 100 K and 140 K. To resolve this issue, we must determine if O_{ad} is present on a Pt surface with (110) step geometry at 100 K.

The threshold behavior is the last point we wish to address regarding figure 7.4. Sudden additional dissociation at the expense of desorption occurs for both (110) and (100) stepped surfaces at $\theta_{O_{ad}} = 0.25$ ML. For both step types, the increase in dissociative adsorption is associated with an increase in the desorption temperature of $O_{2,ad}$ as well as the appearance of sharp desorption peaks in the recombinative desorption regime. The latter have been connected to formation of PtO_2 along the (110) steps, as shown in previous work on Pt(111)[13]. The formation of PtO_2 is also supported by the overlapping leading edges of the TPD features, which is characteristic of a phase transition. As O_2 has also been shown to bind more strongly on the metal oxide than the metal surface[22], we interpret the thresholds as the minimal $\theta_{O_{ad}}$ required for additional oxidation of the Pt surface, i.e. dissociation beyond regular dissociative adsorption on (111) terrace sites and step edges. Stabilizing interactions between $O_{2,ad}$ and the previously formed O_{ad} phase causes the temperature upshift for the molecular desorption feature occurring at the higher exposures. The increased binding leads to additional dissociation and formation of local metal oxides that decompose in the sharp desorption features in the recombinative regime, further supporting the formation of PtO_2. As previously argued for the (100) stepped surface, our data does not require the initial dissociation to occur at 100 K. However, dissociation must happen at all initial coverages somewhere between 100 K and 150 K. If it does not happen at 100 K, or at most to a small extent for the highest exposure, the limited total uptake for (211) makes sense. Most dissociation only occurs during the temperature ramp, leading to significant loss of O_2 through parallel molecular desorption and prior to the onset of local surface metal oxide formation. As initial dissociation is better facilitated by the (110) step at 100 K, more O_2 binds at a lower temperature, in part as a 0.25 ML O_{ad}. With a minimal additional concentration of $O_{2,ad}$ that spans the plateau, molecular adsorption locations and/or geometries are present that facilitate local formation of a surface metal oxide.

Our TPD results clearly indicate that O_2 dissociation depends strongly on the step geometry at low temperatures. In the supporting information, we present an alternate means to support this point. Whereas we could not conclude this with any certainty for Pt(211), both (110) stepped surfaces dissociate molecular oxygen, at least for higher coverages, at 100 K. For lower initial coverages, we

could not argue this based on TPD results, although the coverage-dependencies seem to suggest it. In order to resolve this we have taken images of the Pt(553) surface using STM in the Chicago laboratory.

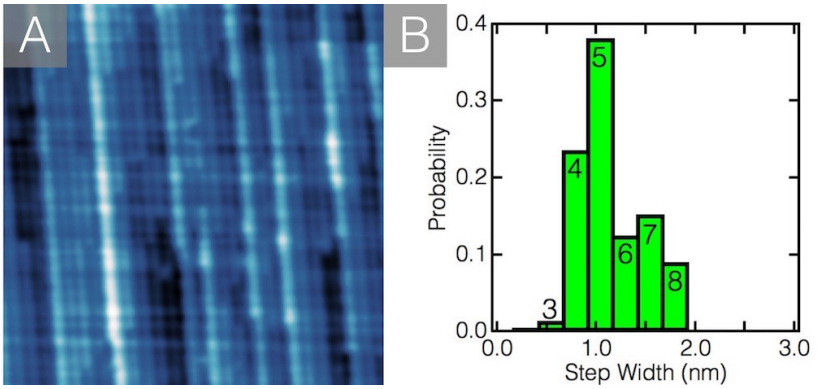

Figure 7.5: The left panel (A) shows an STM image of the clean Pt(553), T_{STM} = 30 K, V = 1.0 V, I = 250 pA, 40 nm x 40 nm. The statistical analysis of the step width Pt(553) leads to the histogram shown in the right panel (B).

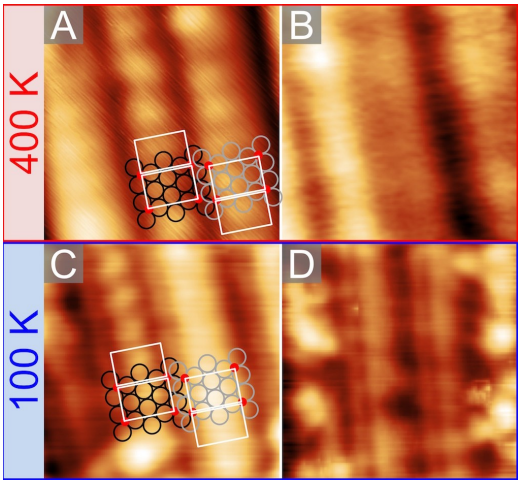

Figure 7.6: 4nm x 4 nm STM images of oxygen covered Pt(553) taken at T_{STM} = 30 K. A) 3 L O_2 exposure at 400 K, V = 0.92 V, I = 160 pA, B) 0.6 L O_2 exposure at 400 K, V = 0.70 V, I = 150 pA, C) 2 L O_2 exposure at 100 K, V = 0.15 V, I = 90 pA, D) 0.6 L O_2 exposure at 100 K, V = 0.78 V, I = 190 pA.

In order to obtain a reliable standard for the structure of Pt(553), we first

imaged the clean Pt(553) surface. A typical image is shown figure 7.5A. Due to surface relaxation and slight misalignment during the crystal preparation process, the surface is not uniformly comprised of five atom wide (111) terraces separated by monotonic steps. While the LEED pattern corresponding to Pt(553) has a spot-splitting to row-spacing ratio that indicates an average terrace width of five atoms, describing this surface as Pt[5(111)x(111)] which is equivalent to Pt[4(111)x(110)], the sub-nanometer scale resolution of STM shown in figure 7.5A allows us to determine the actual distribution of terraces widths. Figure 5B shows this distribution of terrace widths in the form of a histogram. Over 60% of the steps are either 5 or 4 atoms wide with the 5-atom wide terraces being the most abundant. This distribution of terrace widths allows us to study O adsorption on a (110) step type surface with known terrace variances; knowing that there is a distribution of terrace widths allows us to relate adsorption behavior to step type rather than terrace width. It is also important to note the variance in contrast across the clean metal surface. As has been shown when imaging other stepped metal surfaces, the high corrugation of the surface, coupled with inherent imaging limitations, causes steps to display with varying contrast in the STM image[38, 49, 50].

O_{ad} is the only oxygen species after O_2 exposure at 400 K, so the Pt(553) crystal was exposed to 3 L of O_2 at Ts = 400 K to provide a reference image for $\theta_{O_{ad}} = 0.25$ ML and no $O_{2,ad}$. After exposure, the sample was transferred to the STM and cooled to 30 K for imaging. Figure 7.6A shows an image of the oxidized surface along with an illustration of the positions of oxygen and Pt atoms. The oblong rectangular features present in figure 7.6A are highlighted with a white rectangle and correspond to four oxygen atoms resting in fcc tetragonal hollow sites; the arrangement of oxygen on Pt(553) has been determined by previous work[44]. As molecularly adsorbed oxygen is not stable at the 400 K exposure temperature[8], the oblong features must result from the presence of O_{ad}. As seen in figure 7.6A, each of the three terraces imaged possess the rectangular features. The terrace on the left hand side is slightly wider than the two remaining terraces. Despite the difference in terrace width, the appearance of the step in the image is the same. The step terrace has the same rectangular feature characteristic of four O_{ad} on a (111) terrace. We also imaged the surface after exposure to 0.6 L O_2 at $T_s = 400$ K to determine if the surface structure is coverage dependent. As shown in figure 7.6B, the surface is now mostly clean terraces with bright features aligning along the step edges instead of the rectangular features spanning the steps. The orientation of the images is such that the steps move downward from right to left across all four images. The location of the bright oxygen features along the edge of the step, with a slight dark region behind the bright feature,

suggests that the oxygen is also aligning in the tetragonal hollows of the fcc surface at low coverages.

We now look at the Pt(553) surface after low temperature exposures to O_2 to determine if the features characteristic of O_{ad} are present, indicating low temperature dissociation of $O_{2,ad}$ on (110) stepped surfaces. The Pt(553) surface was exposed to 2 L O_2 ($\theta_O^{tot} \approx 0.7$ ML) at $T_s = 100$ K, and the STM images are shown in figure 7.6C. At this temperature, T_s is too low to activate dissociation, and $O_{2,ad}$ is most stable on (111) terraces[8]. If $O_{2,ad}$ does not, in fact, dissociate, we would not expect to see the surface uniformly covered by the rectangular features identified in figure 7.6A. This is clearly not the case. As shown in figure 7.6C, the Pt(553) surface after $T_s = 100$ K exposure to O_2 is very similar to the surface after 400 K O_2 exposure. This suggests that $O_{2,ad}$ dissociated, forming O_{ad} on the terraces. This is shown in figure 7.6C as the presence of rectangular features along the center-left terrace while the center-right terrace appears to be covered in uniformly bright adsorbates. Post-imaging TPD of the sample confirms that no appreciable accumulation of contaminants occurs during imaging, so the bright, rectangular features must be O_{ad}. The coexistence of O_{ad} and $O_{2,ad}$ accurately represents TPD data which indicates the presence of both oxygen species. Because the sample was exposed to O_2 at 100 K, below the temperature needed for dissociation of oxygen on Pt(553), the oxygen must dissociate upon adsorption to the surface. This cannot be because of the direct channel for dissociation, because the translational energy of the incident O_2 is insufficient to activate dissociation[8]. To check for coverage effects, the Pt(553) surface was also exposed to 0.6 L ($\theta_O^{tot} \approx$ 0.2 ML) at 100 K. A representative STM image is shown in figure 7.6D. Although the exposure is the same as for the image in figure 7.6B, the structures along the terraces after the 100 K exposure well-resolved. Rather than oblong rectangular features, a striped pattern near the step edge presents itself. The orientation of the dark contrast in figure 7.6D corresponds well to the dark contrast near the bright feature along the step edge in figure 7.6B. The presence of similar structural features for 0.6 L O_2 exposure at 100 K and 400 K shows that O_2 dissociation occurs at 100 K even for very low O_2 coverages. Finally, the actual terrace widths on the Pt(553) crystal are not uniform (see figure 7.5B), so it can be determined that the dissociation observed at low temperatures on Pt(553) is due to the (110) step geometry rather than the terrace width. The STM images clearly support the findings from the TPD experiments. This demonstrates that the height of dissociation barriers is sensitive to step geometry.

Summarizing, (100) stepped Pt surfaces exhibit high reactivity at lower oxygen coverages (≈ 0.6 ML), however, the reactivity decreases with increasing coverage. On the other hand, (110) stepped Pt surfaces require more oxygen to achieve the

high reactivity but they maintain the high reactivity up to higher coverages (> 0.8 ML). Additionally, extended O_2 exposures saturated the (100) stepped surfaces whereas on the (110) steps, no such saturation was observed.

7.5 Conclusion

Our results show low-temperature dissociation of O_2 on Pt surfaces is strongly dependent on the arrangement of Pt atoms on monoatomic steps. This demonstrates the complexities of O_2 adsorption behavior that arise when defect sites are accounted for on catalytically active surfaces. A combination of TPD and STM experiments show that (100) and (110) step types have very different adsorption and desorption behaviors. Although surfaces with (100) steps show an increase in oxygen coverage compared to Pt(111), this can be attributed to the increased areal density of Pt atoms on the corrugated surfaces. However, on surfaces with (110) step geometries, this increase in surface area cannot account for the increased oxygen coverage. STM images after exposures of Pt(553) to O_2 at $T_s = 400$ K or 100 K clearly show similar surface structures. Only O_{ad} can be on the surface after $T_s = 400$ K O_2 exposures; because the surface structures are similar, O_{ad} must also be present after $T_s = 100$ K O_2 exposures. Therefore, O_2 dissociates upon adsorption on surfaces with (110) steps and not only during the TPD ramp. The presence of O_{ad} confirms that O_2 dissociation at low temperatures causes the increased oxygen uptake. This demonstrates that step geometry is the determining factor in low temperature O_2 dissociation. The (110) steps must lower the dissociation barrier in ways steps with (100) geometry cannot.

7.6 Bibliography

References

(1) Zambelli, T; Barth, J. V.; Wintterlin, J; Ertl, G *Nature* **1997**, *390*, 495–497.

(2) Bonn, M. *Science* **1999**, *285*, 1042–1045.

(3) Sutter, E. a.; Tong, X.; Jungjohann, K.; Sutter, P. W. *Proceedings of the National Academy of Sciences of the United States of America* **2013**, *110*, 10519–24.

(4) Gustafson, J.; Mikkelsen, A; Borg, M.; Andersen, J.; Lundgren, E.; Klein, C.; Hofer, W.; Schmid, M.; Varga, P.; Köhler, L.; Kresse, G.; Kasper, N.; Stierle, A.; Dosch, H. *Physical Review B* **2005**, *71*, 115442.

(5) Wintterlin, J. *Science* **1997**, *278*, 1931–1934.

(6) Hawkins, J. M.; Weaver, J. F.; Asthagiri, A. *Physical Review B* **2009**, *79*, 125434.

(7) Bradley Shumbera, R.; Kan, H. H.; Weaver, J. F. *Surface Science* **2007**, *601*, 4809–4816.

(8) Luntz, A. C.; Williams, M. D.; Bethune, D. S. *Journal of Chemical Physics* **1988**, *89*, 4381–4396.

(9) Nolan, P.; Lutz, B.; Tanaka, P.; Davis, J.; Mullins, C. *The Journal of chemical physics* **1999**, *111*, 3696–3704.

(10) Stipe, B.; Rezaei, M.; Ho, W; Gao, S; Persson, M; Lundqvist, B. *Physical review letters* **1997**, *78*, 4410.

(11) Winkler, A.; Guo, X.; Siddiqui, H. R.; Hagans, P.; Yates, J. T. *Surface Science* **1988**, *201*, 419–443.

(12) Wang, H; Tobin, R. G.; Lambert, D. K.; DiMaggio, C. L.; Fisher, G. B. *Surface Science* **1997**, *372*, 267–278.

(13) Devarajan, S. P.; Hinojosa Jr., J. A.; Weaver, J. F. *Surface Science* **2008**, *602*, 3116–3124.

(14) Gland, J. L.; Sexton, B. A.; Fisher, G. B. *Surface Science* **1980**, *95*, 587–602.

(15) Steininger, H; Lehwald, S; Ibach, H *Surface Science* **1982**, *123*, 1–17.

(16) Weaver, J. F.; Chen, J. J.; Gerrard, A. L. *Surface Science* **2005**, *592*, 83–103.

(17) Weaver, J. F.; Kan, H. H.; Shumbera, R. B. *Journal of Physics-Condensed Matter* **2008**, *20*.

(18) Badan, C.; Koper, M. T. M.; Juurlink, L. B. F. *The Journal of Physical Chemistry C* **2015**, *119*, 13551–13560.

(19) Van der Niet, M. J. T. C.; den Dunnen, A.; Juurlink, L. B. F.; Koper, M. T. M. *Journal of Chemical Physics* **2010**, *132*, 174705–174713.

(20) Van der Niet, M. J. T. C.; den Dunnen, A.; Juurlink, L. B. F.; Koper, M. T. M. *Physical Chemistry Chemical Physics* **2011**, *13*, 1629–1638.

(21) Van der Niet, M. J. T. C.; den Dunnen, A.; Juurlink, L. B. F.; Koper, M. T. M. *Angewandte Chemie-International Edition* **2010**, *49*, 6572–6575.

(22) Wang, J. G.; Li, W. X.; Borg, M.; Gustafson, J.; Mikkelsen, a.; Pedersen, T. M.; Lundgren, E.; Weissenrieder, J.; Klikovits, J.; Schmid, M.; Hammer, B.; Andersen, J. N. *Physical Review Letters* **2005**, *95*, 1–4.

(23) Parker, D. H.; Bartram, M. E.; Koel, B. E. *Surface Science* **1989**, *217*, 489–510.

(24) Saliba, N.; Tsai, Y.-L; Panja, C; Koel, B. *Surface Science* **1999**, *419*, 79–88.

(25) Ohno, Y.; Matsushima, T. *Surface Science* **1991**, *241*, 47–53.

(26) Zhu, T.; Sun, S.-G.; van Santen, R. A.; Hensen, E. J. *The Journal of Physical Chemistry C* **2013**, *117*, 11251–11257.

(27) Li, W.; Österlund, L.; Vestergaard, E.; Vang, R.; Matthiesen, J; Pedersen, T.; Lægsgaard, E.; Hammer, B; Besenbacher, F *Physical Review Letters* **2004**, *93*, 146104.

(28) Walker, A.; Klötzer, B; King, D. *The Journal of chemical physics* **1998**, *109*, 6879–6888.

(29) Gambardella, P; Sljivancanin, Z; Hammer, B; Blanc, M; Kuhnke, K; Kern, K *Physical Review Letters* **2001**, *87*.

(30) Kratzer, P.; Pehlke, E.; Scheffler, M.; Raschke, M. B.; Hofer, U. **1998**, 5.

(31) Šljivan, Ž.; Hammer, B. *Physical Review B* **2010**, 1–4.

(32) Badan, C.; Heyrich, Y.; Koper, M. T. M.; Juurlink, L. B. F. *The Journal of Physical Chemistry Letters* **2016**, 1682–1685.

(33) Vanhove, M. A.; Somorjai, G. A. *Surface Science* **1980**, *92*, 489–518.

(34) Henzler, M *Surface Science* **1970**, *19*, 159–171.

(35) Puglia, C.; Nilsson, a.; Hernnäs, B.; Karis, O.; Bennich, P.; Mårtensson, N. *Surface Science* **1995**, *342*, 119–133.

(36) Norton, P.; Davies, J.; Jackman, T. *Surface Science* **1982**, *122*, L593–L600.

(37) Derouin, J.; Farber, R. G.; Killelea, D. R. *Journal of Physical Chemistry C* **2015**, *119*, 14748–14755.

(38) Kolb, M. J.; Farber, R. G.; Derouin, J.; Badan, C.; Calle-Vallejo, F.; Juurlink, L. B. F.; Killelea, D. R.; Koper, M. T. M. *Physical Review Letters* **2016**, *116*, 136101.

(39) Bashlakov, D.; Juurlink, L.; Koper, M.; Yanson, A. *Catalysis Letters* **2012**, *142*, 1–6.

(40) Avery, N. R. *Chemical Physics Letters* **1983**, *96*, 371–373.

(41) Rar, A.; Matsushima, T. *Surface Science* **1994**, *318*, 89–96.

(42) Gee, A. T.; Hayden, B. E. *The Journal of Chemical Physics* **2000**, *113*, 10333–10343.

(43) Ogawa, T.; Kuwabara, A.; Fisher, C. A. J.; Moriwake, H.; Miwa, T. *Journal of Physical Chemistry C* **2013**, *117*, 9772–9778.

(44) Kolb, M. J.; Calle-Vallejo, F.; Juurlink, L. B. F.; Koper, M. T. M. *The Journal of chemical physics* **2014**, *140*, 134708.

(45) Feibelman, P.; Esch, S.; Michely, T. *Physical Review Letters* **1996**, *77*, 2257–2260.

(46) Allers, K.-H.; Pfnür, H; Feulner, P; Menzel, D *Zeitschrift für Physikalische Chemie* **1996**, *197*, 253–268.

(47) Gibson, K.; Sibener, S.; Hall, B. M.; Mills, D.; Black, J. *The Journal of Chemical Physics* **1985**, *83*, 4256–4270.

(48) Kimmel, G. A.; Persson, M.; Dohnalek, Z.; Kay, B. D. *The Journal of Chemical Physics* **2003**, *119*, 6776–6783.

(49) Ding, H.; Stepanyuk, V.; Ignatiev, P.; Negulyaev, N.; Niebergall, L; Wasniowska, M; Gao, C.; Bruno, P; Kirschner, J *Physical Review B* **2007**, *76*, 033409.

(50) Pearl, T.; Sibener, S. *The Journal of Physical Chemistry B* **2001**, *105*, 6300–6306.

Chapter 8

Summary

8.1 Summary

Interactions of molecules with solid catalytic surfaces are of great importance to our daily lives. Nowadays, most large scale chemical productions in industry involve heterogeneous catalysis in different forms. In particular, the energy sector is highly dependent on heterogeneous catalysis as a future solution to end our dependency on natural sources lies in generating hydrogen by splitting water. Several transition metals, such as Pt, are known to be good catalyst materials for water splitting reactions. They play a key role in understanding the fundamental aspects of the elementary interactions occurring on the surfaces of catalysts. These surfaces, however, are generally very complex and contain a wide distribution of structurally and chemically different sites with different activities. One of the key issues in optimizing the activity of the catalysts is to distinguish and specify the active sites on the surface. In this thesis we use highly corrugated Pt surfaces and UHV techniques (TPD, LEED, and STM) to explore the effects of surface defects on adsorption and desorption of water and related adsorbates.

Prototypical surface science and gas-metal studies for heterogeneous catalysts involve small molecules (e.g. H_2, O_2, and H_2O) as they represent dissociative (H_2 and O_2) and non-dissociative (H_2O) adsorption. The (211) surface, with the smallest unit cell containing the (100) step type, is often taken as the reference for (100) step edge effects in theoretical studies. In chapter 4, we have investigated to what extent Pt(211) is representative for Pt[n(111)x(100)] surfaces in adsorption/desorption behavior of water, hydrogen, and oxygen through temperature programmed desorption. We have compared our results with other Pt surfaces with the same step type but wider terraces and found significant differences. For water adsorption to Pt(211), water molecules tends to gather around the steps due

to the short distance between step edges. It forms crystalline ice at temperatures where on Pt(533) amorphous solid water (ASW) forms. For hydrogen, recombinative desorption from the (100) step edge seems not influenced by the width of the neighboring terraces. However, our results showed that wider terraces cause a large variation in the binding energy and give rise to a broader desorption feature. We have also shown that O_2 dissociation is significantly affected by terrace width. By comparison to Pt(533), we observed enhanced dissociation on Pt(211) resulting in up to 50 % larger maximum O coverage. Our results stressed that great caution is necessary when extrapolating results from theoretical studies on the smallest unit cell to larger structures.

For water adsorption on Pt surfaces, the general consensus is that H_2O water adsorbs molecularly at all coverages and exposures below 120 K leads to the formation of metastable ASW. The amorphous phase crystallizes into crystalline ice when heated. For studies of ASW, CI, and the kinetics of the phase transition, the atomically flat Pt(111) plane has often been used. In chapter 5, we have studied the role of the surface corrugation on crystallization using three-atom wide (111) terraces truncated by (100) and (110) steps. These surfaces have step densities similar to actual nanoparticles. Our results showed that the step type significantly influences the wetting behavior of H_2O_{ad} resulting in different desorption kinetics for ASW and CI. Also, crystallinity of the CI-like layers is maintained over a thickness that is dictated by step type.

The hydrogen evolution reaction is one of the key reactions in electrochemistry. This reaction requires a deep understanding of the interactions between water, adsorbed hydrogen and the electrode surface, with platinum being one of the most studied metals. In chapter 6, we have investigated the influences of pre- and post-covered deuterium on water desorption from Pt(211). For post-deuterated surface, D_{ad} lowers the binding energy of water at $\theta_{H_2O} < 1.0$ ML. Similar to other Pt[n(111)x(100)] surfaces with n=4, 6, and 8, Pt(211) also exhibits hydrophobic behavior when D is preadsorbed. Both co-adsorption experiments yield the maximum isotopic ratio at sub-monolayer water coverages. The desorption kinetics and the water structure does not seem to be affected by subsequent exposure to D_2. However, for the pre-deuterated surface our kinetic analysis suggests a new CI phase. This new phase has identical desorption kinetics with the CI grown on Pt(111). Finally, we introduced a new method to quantify the (110) step defects on (100) stepped surfaces. This method can be especially useful when inspecting the surface quality of the real crystals used in ultra-high vacuum studies.

One of the vital issues in heterogeneous catalysis is how the role of metaloxide interfaces influences the catalytic activity. A smart construction of nanocatalysts can advance the catalytic activity of transition metals. In chapter 7, we reported

a combined TPD and STM study of oxygen adsorption and dissociation to investigate the extent to which step geometry influences oxygen dissociation on Pt surfaces. Our quantitative TPD results show that (110) stepped surfaces build up a considerably larger surface oxygen concentration in comparison to (100) stepped surfaces and Pt(111) for adsorption at 100 K. STM images for different coverages and surface temperatures confirm the terrace-width indiscriminate lowering of the dissociation barrier by the (110) step type.

8.2 Samenvatting

De interactie van moleculen met katalytisch actieve oppervlakken zijn erg belangrijk in het dagelijks leven. Grootschalige productie van chemicaliën gebeurt tegenwoordig bijna altijd met behulp van heterogene katalyse. Dit geldt in het bijzonder voor de energiesector, welke sterk afhangt van heterogene katalyse. In heterogene katalyse vinden wij namelijk de toekomstige oplossing voor onze afhankelijkheid van fossiele brandstoffen; de productie van elementair waterstof en zuurstof uit water. Verschillende overgangsmetalen, zoals bijvoorbeeld Pt, staan bekend als goede katalytisch actieve materialen voor de dissociatie van water en deze materialen spelen daarom een belangrijke rol in het fundamentele begrip van elementaire reacties aan katalytisch actieve oppervlakken. Deze oppervlakken zijn echter erg complex en bevatten een grote distributie aan structurele en chemisch verschillende sites welke allen een verschillende activiteit kunnen hebben. Eén van de uitdagingen bij het optimaliseren van de activiteit van katalysatoren is het onderscheiden en identificeren van actieve sites. In dit proefschrift gebruiken we sterk gecorrugeerde Pt oppervlakken en ultrahoog vacuüm (UHV) technieken (TPD, LEED, en STM) om de invloed van oppervlakte defecten op adsorptie en desorptie van water en water-gerelateerde adsorbaten te bestuderen.

Prototypische gas-metaal en oppervlakte-onderzoek van heterogene katalysatoren worden doorgaans uitgevoerd met kleine moleculen (e.g. H_2, O_2, en H_2O) omdat ze dissociatieve (H_2 en O_2) en niet-dissociatieve (H_2O) adsorptie representeren. Het (211) oppervlak, de kleinste eenheidscel met het (100) staptype, wordt vaak gebruikt in theoretisch onderzoek als referentie voor het effect van (100) stapranden. In hoofdstuk 4 hebben we met behulp van temperatuur geprogrammeerde desorptie (TPD) onderzocht in hoeverre Pt(211) representatief is voor Pt[n(111)x(100)] oppervlakken in het adsorptie/desorptie gedrag van water, waterstof, en zuurstof. Daarnaast hebben we onze resultaten vergeleken met andere Pt oppervlakken met hetzelfde staptype maar bredere terrassen, en significante verschillen gevonden. Bij water adsorptie aan Pt(211) neigt water ertoe rond de stapranden te groeperen als gevolg van de korte afstand tussen de stapranden. Het vormt daarbij de kristallijn ijs structuur, in tegenstelling tot Pt(533) waar het amorf vast water (ASW) vormt. Bij waterstof lijkt het alsof de recombinatieve desorptie niet beïnvloed wordt door de breedte van de naburige terrassen. Onze resultaten tonen echter wel aan dat bredere terrassen een grote variatie in de bindingsenergie veroorzaaken, wat resulteert in een bredere desorptie piek. Ook hebben we laten zien dat O_2 dissociatie sterk benvloed wordt door de breedte van het terras. Wanneer we Pt(211) vergelijken met Pt(533) zien we dat dissociatie bevorderd wordt met als gevolg een 50 % hogere O bedekkingsgraad. Onze resultaten tonen daarmee aan dat men voorzichtig moet zijn bij de extrapolatie

van resultaten van theoretisch onderzoek aan kleine eenheidscellen naar grotere structuren.

De waterstof-evolutie-reactie is één van de meest belangrijke reacties binnen de elektrochemie. Deze reactie vereist begrip van de interacties tussen water, geadsorbeerd waterstof, en het oppervlak van de elektrode, waarvan platina het meest bestudeerde metaal van is. In hoofdstuk 6 hebben we bestudeerd hoe deuterium adsorptie voor of na water adsorptie de opvolgende water desorptie benvloed. Dit is bestudeerd door middel van desorptie experimenten aan Pt(211). Bij het naderhand gedeutereerde oppervlak verlaagt D_{ad} de bindingsenergie van water bij $\theta_{H_2O} < 1{,}0$ monolagen. Vergelijkbaar met andere Pt[n(111)x(100)] oppervlakken, waar n = 4, 6, en 8, vertoont Pt(211) ook hydrofoob gedrag wanneer D vooraf geadsorbeerd wordt. Beide co-adsorptie experimenten resulteren in een maximale isotoop verhouding bij een submonolaag bedekkingsgraad van water. Bij het vooraf gedeutereerde oppervlak suggereert onze kinetische analyse echter een nieuwe kristallijn ijs fase. Deze nieuwe fase heeft identieke desorptie kinetiek als kristallijn ijs dat op Pt(111) is gegroeid. Ten slotte introduceerden we een nieuwe methode om de (110) stapranden te kwantificeren aan (100) gestapte oppervlakken. Deze methode is in het bijzonder nuttig om de kwaliteit van het oppervlak vast te stellen bij onderzoek aan echte kristallen onder UHV.

Eén van de belangrijkste problemen binnen de heterogene katalyse is de invloed van metaaloxiden op de katalytische activiteit. Een intelligente constructie van nano-katalysatoren kan zorgen voor vooruitgang in de katalytische activiteit van overgangsmetalen. In hoofdstuk 7 rapporteren we een gecombineerde TPD en raster tunnel microscopie (STM) studie van zuurstof adsorptie en dissociatie. We hebben bestudeerd in hoeverre de geometrie van stapranden zuurstof dissociatie aan Pt oppervlakken beïnvloedt. Onze kwantitatieve TPD resultaten tonen aan dat oppervlakken met (110) stapranden significant hogere zuurstof concentraties opbouwen in verhouding tot (100) stapranden wanneer zuurstof bij 100 K geadsorbeerd wordt. STM plaatjes met verschillende bedekkingsgraad en oppervlakte temperatuur bevestigen de terrasbreedte onafhankelijkheid van de dissociatiebarrière bij (110) type stapranden.

Appendix

Appendix A

Supporting information to Chapter 7

Figure S1 shows oxygen desorbing from Pt(111), Pt(211), Pt(221) and Pt(553). Desorption between 500 and 850 K results from recombinative desorption. Several studies[1, 2], reported that oxygen saturates at 0.25 ML in the recombinative desorption region on Pt(111). The hatched area corresponds to our best estimate for θ_O= 0.25 ML on Pt(111) and serves as our reference for subsequent TPD experiments.

In figure S2, we show the uptake curves of oxygen for Pt(111), Pt(211), Pt(221), Pt(533), and Pt(553). The uptake curve includes total amount O_2 desorption from the molecular and recombinative desorption regimes. For Pt(111), the saturation coverage is in good agreement with previous work done by Steininger et al.[1] (black squares). For combined molecular and recombinative desorption, the highest coverage obtained on Pt(111) is 0.53 ML. Figure S2 clearly shows that stepped surfaces exhibit significantly higher oxygen coverages.

To emphasize the different effects that the two step types have on the adsorption of oxygen on Pt surfaces, we show in figure S3 how the fraction of O_{ad} changes as a function of total O_2 coverage. For Pt(221) and (553), the fraction of O_{ad} drops to ∼25% between $\theta_O^{tot} \approx 0.6$ and 0.90 ML, and increases to ∼55% for $\theta_O^{tot} > 0.90$ ML. The O_{ad} desorption decrease between 0.6 ML and 0.90 ML results in a marked change in the ratio between $O_{2,ad}$ and O_{ad} desorption.

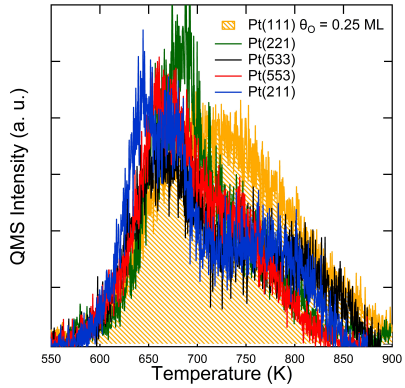

Figure S1: O_2 TPD spectra for Pt(111), Pt(211), Pt(221), Pt(533) and Pt(553).

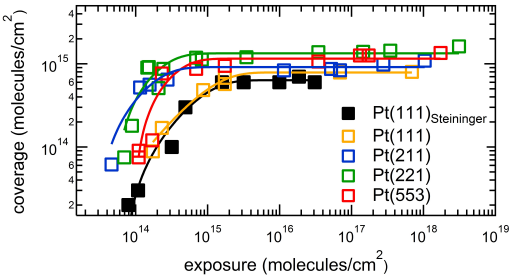

Figure S2: O_2 desorption from Pt(111), Pt(211), Pt(221) and Pt(553). Black squares show experimental data obtained by Steininger et al.[1]

Figure S4 shows TPD spectra of O2 desorption taken at different angles from the Pt(553) surface for 2.2 L O2 exposures at 100 K. Because of geometric constraints of the instrument, the angular variation is ±12°. This is because the crystal is mounted off center from the rotational axis of the x, y, z, θ manipulator, and x,y, position is limited to ±12/5 mm. The crystal-to-orifice distance was aligned by eye, causing some variation in the absolute peak intensity. However, the relative intensities of the low (molecular) and high (recombinative desorption) desorption peaks would indicate biases in the desorption angles for the two processes. As shown in table A.1, only small variations in the percent of recombinative desorption versus total O_2 desorption is observed, indicating that the angular dependencies do not vary enough between the low and high temperature desorption features to affect the interpretation of our data in the manuscript.

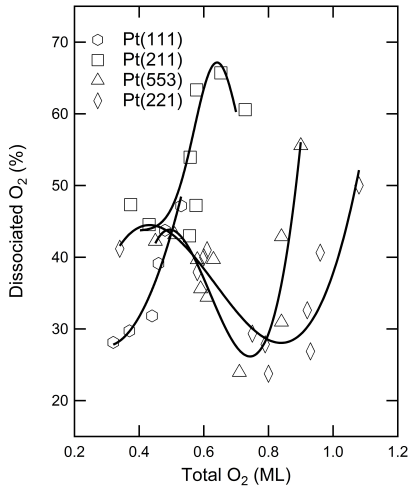

Figure S3: Fraction of adsorbed O_2 dissociated for Pt(111), Pt(211), Pt(221) and Pt(553) vs. θ_O. The lines through the data are to guide the eye.

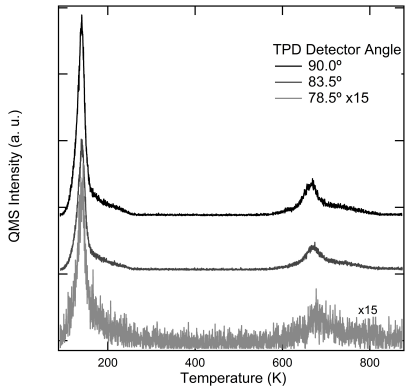

Figure S4: Angle-resolved TPD of O_2 desorbing from Pt(553). For each, the initial O/O_2 coverages were the same. Dose conditions: 2.2 L O_2, T_s = 100 K.

Because of their corrugation, stepped surfaces have higher actual geometric surface area than planar (111) surfaces[3]. In figure S5, we show a typical packing arrangement of the fcc unit cell, where α = lattice constant. The planes "x+y" show the actual geometric area of a stepped surface. For (100) and (110) stepped Pt(111) surfaces $\alpha = 125.4°$ and 109.5°, respectively. The ratio of the geometric surface area of (211)/(111) and (533)/(111) is ∼1.10. For (221)/(111) and (553)/(111), it is slightly higher, ∼1.15.

Table A.1: Percentage of total O2 from recombinative desorption for three different TPD angles.

Angle	% Recombinative
78.5	26
83.5	31
90.0	30

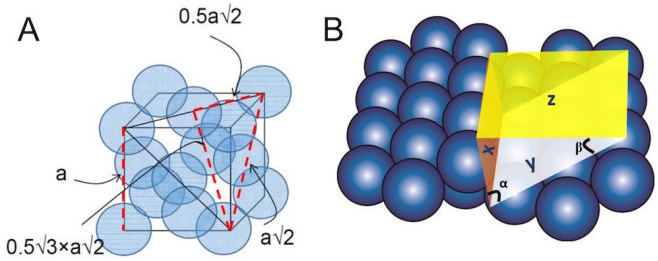

Figure S5: A) The packing arrangement of the face centered cubic (fcc) cell. B) (x+y) planes show the actual geometric area of a stepped Pt(211) surface. α is the angle between (111) and (100) planes and β is the angle between the (211) and (111) planes.

Figure S6A shows a representative STM image of an oxidized Pt(553) surface (figure 7.6 in main manuscript) and its corresponding line profile (figure S6B). This serves to illustrate the topography of the surface.

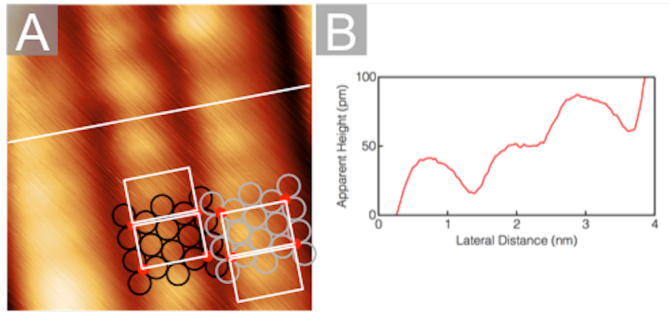

Figure S6: A) STM image from chapter 7 figure 7.6A with a profile line (white) drawn across oxidized terraces B) Extracted line profile from image.

List of Publications

- Badan, C.; Farber, R.; Heyrich, Y.; Koper, M.T.M.; Killelea, D.R. and Juurlink, L.B.F. : *Step-Type Selective Oxidation of Pt Surfaces*, Journal of Physical Chemistry C, 2016

- Badan, C.; Heyrich, Y.; Koper, M.T.M. and Juurlink, L.B.F. : *Surface Structure Dependence in Desorption and Crystallization of Thin Interfacial Water Films on Platinum*, The Journal of Physical Chemistry Letters, 2016, 7, 1682

- Kolb, M.J.; Farber, R.; Derouin, J.; Badan, C.; Calle-Vallejo, F.; Juurlink, L.B.F.; Killelea, D.R. and Koper, M.T.M.: *Double Stranded Water on Stepped Platinum Surfaces*, Phys. Rev. Lett., 2016, 116, 136101

- Badan, C.; Koper, M.T.M. and Juurlink, L.B.F. : *How Well Does Pt(211) Represent Pt[n(111) × (100)] Surfaces in Adsorption/Desorption?*, The Journal of Physical Chemistry C, 2015, 119, 13551

- den Dunnen, A.; van der Niet, M.J.T,C.; Badan, C.; Koper, M.T.M. and Juurlink, L.B.F. : *Long-Range Influence of Steps on Water Adsorption on Clean and D-Covered Pt Surfaces*, Physical Chemistry Chemical Physics, 2015, 17, 8530

- Badan, C.; Esenturk, O. and Yilmaz, A. : *Microwave-Assisted Synthesis of Eu^{3+} Doped Lanthanum Orthoborates, Their Characterizations and Luminescent Properties*, Solid State Sciences, 2012, 14, 1710

Curriculum Vitae

Cansın Badan was born on January 30$^{\text{th}}$, 1987 in Çukurova, Turkey. After finishing the *Anatolian High School*, he studied Chemistry at the Middle East Technical University, METU. In 2008, he did an internship in the group of Prof. J.W. (Hans) Niemantsverdriet at the Eindhoven University of Technology. In 2009, he moved to Netherlands for another internship at Leiden University under the supervision of Dr. Ludo Juurlink, studying "Water desorption from Pt(755) and its dependence on precoverage by hydrogen". During his undergraduate studies, he was awarded the Vehbi Koç Scholarship. In 2011, he earned his bachelor's degree with a research thesis on polymer composites.

Cansın continued at METU for his master's degree in inorganic chemistry under the supervision of Dr. Okan Esentürk and Prof. Dr. Ayşen Yılmaz, studying the luminescence properties of lanthanum orthoborates. After obtaining his master's degree in 2012, he joined the research group of Prof. Dr. Marc Koper as a PhD student as part of a TOP grant awarded to Prof. Dr. Marc Koper and Dr. Ludo Juurlink. In his PhD project, he studied the surface structure dependence of water related adsorbates on highly corrugated platinum surfaces. Cansın elucidated the kinetics of interfacial water on platinum in monolayer and thin-film regime. He also shed light on the influence of local surface structure to various chemical reactions on Pt surfaces. The results of his PhD research are presented in this thesis.